



저작자표시-비영리-변경금지 2.0 대한민국

이용자는 아래의 조건을 따르는 경우에 한하여 자유롭게

- 이 저작물을 복제, 배포, 전송, 전시, 공연 및 방송할 수 있습니다.

다음과 같은 조건을 따라야 합니다:



저작자표시. 귀하는 원저작자를 표시하여야 합니다.



비영리. 귀하는 이 저작물을 영리 목적으로 이용할 수 없습니다.



변경금지. 귀하는 이 저작물을 개작, 변형 또는 가공할 수 없습니다.

- 귀하는, 이 저작물의 재이용이나 배포의 경우, 이 저작물에 적용된 이용허락조건을 명확하게 나타내어야 합니다.
- 저작권자로부터 별도의 허가를 받으면 이러한 조건들은 적용되지 않습니다.

저작권법에 따른 이용자의 권리는 위의 내용에 의하여 영향을 받지 않습니다.

이것은 [이용허락규약\(Legal Code\)](#)을 이해하기 쉽게 요약한 것입니다.

[Disclaimer](#)

**Ph. D. DISSERTATION**

***Ab Initio* Study on the Symmetry- and Interface  
Structure-Driven Electronic Properties of MoS<sub>2</sub>  
for Device Application**

**by**

**Jaehong Park**

**August 2019**

**DEPARTMENT OF MATERIALS SCIENCE AND ENGINEERING  
COLLEGE OF ENGINEERING  
SEOUL NATIONAL UNIVERSITY**

*Ab Initio* Study on the Symmetry- and Interface Structure-Driven  
Electronic Properties of MoS<sub>2</sub> for Device Application

Advisor : Prof. Cheol Seong Hwang

By  
Jaehong Park

A thesis submitted to the Graduate Faculty of Seoul National University  
in partial fulfillment of the requirements for the  
Degree of Doctor of Philosophy  
Department of Materials Science and Engineering

August 2019

Approved

By

Chairman of Advisory Committee : Prof. Seungwu Han

Vice-chairman of Advisory Committee : Prof. Cheol Seong Hwang

Advisory Committee : Prof. Jin Young Kim

Advisory Committee : Prof. Yo-Sep Min

Advisory Committee : Dr. Jung-Hae Choi



# ABSTRACT

---

Molybdenum disulfide ( $\text{MoS}_2$ ) is two-dimensional (2D) crystalline material showing layered structure where three-atoms-thick crystalline sheets are stacked by van der Waals force. The 2D geometry of the structure, a defining feature of this material, has fascinated societies of academia and industry by invoking both ground-breaking solutions for device scaling and blueprints for an entirely new type of device. The 2D geometry, however, poses significant challenges in the materializations of the concepts at the same time. A particularly important issue is the interface which significantly affects the electronic properties. The interface can be either extrinsic in the device structures such as metal-oxide-semiconductor or intrinsic in the multilayer structure. In addition, crystalline symmetry of the multilayer structure varies with the way of stacking. The symmetry plays a fundamental role in determining various symmetry-related properties such as topological current and ferroelectricity.

In this dissertation, the role of interface and symmetry on the electronic properties of  $\text{MoS}_2$  is investigated using first principles calculations based on density functional theory (DFT). The theoretical study explores the structure-property correlations for the  $\text{MoS}_2$  based logic device with enhanced and new functionalities.

We begin with the study on the atomistic structure at the interface between single layer MoS<sub>2</sub> and gate oxides in field-effect transistor. This shows that the electronic band structure of MoS<sub>2</sub> can be significantly perturbed by the chemical interaction at the interface with the oxide. The results reveal the atomistic origin of mobility degradation mechanism depending on the types of oxide and calls for the importance of careful interface treatment to improve the performance of MoS<sub>2</sub> transistor.

Next, we investigate the emerging electronic properties of multilayer MoS<sub>2</sub> showing particular symmetry. Recent theoretical and experimental studies established the basis of valleytronics which harnesses the valley degrees of freedom of electrons in the multi-valley band structures as an information carrier. On the other hand, the layer degree of freedom naturally arises in the multilayer structures and can be possibly integrated into the valleytronics as an additional information carrier. The concept of the layer degree of freedom, however, was immature compared to the valley counterpart. Here, we combine the DFT and group theory calculations to thoroughly investigate the role of the symmetry of layered structure on the properties of layer degree of freedom. We show that the certain stacking structure, called 3R structure, with polar symmetry enables efficient processing of the layer degree of freedom in analogy with the valley degree of freedom in the inversion asymmetric systems.

Finally, we explore the ferroelectric functionality with the 3R structure. The

possibility of ferroelectricity of MoS<sub>2</sub> had been overlooked due to the mirror symmetry of isolated monolayer. We show that the spontaneous electric polarization can manifest itself from the interlayer interaction in the polar 3R structure. Hence the polarization is switched by the interlayer sliding. We investigate the ferroelectric switching mechanism based on the nonlinear phononics of the interlayer shear phonon with the infrared active phonon. The results indicate that the possibility of ultrafast ferroelectric switching using an intense light pulse.

This dissertation demonstrates substantial effects of the interface and the symmetry on the electronic properties of MoS<sub>2</sub> in various perspectives of applications. The constructed structure-property correlations and the strategies to utilize the emerging properties shall provide the insights to realize and advance the 2D materials device.

Keywords: Two-dimensional material, molybdenum disulfide, density functional theory, interface, crystalline symmetry, valleytronics, 2D ferroelectrics, structure-property correlation

Student number: 2013-20602

# CONTENTS

---

ABSTRACT .....	i
CONTENTS .....	iv
LIST OF FIGURES .....	vii
LIST OF TABLES .....	xv
CHAPTER 1 INTRODUCTION .....	1
1.1 Two-dimensional transition metal dichalcogenide .....	1
1.2 Electronics upon two-dimensions.....	2
1.2.1 2D channel in MOSFET .....	3
1.2.2 Valleytronics device .....	4
1.2.3 2D ferroelectrics .....	6
1.3 Role of interface and symmetry.....	7
1.4 Thesis outline.....	8
1.5 References .....	10
CHAPTER 2 THEORETICAL BACKGROUND.....	15
2.1 First principles calculation .....	15
2.1.1 Hartree-Fock theory.....	16
2.1.2 Density functional theory .....	17
2.2 Group theory.....	21
2.2.1 Group.....	21

2.2.2 Representation of group.....	22
2.2.3 Applications.....	23
2.3 References .....	23
CHAPTER 3 EFFECT OF INTERFACE ON ELECTRON TRANSPORT IN SINGLE LAYER .....	25
3.1 Introduction .....	25
3.2 Simulation method.....	27
3.3 Results and Discussion.....	29
3.3.1 Short-range order of oxides .....	29
3.3.2 Effect of interface on band dispersion.....	36
3.4 Conclusion.....	40
3.5 Appendix.....	41
3.5.1 MoS <sub>2</sub> /a-Al <sub>2</sub> O <sub>3</sub> interface.....	41
3.6 References .....	43
CHAPTER 4 EFFECT OF SYMMETRY ON VALLEYTRONICS OF MULTILAYER STRUCTURE .....	46
4.1 Introduction .....	46
4.2 Method; DFT calculation.....	48
4.3 Results and Discussion.....	50
4.3.1 Spontaneous polarization of 3R MoS <sub>2</sub> .....	50
4.3.2 Localization mechanism of <i>K</i> valley states .....	55
4.3.3 Optical selection rule for interlayer dynamics.....	68

4.4 Conclusion .....	74
4.5 Appendix.....	75
4.5.1 Berry phase Calculation.....	75
4.5.2 Calculation of crystal angular momentum .....	80
4.5.3 Calculation of double group representation.....	85
4.6 References .....	97
<b>CHAPTER 5 FERROELECTRICITY OF LAYERED STRUCTURE WITH POLAR SYMMETRY .....</b>	<b>102</b>
5.1 Introduction .....	102
5.2 Methods .....	105
5.3 Results and Discussion.....	106
5.3.1 Electric polarization and switching in bilayer 3R MoS <sub>2</sub> ...	106
5.3.2 Dynamics of coupled normal-modes under light pulse .....	115
5.4 Conclusion.....	126
5.5 References .....	126
<b>CHAPTER 6 CONCLUSION .....</b>	<b>131</b>
<b>LIST OF PUBLICATIONS .....</b>	<b>135</b>
국문 초록 .....	140

## LIST OF FIGURES

---

Figure 3.1 Atomic structures of bulk amorphous oxide and interface structure with MoS<sub>2</sub>. Short-range order of (a) *a*-SiO<sub>2</sub> showing the distinct SiO<sub>4</sub> tetrahedral network and (b) *a*-HfO<sub>2</sub> showing various coordination numbers and polyhedral connectivities. Interface structures of (c) MoS<sub>2</sub>/*a*-SiO<sub>2</sub> and MoS<sub>2</sub>/*a*-HfO<sub>2</sub> obtained by annealing at 1000 K for 50 ps. The Si-S bonds and dangling O atoms are indicated by arrows in (c).  
.....31

Figure 3.2 Evolution of interface atomic structure and interface energy for MoS<sub>2</sub>/*a*-SiO<sub>2</sub> and (b) MoS<sub>2</sub>/*a*-HfO<sub>2</sub> along the annealing time at different annealing temperatures.  $N_{\text{Si}}$ ,  $N_{\text{Hf}}$ , and  $N_{\text{S}}$  are the coordination numbers of Si, Hf, and S atoms, respectively. The dashed lines are the corresponding values for bulk *a*-SiO<sub>2</sub>, bulk *a*-HfO<sub>2</sub>, and free-standing MoS<sub>2</sub>. The shaded region in (b) indicates the standard deviation of  $N_{\text{Hf}}$  in Bulk *a*-HfO<sub>2</sub>. ...35

Figure 3.3 Comparison of the electronic properties of the interface structures with free-standing MoS<sub>2</sub>. The interface structures correspond to the structures shown in Figure 3.1(c) and (d). (a) High-symmetry points in the folded Brillouin zone (orange) of MoS<sub>2</sub> in 4×4 supercell. Band structure and wavefunction of the conduction band minimum for (b, c) free-standing MoS<sub>2</sub>, (d, e) MoS<sub>2</sub>/*a*-SiO<sub>2</sub> and (f, g) MoS<sub>2</sub>/*a*-HfO<sub>2</sub>

structures. The Si-S bonds in  $\text{MoS}_2/a\text{-SiO}_2$  are denoted by the arrow in (e).....38

Figure 3.4 (a) Short-range order of bulk  $a\text{-Al}_2\text{O}_3$  structure. (b) Snapshot of  $\text{MoS}_2/a\text{-Al}_2\text{O}_3$  interface structure annealed at 1000 K for 50 ps. (c) Electronic band structure of the interface structure. Zero-energy corresponds to the Fermi level (d) Plot of wavefunction corresponding to the CBM. ....42

Figure 4.1 Layer-index of polar 3R  $\text{MoS}_2$ . (a) The layer-index  $n$  is defined over layers stacked with the interlayer spacing  $d$  along the polar axis [001]. The direction of the spontaneous electric polarization  $P_s$  is downward ([001]) in  $\text{BCA}\cdots$  stacking. All the layers are crystallographically equivalent by the rhombohedral translational symmetry  $R$  in the periodic bulk structure. (b) The Wannier-Stark states confined in each layer under the uniform built-in potential  $V_{\text{built-in}}$  with the energy splitting corresponding to the interlayer potential  $\phi$ . (c) The magnitude of  $P_s$  and  $V_{\text{built-in}}$  calculated by DFT as a function of the number of layers. The  $P_s$  asymptotically reaches the bulk value (dashed line) with the number of layers. The potential between the top and bottom layers increases linearly by the interlayer potential  $\phi$ . ....53

Figure 4.2 Schematic band structures with the double group representation  $\Gamma$  of bilayer structure. The red and blue lines indicate spin up and down,

respectively. (a) In 3R, all the states are nondegenerate from  $C_3^\dagger$  symmetry and show WS type localization under  $E_{built-in}$  with splitting energy  $\varphi$ . Except for certain pair of opposite spins,  $\Gamma$  differ between adjacent states indicating prohibited superposition from symmetry. (b) In 2H, degeneracy arises from  $D_3^\dagger$  symmetry whose IR labels are marked with the prime ( $\Gamma'$ ). See Table 4.3 for the detailed wavefunction forms.  
 .....60

Figure 4.3 Compatibility relation for the  $K$  valley states under the electric field along the  $z$ -axis. The red and blue lines indicate spin up and down, respectively. (a) 3R structure undergoes the anti-crossing accompanied by the delocalization and spin-depolarization at the critical field. The critical field is always opposite to the built-in electric field ( $-z$  direction in the **BC** stacking). (b) In 2H structure, the anti-crossing between split VB states with the up (down) spin appears at the critical field along  $- (+)z$  direction entailing the delocalization but no spin-depolarization. .63

Figure 4.4 LDA band structures of pristine (a) and biased (b, c) 3R MoS<sub>2</sub>. (a) All the band are spin polarized and confined, including the states spanning the same IR. (b) Under the field strength of  $10 \text{ MVcm}^{-1}$ , the anti-crossing induces mixing of two CB states having identical representation  $\Gamma_6$ , which results in the significant delocalization and depolarization of spin. (c) The anti-crossing between VB states of  $\Gamma_4$

takes place at higher field of  $30 \text{ MVcm}^{-1}$ . The direction of external field is downward. ....66

Figure 4.5 LDA band structures of pristine (a) and biased (b, c)  $2\text{H MoS}_2$  ( $\mathbf{BC}$  stacking). The IR labels of  $D_3^\dagger$  are marked with the prime ( $\Gamma'$ ) in (a), on the contrary, those of  $C_3^\dagger$  are marked without the prime ( $\Gamma$ ) in (b, c) by breaking the  $D_3^\dagger$  symmetry. (a) In the absence of field, all the bands are spin-depolarized although pair of degenerate states have definite spin. The VB states are slightly delocalized. (b, c) Under the field along with the  $-z$  direction, delocalization of up spin bands becomes significant by the anti-crossing between spin up states ( $\Gamma_4$ ). By increasing the field strength from (b)  $10 \text{ MVcm}^{-1}$  to (c)  $15 \text{ MVcm}^{-1}$ , the probability distribution over two layers becomes almost symmetric. ....67

Figure 4.6 (a) Frequency and polarization of the optical selection rule at  $K$  valley of bilayer 3R structure. In the 3R homostructure, the  $\Phi^+$  transition of electrons and holes can be induced simultaneously by a single light source. At  $-K$  valley, the light polarization is reversed. (b) The  $\Delta n = -1$  operation by the illumination of photon of energy  $\hbar\omega_1 = E_g^K - \varphi$  (orange) coupled with the  $\Sigma^-$  transition. Simultaneous incidence with the  $\hbar\omega_2 = \varphi$  (red) triggers the  $\Phi^+$  transition by virtue of the excited-state absorption, corresponding to the  $\Delta n = +1$  operation. The magnitude of  $P_s$

is modulated in accord with the configuration of electron-hole carriers. The valley-index can be independently controlled by the helicity for each frequency and constitutes the  $2 \otimes 2$  quantum states in total with the layer-index. ....71

Figure 4.7 Optical selection rule of various commensurate heterostructures.

Bilayer heterostructures  $\text{MX}_2/\text{M}'\text{X}'_2$  and the schematics of the  $K$  valleys drawn in the real space along the  $[001]$  axis. Optical transitions are classified into  $\Sigma$  (across the band gap in the visible range) and  $\Phi$  (interlayer charge transfer in the infrared range) types with the superscript corresponding to the change of layer-index  $\Delta n$ . Frequency selection rule can be varied with the details of the energy spectra such as band offsets and Zeeman spin splitting depending on the chemistry; e.g.,  $\text{M} = \{\text{Mo}, \text{W}\}$  and  $\text{X} = \{\text{S}, \text{Se}, \text{Te}\}$ . The polarization selection rule is independent of the chemistry. At the  $-K$  valley, the light helicity is reversed .....72

Figure 4.8 Built-in potential developed by the spontaneous polarization of the

finite layers of 3R  $\text{MoS}_2$ . Plane-averaged electrostatic potential profiles along the  $[001]$  axis of 2-5 layers of 3R  $\text{MoS}_2$  (**BCA**... stacking) calculated using vacuum-slab structures with (a) LDA, (b) PBE-D2 and (c) PBE-D3 functionals.  $\Delta V$  is the potential difference between the top and bottom layers. ....78

Figure 4.9 Finite layers of 3R stacking sandwiched in supercell structure.

Finite layers (2-5 layers) of MoS<sub>2</sub> with polar 3R stacking are intercalated between non-polar stacking (including 2H). In-plane lattice parameters, layer thickness and interlayer distances in the supercell structures are the same with those of bulk 3R MoS<sub>2</sub>. .....79

Figure 4.10 In the commensurate structure, position of the Mo and S atoms

projected onto the 2D hexagonal primitive cell corresponds to the partial translation vectors  $\mathbf{t}_A = \mathbf{a}_1$ ,  $\mathbf{t}_B = 2/3\mathbf{a}_1 + 1/3\mathbf{a}_2$  and  $\mathbf{t}_C = 1/3\mathbf{a}_1 + 2/3\mathbf{a}_2$ , respectively. The  $C_3^+$  symmetry axes at  $\mathbf{t}_A$ ,  $\mathbf{t}_B$  and  $\mathbf{t}_C$  are all preserved in any commensurate stacking. The CAM is the eigenvalue of the  $C_3^+$  symmetry axis at  $\mathbf{t}_A$ . .....81

Figure 5.1 (a) Stacking-dependent spontaneous polarization of bilayer 3R

MoS<sub>2</sub>. (b) Energy of the bilayer structure depending on the stacking sequence.  $\Phi_{\text{NEB}}$  is the ferroelectric switching barrier calculated by the NEB method. (c) Displacement patterns of the interlayer shear mode ( $Q_{LS}$ ) and the infrared mode ( $Q_{IR}$ ) mode along the in-plane polarization direction  $r$ . (d) Phonon dispersion of the bilayer 3R MoS<sub>2</sub>. The zone-center  $Q_{LS}$  mode at 0.6 THz and  $Q_{IR}$  mode at 11.4 THz are denoted by arrows. ....107

Figure 5.2 (a) Top view of the AB stacked 3R MoS<sub>2</sub> showing the  $C_{3v}$  symmetry.

In the AB stacking, the S atoms in the upper layer are on the top of the

Mo atoms in the lower layer (bottom layer is depicted as dimmed). The x- and y- axis corresponds to the zigzag and armchair axis of MoS<sub>2</sub>, respectively. The AB stacking changes to the AC stacking under the deformation induced by the positive amplitude of  $Q_{LS}$  along the three equivalent directions  $r_1$ ,  $r_2$  and  $r_3$ . (b) Potential energy surface  $V(Q_{IR}, Q_{LSx}, Q_{LSy})$  on the  $(Q_{LSx}, Q_{LSy})$  coordinates for  $Q_{IR} = 0 \text{ \AA}\mu$  ( $\mu$  is atomic mass unit). The AB stacking corresponds to the origin  $(0, 0)$ . (c, d) Polarization-dependent modulation of the potential energy landscape at (c)  $Q_{IRx} = \pm 5 \text{ \AA}\mu$  and at (d)  $Q_{IRy} = \pm 5 \text{ \AA}\mu$  via anharmonic coupling..110

Figure 5.3 Evolution of potential energy curve on the  $Q_{LS}$  coordinate along the ferroelectric switching directions under (a, b) x-polarized and (c, d) y-polarized pulse. Rapidly oscillating  $Q_{IRx}$  under pulse modulates the potential energy curve (grey lines) with respect to the static case at  $Q_{IR} = 0 \text{ \AA}\mu$  (black line). The effective potential energy experienced by the  $Q_{LS}$  is the time-average of the potential energy curves (orange line).  $\langle\Phi\rangle$  is the effective energy barrier under the pulse while  $\Phi_0$  is pristine energy barrier. Direction and relative magnitude of the effective anharmonic force  $F_{anh}$  on  $Q_{LS}$  are depicted by the orange arrow. (e) Effective interlayer interaction between the Mo and S sublattices induced by  $Q_{IR}$ . (f) Contour plot of the interaction energy indicates the direction and relative magnitude of the anharmonic force depending on the polarization direction of  $Q_{IR}$  (see main text for the details).....118

Figure 5.4 Dynamics of the normal-modes under the x-polarized pulse (a, b) without and (c) with damping. (a) Amplification of the  $Q_{LSy}$  mode through the anharmonic force by the pulse at 0 K. (b) At 300 K, the  $Q_{LSy}$  has sufficient kinetic energy to overcome the effective energy barrier ( $\langle\Phi\rangle = 11.5$  meV at  $|Q_{IRx}| = 5.35 \text{ \AA}\mu$ ) after the pumping, and oscillates back and forth between the AB ( $Q_{LSy} = 0 \text{ \AA}\mu$ ) and AC ( $Q_{LSy} = 16.29 \text{ \AA}\mu$ ) stackings without dissipation. (c) In the presence of damping, the  $Q_{LSy}$  mode at 0 K overcomes the energy barrier after eight sequential pulses. The AB stacking changes to the AC stacking and does not return due to the dissipation of kinetic energy. (d) Schematics of ferroelectric switching through the  $Q_{IRx}$ - $Q_{LSy}$  coupling. The orange arrows indicates the directions of interlayer shear induced by the x-polarized pulse, which are opposite in the AB and AC stackings. ....122

Figure 5.5 Dynamics of the normal-modes under the y-polarized pulse (a, b) without and (c) with damping. (a) Amplification of the  $Q_{LSy}$  mode through the anharmonic force by the pulse at 0 K. (b) the  $Q_{LSy}$  cannot overcome the increased effective energy barrier although its kinetic energy is increased by the pulse. (c) The gaining of kinetic energy of  $Q_{LSy}$  is smaller than x-polarized case. Even eight pulses are irradiated, switching does not take place .....125

## LIST OF TABLES

---

Table 4.1 Calculated structural and electronic properties of the bulk 3R and 2H MoS <sub>2</sub> in comparison with experimental data.....	54
Table 4.2 Stacking-dependent crystal angular momentum (CAM) of the Bloch wavefunctions $ n,l\rangle$ at the $K$ valley.....	57
Table 4.3 Symmetry-adapted form of the $K$ valley states and corresponding irreducible representation (IR) of the double group for the bilayer 3R and 2H structure. ....	59
Table 4.4 Character table of double group $C_3^\dagger$ [44].....	89
Table 4.5 Character table of double group $D_3^\dagger$ [44].....	92
Table 5.1 The anharmonic coefficient $c_{lmn}$ for $Q_{IR}^l Q_{LSx}^m Q_{LSy}^n$ coupling terms for each $Q_{IRx}$ and $Q_{IRy}$ mode. The values are shown up to 5th power coupling terms in unit of $\text{meV}\text{\AA}^{-(l+m+n)}\mu^{-(l+m+n)/2}$ . ....	114

# CHAPTER 1

## INTRODUCTION

---

### 1.1 Two-dimensional transition metal dichalcogenide

Two-dimensional (2D) material refers to the atomically thin sheet of crystal or its stacked form. The study on 2D materials began in earnest with the isolation of the single layer graphene from graphite using adhesive tape in 2004[1] and subsequent observation of celebrated massless Dirac fermion and quantum Hall effects[2,3]. Importantly, this astonishing event triggered a search for the other 2D materials candidates by renewing the interests in all the known layered materials bonded by van der Waals (vdW) interaction[4]. The transition metal dichalcogenides (TMDCs) of the chemical formula  $MX_2$  are crystallized in three-atom-thick crystalline sheets with various combinations of metal and chalcogen elements from the periodic table[5]. The TMDCs constitute the one of the most important class of 2D materials which exhibits various structural and electronic phases ranging from the

semiconducting[6,7], (semi-) metallic[8], and superconducting[9] phases to those with topological characteristics[10–12].

Molybdenum disulfide ( $\text{MoS}_2$ ) is representative TMDC naturally found as an earth-abundant mineral. The early interest in  $\text{MoS}_2$  was mainly on the tribological applications due to the easy interlayer sliding[13]. Being enlightened from the graphene case, many researchers started to focus on more fascinating aspects of the  $\text{MoS}_2$  in electronics applications. The  $\text{MoS}_2$  is stable in semiconducting phase in ambient conditions, which is suitable for ultrathin transistor applications[14] compared to the invariably semi-metallic graphene[15]. Also, the band structure exhibits multiple extrema at momentum space enabling the valleytronics applications[16]. Moreover, the  $\text{MoS}_2$  has the rich structure-property correlations such as stacking-dependent band structure modulations[6,7,17], and metal-semiconductor transitions through the reconstruction within individual layers[18]. All these facets have attracted vast attention across the fields of science and engineering for the realization of the electronics upon two-dimensions using the  $\text{MoS}_2$  as a prototypical materials platform.

## 1.2 Electronics upon two-dimensions

Understanding of the physics and chemistry of  $\text{MoS}_2$  is now becoming more sophisticated. Nonetheless, it is yet a long way to go to realize next-generation

devices harnessing its unique advantages. In followings, brief reviews are given for the researches on the device applications categorized by the three mainstream directions; field-effect transistor, valleytronics device, and ferroelectrics.

### 1.2.1 2D channel in MOSFET

The scaling of silicon-based metal-oxide-semiconductor field-effect transistor (MOSFET) is expected to end up the stage where the switching speed and switching energy cannot be further improved simultaneously [19]. Upon pursuing the scaling, the geometry of MOSFET has been evolved in order to improve the electrostatic controllability over the channel from the single-gate to the multi-gate one[20]. So-called FinFET, where the fin-shaped channel silicon is wrapped by the gate oxide at the three facets, came into the successful commercialization[21]. Replacing the silicon with other materials will be another revolutionary breakthrough in realizing the next-generation device. The III-V compounds exhibiting extremely higher carrier mobility seems to be a straightforward solution, however, calls for many technological challenges[22].

The MoS<sub>2</sub> has attracted many research interests as a potential candidate for true 2D channel material[23]. The MoS<sub>2</sub> based MOSFET can be considered as an ultimate form of the gate-all-around MOSFET based on the silicon

channel which is shaped into the nanosheet[24]. Single layer MoS<sub>2</sub> has the sizable band gap (~1.8 eV)[6,8] and good theoretical mobility (~200-400 cm<sup>2</sup>V<sup>-1</sup>s<sup>-1</sup>)[25,26] which are promising for high-performance and low-power device. Especially, this will greatly enhance the electrostatic gate control since all the electrons are confined in the true 2D geometry at the immediate proximity of the electric field from the gate oxide. The MoS<sub>2</sub> based MOSFET features high on/off ratio (~10<sup>8</sup>) and low subthreshold swing (below 80 mV/decade)[14]. However, the mobility of MoS<sub>2</sub> in the MOSFET structure severely degraded from the theoretical value predicted from the free-standing form[27]. The most effective strategy was utilizing the high-*k* gate oxides such as HfO<sub>2</sub> and Al<sub>2</sub>O<sub>3</sub> in order to suppress the Coulombic scatterings from the defects near the channel region[28]. However, the mobility enhancement mechanism has been arguable because the surface optical phonons of high-*k* oxides might scatter the carriers stronger than the low-*k* oxide such as SiO<sub>2</sub>[29]. On the other hand, the encapsulation of MoS<sub>2</sub> with other 2D materials like graphene or boron nitride to avoid the defects showed mild improvements[30].

### 1.2.2 Valleytronics device

Another important research field of the MoS<sub>2</sub> is to build entirely new types of logic devices utilizing the unique electronic structure. In conventional electronics, digital information (0 and 1 states) is encoded based on the

presence or absence of the electronic charge in the real space. By contrast, the valleytronics is an emerging information technology in which the information is encoded in valley degrees of freedom (DOF) of electrons in momentum (reciprocal) space[16]. The MoS<sub>2</sub> has the multi-valley band structure where the band extrema appear at two inequivalent points  $\pm K$  in the momentum space[31]. The electrons with opposite momentum can be distinguished because they are conjugated with the opposite Berry curvature and magnetic moment under the time-reversal symmetry[16]. The read/write operations rely on the conjugate properties by which electrons differently response to the external electric or optical field at two valleys[31]. This protocol is hence feasible only in the system without inversion symmetry which would make two valleys indistinguishable[16].

Valleytronics is yet in the conceptual stage compared to the spintronics which has a commercialized device architecture like the STT-MRAM (spin torque transfer magnetic random access memory)[32]. Valleytronics is expected to have advantages similar to spintronics such as nonvolatility and low power consumption[33]. The single layer MoS<sub>2</sub> with broken inversion symmetry had been the main platform of the fundamental study at the early stage[34,35]. Soon the research interest transferred to the multilayer form where the various stacking-dependent phenomena were explored[17,36,37]. In particular, it was noted that electrons in layered structure gain another DOF related to the position among layers, so-called as layer-index or layer pseudospin[38]. The

layer-index is the most natural DOF arising at the layered 2D materials. If this can be harnessed as an additional information carrier along with the valley DOF, for example, the information density can be simply multiplied. However, the possibility of integration of layer-index concept into the valleytronics has not been investigated.

### 1.2.3 2D ferroelectrics

Ferroelectric materials should have stable ground states of distinct electric polarizations which are switchable by an electric field. Ferroelectricity is an important material property to realize the non-volatile memory devices. The bulk ferroelectric materials such as perovskite[39] and zirconia-hafnia[40] systems have been mainly studied for the ferroelectric memory devices to date. Upon pursuing the scaling of the devices for the higher storage density and low power consumption, the ferroelectric films have been thinned into the few tens of nanometer scale[41]. In the angstrom scale, however, whether the bulk ferroelectrics retain the ferroelectricity against the depolarization field is still an open question[42–44]. On the other hand, observation on the robust ferroelectricity from the atomically thin crystals based on polyvinylidene fluoride indicates the possibility of robust ferroelectricity without the size effect based on the low-dimensional materials[45].

The study on the ferroelectrics based on 2D materials is very limited despite

its importance in both technological and theoretical perspectives. To date, 2D ferroelectricity has been reported for some of the group IV-VII[46] and group III-V[47] compounds, but not for the TMDC in the experiments. The ferroelectric TMDC will enable the non-volatile device with combinations of the extreme scale and the unique functionalities of the TMDC.

### 1.3 Role of interface and symmetry

The interface between dissimilar materials is omnipresent in any functional unit of the electronic devices and is a crucial factor affecting the properties. Compared to the bulk materials, the extrinsic interface effect will be more dominating in the 2D materials; it is even difficult to distinguish the ultrathin body and the interface (surface). For instance, the carriers confined in the proximity of interface with gate oxides becomes more vulnerable to the scattering at the interface[29], which corresponds to another side of the coin; the enhancement of gate controllability over the confined carriers[23]. It is apparent that the 2D channel will show intrinsic performance when its atomic and electronic structures are intact like in the free-standing form[48]. In addition, the intrinsic interface will form between layers in any multilayer structures, which can modulate the properties substantially also[6,7,17].

The symmetry of materials determines many of the properties at firsthand. The understanding of the symmetry-dependent properties is essential to

design the materials for the target function. For instance, the ferroelectricity only appears in the materials with polar symmetry structure[49]. And, the inversion asymmetric material is used for valleytronics device in order to process the valley information[16]. Importantly, the 2D materials can have various crystalline symmetries depending on how to stack the individual layers[50]. Thus, careful inspection is necessary to predict the properties emerging from the underlying symmetry.

## 1.4 Thesis outline

At the heart of this dissertation is to look at carefully the electronic properties driven by interface and symmetry in order to improve and extend the functionality of MoS<sub>2</sub> for device applications. First principle calculation is a powerful theoretical tool to investigate such structure-property correlations in atomic scale. In this dissertation, we address the important issues in the field of MoS<sub>2</sub> based electronic devices using the first principles.

Chapter 3 presents a study on the atomistic mechanism of mobility degradation from the interface between the single layer MoS<sub>2</sub> and gate oxides. We compare the high-*k* HfO<sub>2</sub> and low-*k* SiO<sub>2</sub> which have shown, consistently in previous experiments, the mobility enhancement and degradation, respectively. We show that the SiO<sub>2</sub> forms the interfacial bonds or defects at the interface and significantly reduces the electron effective mass of MoS<sub>2</sub>. In

contrast, the electronic structure of MoS<sub>2</sub> is preserved, like free-standing form, in contact with the HfO<sub>2</sub> which does not form interfacial defects. The origin of the distinct interface chemistry is discussed. The results provide an atomic-scale understanding of mobility engineering using gate oxides.

In Chapter 4, we investigate the role of stacking-dependent symmetry on the electronic valley structures in order to construct a concept of the controllable layer degrees of freedom of electrons in the multilayer structures. By combining the group theory with the first principles calculations, we elucidate certain conditions to have the valley carriers suitable for interlayer motion control. Namely, the 3R structure MoS<sub>2</sub> with polar symmetry retaining the internal electric field hosts the carriers confined in the individual layer whose interlayer motions can be selectively induced based on the energy conservations upon interaction with the photons. We thoroughly discuss the effect of the spin-orbit coupling under double group symmetries on the valleytronics with various stacking structures.

Chapter 5 investigates the ferroelectric switching mechanism of the bilayer 3R structure MoS<sub>2</sub>. We focus on the optically driven switching based on the nonlinear phonics by which the selective excitations of infrared active mode leads amplification of Raman active interlayer shear mode from anharmonic couplings. First principles calculations and lattice dynamics simulations show that the intense optical pulses polarized along the certain crystallographic axis of MoS<sub>2</sub> can lead the large amplitude of interlayer translation to reverse the

electric polarization.

## 1.5 References

- [1] Novoselov K S 2004 *Science*. 306 666–9
- [2] Novoselov K S, Geim A K, Morozov S V., Jiang D, Katsnelson M I, Grigorieva I V., Dubonos S V. and Firsov A A 2005 *Nature* 438 197–200
- [3] Zhang Y, Tan Y-W, Stormer H L and Kim P 2005 *Nature* 438 201–4
- [4] Xu M, Liang T, Shi M and Chen H 2013 *Chem. Rev.* 113 3766–98
- [5] Manzeli S, Ovchinnikov D, Pasquier D, Yazyev O V. and Kis A 2017 *Nat. Rev. Mater.* 2 17033
- [6] Splendiani A, Sun L, Zhang Y, Li T, Kim J, Chim C-Y, Galli G and Wang F 2010 *Nano Lett.* 10 1271–5
- [7] Mak K F, Lee C, Hone J, Shan J and Heinz T F 2010 *Phys. Rev. Lett.* 105 136805
- [8] Eda G, Yamaguchi H, Voiry D, Fujita T, Chen M and Chhowalla M 2011 *Nano Lett.* 11 5111–6
- [9] Zhang Y J, Iwasa Y, Arita R, Ye J T, Bahramy M S and Akashi R 2012 *Science*. 338 1193–6
- [10] Qian X, Liu J, Fu L and Li J 2014 *Science*. 346 1344–7
- [11] Soluyanov A A, Gresch D, Wang Z, Wu Q, Troyer M, Dai X and Bernevig B A 2015 *Nature* 527 495–8

- [12] Hsu Y-T, Vaezi A, Fischer M H and Kim E-A 2017 *Nat. Commun.* 8 14985
- [13] Martin J M, Donnet C, Le Mogne T and Epicier T 1993 *Phys. Rev. B* 48 10583–6
- [14] Radisavljevic B, Radenovic A, Brivio J, Giacometti V and Kis A 2011 *Nat. Nanotechnol.* 6 147–50
- [15] Craciun M F, Russo S, Yamamoto M, Oostinga J B, Morpurgo A F and Tarucha S 2009 *Nat. Nanotechnol.* 4 383–8
- [16] Xiao D, Yao W and Niu Q 2007 *Phys. Rev. Lett.* 99 236809
- [17] Suzuki R, Sakano M, Zhang Y J, Akashi R, Morikawa D, Harasawa A, Yaji K, Kuroda K, Miyamoto K, Okuda T, Ishizaka K, Arita R and Iwasa Y 2014 *Nat. Nanotechnol.* 9 611–7
- [18] Kappera R, Voiry D, Yalcin S E, Branch B, Gupta G, Mohite A D and Chhowalla M 2014 *Nat. Mater.* 13 1128–34
- [19] Waldrop M M 2016 *Nature* 530 144–7
- [20] Ferain I, Colinge C A and Colinge J-P 2011 *Nature* 479 310–6
- [21] Auth C, Aliyarukunju A, Asoro M, Bergstrom D, Bhagwat V, Birdsall J, Bisnik N, Buehler M, Chikarmane V, Ding G, Fu Q, Gomez H, Han W, Hanken D, Haran M, Hattendorf M, Heussner R, Hiramatsu H, Ho B, Jaloviar S, Jin I, Joshi S, Kirby S, Kosaraju S, Kothari H, Leatherman G, Lee K, Leib J, Madhavan A, Marla K, Meyer H, Mule T, Parker C, Parthasarathy S, Pelto C, Pipes L, Post I, Prince M, Rahman A, Rajamani S, Saha A, Santos J D, Sharma M, Sharma V, Shin J, Sinha P, Smith P, Sprinkle M, Amour A St.,

- Staus C, Suri R, Towner D, Tripathi A, Tura A, Ward C and Yeoh A 2017 *2017 IEEE International Electron Devices Meeting (IEDM)* (IEEE) pp 29.1.1-29.1.4
- [22] del Alamo J A 2011 *Nature* 479 317–23
- [23] Fiori G, Bonaccorso F, Iannaccone G, Palacios T, Neumaier D, Seabaugh A, Banerjee S K and Colombo L 2014 *Nat. Nanotechnol.* 9 768–79
- [24] Bae G, Bae D-I, Kang M, Hwang S M, Kim S S, Seo B, Kwon T Y, Lee T J, Moon C, Choi Y M, Oikawa K, Masuoka S, Chun K Y, Park S H, Shin H J, Kim J C, Bhuwalka K K, Kim D H, Kim W J, Yoo J, Jeon H Y, Yang M S, Chung S-J, Kim D-W, Ham B H, Park K J, Kim W D, Park S H, Song G, Kim Y H, Kang M S, Hwang K H, Park C-H, Lee J-H, Kim D-W, Jung S-M and Kang H K 2018 *2018 IEEE International Electron Devices Meeting (IEDM)* vol 2018-Decem (IEEE) pp 28.7.1-28.7.4
- [25] Kaasbjerg K, Thygesen K S and Jacobsen K W 2012 *Phys. Rev. B* 85 115317
- [26] Li X, Mullen J T, Jin Z, Borysenko K M, Buongiorno Nardelli M and Kim K W 2013 *Phys. Rev. B* 87 115418
- [27] Li S-L, Tsukagoshi K, Orgiu E and Samorì P 2016 *Chem. Soc. Rev.* 45 118–51
- [28] Yu Z, Ong Z-Y, Pan Y, Cui Y, Xin R, Shi Y, Wang B, Wu Y, Chen T, Zhang Y-W, Zhang G and Wang X 2016 *Adv. Mater.* 28 547–52
- [29] Ma N and Jena D 2014 *Phys. Rev. X* 4 011043
- [30] Cui X, Lee G-H, Kim Y D, Arefe G, Huang P Y, Lee C-H, Chenet D A,

- Zhang X, Wang L, Ye F, Pizzocchero F, Jessen B S, Watanabe K, Taniguchi T, Muller D A, Low T, Kim P and Hone J 2015 *Nat. Nanotechnol.* 10 534–40
- [31] Xiao D, Liu G-B, Feng W, Xu X and Yao W 2012 *Phys. Rev. Lett.* 108 196802
- [32] Song Y J, Lee J H, Shin H C, Lee K H, Suh K, Kang J R, Pyo S S, Jung H T, Hwang S H, Koh G H, Oh S C, Park S O, Kim J K, Park J C, Kim J, Hwang K H, Jeong G T, Lee K P and Jung E S 2016 *2016 IEEE International Electron Devices Meeting (IEDM)* (IEEE) pp 27.2.1-27.2.4
- [33] Mak K F, Xiao D and Shan J 2018 *Nat. Photonics* 12 451–60
- [34] Mak K F, He K, Shan J and Heinz T F 2012 *Nat. Nanotechnol.* 7 494–8
- [35] Zeng H, Dai J, Yao W, Xiao D and Cui X 2012 *Nat. Nanotechnol.* 7 490–3
- [36] Zhu B, Zeng H, Dai J, Gong Z and Cui X 2014 *Proc. Natl. Acad. Sci.* 111 11606–11
- [37] Jones A M, Yu H, Ross J S, Klement P, Ghimire N J, Yan J, Mandrus D G, Yao W and Xu X 2014 *Nat. Phys.* 10 130–4
- [38] Xu X, Yao W, Xiao D and Heinz T F 2014 *Nat. Phys.* 10 343–50
- [39] Scott J F 2007 *Science.* 315 954–9
- [40] Park M H, Lee Y H, Mikolajick T, Schroeder U and Hwang C S 2018 *MRS Commun.* 8 795–808
- [41] Ihlefeld J F, Harris D T, Keech R, Jones J L, Maria J-P and Trolrier-McKinstry S 2016 *J. Am. Ceram. Soc.* 99 2537–57
- [42] Junquera J and Ghosez P 2003 *Nature* 422 506–9

- [43] Sai N, Fennie C J and Demkov A A 2009 *Phys. Rev. Lett.* 102 107601
- [44] Gao P, Zhang Z, Li M, Ishikawa R, Feng B, Liu H-J, Huang Y-L, Shibata N, Ma X, Chen S, Zhang J, Liu K, Wang E-G, Yu D, Liao L, Chu Y-H and Ikuhara Y 2017 *Nat. Commun.* 8 15549
- [45] Bune A V V, Fridkin V M M, Ducharme S, Blinov L M M, Palto S P P, Sorokin A V V, Yudin S G G and Zlatkin A 1998 *Nature* 391 874–7
- [46] Chang K, Liu J, Lin H, Wang N, Zhao K, Zhang A, Jin F, Zhong Y, Hu X, Duan W, Zhang Q, Fu L, Xue Q-K, Chen X and Ji S-H 2016 *Science*. 353 274–8
- [47] Cui C, Hu W-J, Yan X, Addiego C, Gao W, Wang Y, Wang Z, Li L, Cheng Y, Li P, Zhang X, Alshareef H N, Wu T, Zhu W, Pan X and Li L-J 2018 *Nano Lett.* 18 1253–8
- [48] Bolotin K I, Sikes K J, Jiang Z, Klima M, Fudenberg G, Hone J, Kim P and Stormer H L 2008 *Solid State Commun.* 146 351–5
- [49] Rabe K M, Ahn C H, Triscone J M-M, Dawber M and Lichtensteiger C 2007 *Physics of Ferroelectrics* vol 105 (Berlin, Heidelberg: Springer Berlin Heidelberg)
- [50] Ribeiro-Soares J, Almeida R M, Barros E B, Araujo P T, Dresselhaus M S, Cançado L G and Jorio A 2014 *Phys. Rev. B* 90 115438

## CHAPTER 2

### THEORETICAL BACKGROUND

---

#### 2.1 First principles calculation

First principles calculation is the principal method in this dissertation. The first principles approach is to study a physical phenomena by solving the fundamental equation governing the system. The quantum mechanical behavior of electrons is described by the Schrödinger equation. The electronic part of the Schrödinger equation for  $N$  electrons is given by Born–Oppenheimer approximation (in atomic unit)

$$\left\{ -\frac{\hbar}{2m} \sum_i \nabla_i^2 - \sum_{i,j} \frac{Z_j}{|r_i - R_j|} + \frac{1}{2} \sum_{i \neq i'} \frac{1}{|r_i - r_{i'}|} \right\} \Psi = (K + V + U)\Psi = E\Psi,$$

where  $\Psi(r_1, r_2, \dots, r_N)$  is electronic wavefunction, and  $R_j$  and  $Z_j$  are coordinate and charge of the nucleus, respectively. Typical materials systems

consist of a substantial number of electrons and nucleus for which the Schrödinger equation cannot be solved by itself. Nonetheless, if the solution is obtained, all the properties of materials can be obtained without any approximations. The density functional theory (DFT) has become a standard for the first principle calculations, which enabled ones to study of many kinds of physical and chemical properties of materials on the basis of quantum mechanics with affordable computational resources[1]. In followings, backgrounds of the DFT is described briefly.

### 2.1.1 Hartree-Fock theory

Hartree-Fock method[2] is an early approach to solve the Schrödinger equation. The primary approximation is to express the wavefunction by Slater determinant in the form of

$$\Psi(r_1, r_2, \dots, r_N) = \frac{1}{N!} \begin{vmatrix} \varphi_1(x_1) & \cdots & \varphi_N(x_1) \\ \vdots & \ddots & \vdots \\ \varphi_1(x_N) & \cdots & \varphi_N(x_N) \end{vmatrix},$$

where  $\varphi(x)$  is one-electron spin-orbital as a function of both coordinate and spin, which is normalized as  $\langle \varphi_i | \varphi_j \rangle = \delta_{ij}$ . The determinant is antisymmetric under electron exchange  $P_{ij} \Psi = -\Psi$ , hence trivially satisfy the Pauli principle. The approximation of  $\Psi$  by a single Slater determinant is exact

only for the non-interacting systems ( $U = 0$ ) for which the to the electron coordinates are separable.

The best approximate ground state wavefunction is obtained by optimizing trial wavefunction  $\tilde{\Psi}$  using the variational principle  $E_0 = \min_{\tilde{\Psi}} \langle \tilde{\Psi} | H | \tilde{\Psi} \rangle$ .

This results in the Hartree-Fock equation

$$h^{HF} \varphi_i(r) = \left\{ -\frac{1}{2} \nabla_i^2 + v(r) \right\} \varphi_i(r) + \sum_{j \neq i} \int dr' \left\{ \frac{|\varphi_j(r')|^2}{|r-r'|} \varphi_i(r) - \frac{\varphi_j^*(r') \varphi_i(r')}{|r-r'|} \varphi_j(r) \right\}$$

$$= \varepsilon_i \varphi_i$$

Each electron in the equation moves in the effective potential asserted by the rest of electrons, and the equation is solved self-consistently. The equation is based on the wavefunction with  $3N$  spatial coordinates, which becomes extremely difficult to solve when the system size goes large. The computational cost increases  $O^4$  (and much more for more sophistication) as the growing size of the system ( $N$  or size of the basis functions). The most time-consuming part is the calculation of orbital-dependent, nonlocal, exchange operators in the equation[3].

### 2.1.2 Density functional theory

The DFT provides an accurate and efficient way to obtain ground state properties. The DFT is fundamentally different from earlier method in that

this approach uses the electron density as a basic variable rather than the wavefunction;

$$n(r) = N \int dr_2 \dots dr_N \Psi^*(r, r_2, \dots, r_N) \Psi(r, r_2, \dots, r_N).$$

In 1964, Hohenberg and Kohn[4] supposed the one-to-one correspondence between ground state electron density  $n(r)$  and external potential  $v(r)$  for the interacting electronic system which is defined by the external potential  $v(r)$ . Therefore, the  $n(r)$  determines both  $N$  and  $v(r)$ , and hence the entire Hamiltonian. The lemma indicates that obtaining the  $n(r)$  is equivalent to solving the Schrodinger equation. Hohenberg and Kohn defined the total energy functional

$$E_v[n(r)] \equiv \int v(r)n(r)dr + F[n(r)],$$

where  $F[n(r)] \equiv \langle \Psi | T + U | \Psi \rangle$  is a universal functional independent of external potential (i.e. nucleus configurations in the crystal structure). The ground state electron density and energy are obtained via the Hohenberg-Kohn variational principle in terms of trial density  $n(r)$ ,

$$E_0 = \min_{\tilde{n}(r)} E_v[\tilde{n}(r)].$$

In this way, the problem of solving Schrödinger equation with  $3N$  dimensional wavefunction is transformed into the that of minimizing  $E[n(r)]$  with respect

to the electron density function with 3 dimensions only. One major remaining task was to find the explicit expression of the kinetic energy functional. The Kohn and Sham[5] adopted the kinetic energy functional  $T_s[n(r)]$  for the noninteracting electronic system, and expressed the energy functional as

$$E_v[n(r)] = T_s[n(r)] + \int dr dr' \frac{n(r)n(r')}{|r-r'|} + E_{xc}[n(r)].$$

The variational method on this functional with respect to  $n(r)$  results in the Kohn-Sham equation taking the form of

$$\left\{ -\frac{1}{2} \nabla_i^2 + v(r) + \int dr' \frac{n(r')}{|r-r'|} + v_{xc}(r) \right\} \phi_i(r) = \varepsilon_i \phi_i(r),$$

where  $v_{xc}(r) = \frac{\delta E_{xc}[n(r)]}{\delta n(r)}$  and  $E_{xc}[n(r)]$  is the exchange-correlation energy functional. The ground state energy is given by

$$E = \sum_i \varepsilon_i + E_{xc}[n(r)] - \int v_{xc}(r)n(r)dr - \frac{1}{2} \int dr dr' \frac{n(r)n(r')}{|r-r'|}.$$

The Kohn-Sham equation describes the noninteracting particles moving in an effective potential, and is solved self-consistently like Hartree-Fock equation. The important distinction of Kohn-Sham formulation from the Hartree-Fock is that all the many-body effect is rigorously included in the exchange-

correlation functional in Kohn-Sham equation. Provided that the  $E_{xc}[n(r)]$  ( $v_{xc}(r)$ ) is exact, Kohn-Sham equation gives an exact solution of Schrodinger equation. Therefore, the accuracy of DFT is critically dependent on the accuracy of the  $E_{xc}[n(r)]$ [6].

The simplest and powerful approximation for the  $E_{xc}[n(r)]$  is local density approximation (LDA)[7],

$$E_{xc}^{LDA}[n(r)] = \int e_{xc}(n(r))n(r)dr,$$

where  $e_{xc}(n(r))$  is the exchange-correlation energy per particle of a uniform electron gas of density  $n$ . In this form, the exchange-correlation energy is solely dependent on the value of the density at the point  $n(r)$ . Despite the crude approximation, the LDA accurately describes the bonding energies and geometry of materials for many cases. The LDA becomes inaccurate when the assumption of slowly varying density  $n(r)$  is incorrect, which is remedied to some extent in generalized gradient approximation (GGA)[8]. However, both LDA and GGA fail in describing systems showing non-local interaction such as van der Waals interaction in 2D materials for which further corrections are required[9].

## 2.2 Group theory

Group theory serves as a powerful tool to solve physical problems efficiently by utilizing the underlying symmetry of the physical system. For instance, it dictates the allowed forms of quantum states of electrons and phonons. It also informs how to induce transitions between the quantum states as intended by external driving forces. Here, a basic concept of group theory relevant to this dissertation is presented.

### 2.2.1 Group

In mathematics, an algebraic structure is a set of elements equipped with some operations defined on the set. *Group* is one of the simplest algebraic structure[10]. A group  $G$  is defined as a set  $G = \{E, A, B, C, \dots\}$  with an operation, called group multiplication, which associates an ordered pair of two elements with the third element by  $AB = C$ . To qualify as a group, it should satisfy four axioms; (1) it is closed under the group multiplications, i.e. If  $A$  and  $B \in G$ , and  $AB = C$ , then  $C \in G$ , (2) group multiplication is associative  $(AB)C = A(BC)$ , (3) it has an identity element of the group multiplications, i.e.  $AE = EA = A$ , (4) each element has its inverse, i.e.  $A^{-1}A = A^{-1}A = E$ .

### 2.2.2 Representation of group

Such an abstract mathematical object is closely related to natural phenomena because the set of symmetries of the physical system exactly show the properties of the group. A symmetry of a geometrical object in space is represented by a coordinate transformation matrix under which the object is invariant. The set of matrices satisfies the group axioms and forms a symmetry group of the object; *e.g.* point/space group of crystals. This concept is formulated in the context of representation of group.

A *representation* of group  $G$  on vector space  $V$  is a homomorphism  $\Gamma: G \rightarrow GL(V)$ , where  $GL(V)$  is a group of invertible matrices acting on  $V$  (general linear group)[11]. Since the homomorphism preserves the structure of group such that  $\Gamma(A)\Gamma(B) = \Gamma(AB)$ , calculations based on the representation become simply a matrix algebra. In many cases, the vector space  $V$  is possibly partitioned into subspaces  $W \subset V$  which is invariant under all the symmetry operations of the group such that  $\Gamma(g)w \in W$  for all  $g \in G, w \in W$ . By doing so, the representation on the vector space  $V$  can be broken down into the sum of smaller representations on the subspace  $W_i$ . Each group uniquely has a denumerable number of such building-blocks representations called *irreducible representations*.

### 2.2.3 Applications

The symmetry group manifests in the equations describing the system. For instance, Schrödinger equations for electrons in a crystal has a point/space group of the crystal as its symmetry group[12]. The energy eigenspace of the equation  $H\Psi_n = E_n\Psi_n$  corresponds to the invariant subspace; i.e.  $\Gamma(g)\Psi_n$  is also the eigenstate of the same energy  $E_n$  since  $\Gamma(g)\{H\Psi_n\} = H\{\Gamma(g)\Psi_n\} = E_n\{\Gamma(g)\Psi_n\}$  for all  $g \in G$ . Therefore, the wavefunctions of each energy level should conform to the irreducible representation of symmetry group. Once the information on the irreducible representations is obtained, many fundamental properties are *a priory* determined, such as energy degeneracy, spatial/phase distributions of wavefunctions, and selection rule.

### 2.3 References

- [1] Jones R O 2015 *Rev. Mod. Phys.* 87 897–923
- [2] Slater J C 1951 *Phys. Rev.* 81 385–90
- [3] Becke A D 2014 *J. Chem. Phys.* 140 18A301
- [4] Hohenberg P and Kohn W 1964 *Phys. Rev.* 136 B864–71
- [5] Kohn W and Sham L J 1965 *Phys. Rev.* 140 A1133–8
- [6] Kohn W 1999 *Rev. Mod. Phys.* 71 1253–66

- [7] Ceperley D M and Alder B J 1980 *Phys. Rev. Lett.* 45 566–9
- [8] Perdew J P, Burke K and Ernzerhof M 1996 *Phys. Rev. Lett.* 77 3865–8
- [9] Grimme S 2011 *Wiley Interdiscip. Rev. Comput. Mol. Sci.* 1 211–28
- [10] Pinter C C 2010 *A book of abstract algebra* (Courier Corporation)
- [11] Jeevanjee N 2011 *An introduction to tensors and group theory for physicists* (Springer)
- [12] Tinkham M 2003 *Group theory and quantum mechanics* (Courier Corporation)

## CHAPTER 3

# EFFECT OF INTERFACE ON ELECTRON TRANSPORT IN SINGLE LAYER<sup>1</sup>

---

### 3.1 Introduction

Two-dimensional (2D) semiconducting materials may allow for high-performance and low-power consumption field effect transistors by virtue of the excellent electrostatic gate control over the extremely thin channel[1]. Among them, MoS<sub>2</sub> is considered to be suitable for switch device applications, showing extrinsic n-type conduction[2] with high intrinsic electron mobility

---

<sup>1</sup>This chapter is reprinted/adapted from the published work; J. Park et al., “Role of the Short-Range Order in Amorphous Oxide on MoS<sub>2</sub>/a-SiO<sub>2</sub> and MoS<sub>2</sub>/a-HfO<sub>2</sub> Interfaces”, *Phys. Status Solidi B* (2019), DOI: <https://doi.org/10.1002/pssb.201900002>. Wiley-VCH. Reproduced with permission. All rights reserved.

( $\approx 320\text{-}410\text{ cm}^2\text{ V}^{-1}\text{s}^{-1}$  at 300 K) and an appropriate band gap ( $\approx 1.8\text{ eV}$ )[3,4]. The carrier transport confined in 2D channel significantly depends on the type and contact properties of the gate dielectrics. For example, high- $k$  oxides like  $\text{HfO}_2$  have shown superior electron mobility over low- $k$  oxide like  $\text{SiO}_2$ , which is different from Si-based devices, which usually show degraded carrier mobility with high- $k$  dielectrics as compared with  $\text{SiO}_2$ [5,6]. This behavior has been attributed to the capability of high- $k$  oxide to suppress the charged impurity scattering from the impurity or sulfur vacancy in  $\text{MoS}_2$ [7–10]. It has been reported that the high- $k$  oxide induces stronger surface optical phonon scattering than  $\text{SiO}_2$ [11]. Therefore, the previously referenced positive effect of high- $k$  dielectrics on the carrier mobility may only be achieved when the defect density is higher than a certain critical value[11]. Nonetheless, possible effects of atomic interface structures on the carrier transport have not been dealt with in detail.

Since the surfaces of 2D materials like graphene and  $\text{MoS}_2$  are chemically inert due to the absence of surface dangling bonds[12,13], the surface properties of the contacting gate dielectric layer are assumed to dominate the properties of the interface between the two materials. In the case of graphene, the interface between graphene and  $\text{SiO}_2$  has strongly indicated the existence of interfacial bonds[14,15]. By contrast, the interfacial interaction of graphene with 2D hexagonal boron nitride was negligible by forming the van der Waals (vdW) interface[16,17]. In the case of  $\text{MoS}_2$ , the electronic

structure will be perturbed depending on the strength of the interaction at the interface, which is an important factor for carrier transport. For example, the interface with HfO<sub>2</sub> did not show covalent bonding[18]. However, to date, studies on the effect of interfacial structure between MoS<sub>2</sub> and gate dielectric materials have been rather limited.

In this work, the effects of the interface structures between MoS<sub>2</sub> and oxides on the electronic structures of MoS<sub>2</sub> are studied through ab-initio molecular dynamics calculations (AIMD). Amorphous SiO<sub>2</sub> (*a*-SiO<sub>2</sub>) and HfO<sub>2</sub> (*a*-HfO<sub>2</sub>) are selected as representatives of low-*k* and high-*k* oxides, respectively. The characteristics of interface structures are studied from the viewpoint of the short-range orders (SROs) of the two oxides. The MoS<sub>2</sub>/*a*-SiO<sub>2</sub> structure shows distinct interfacial bonds, by which the electronic structure of MoS<sub>2</sub> is significantly perturbed. By contrast, the MoS<sub>2</sub>/*a*-HfO<sub>2</sub> structure exhibits a weak non-covalent interaction at the interface, which results in the maintenance of the effective mass of MoS<sub>2</sub> as the free-standing form. This is rather counter-intuitive, considering the more ionic and active nature of HfO<sub>2</sub> as compared with SiO<sub>2</sub>, demonstrating the importance of this type of theoretical approach.

### 3.2 Simulation method

Bulk *a*-SiO<sub>2</sub> and *a*-HfO<sub>2</sub> structures were obtained by the melt-quenching

method[19]. The initial structures were a hexagonal periodic box with a cell size of  $a = 12.66 \text{ \AA}$  (corresponding to  $4 \times 4$  supercell of  $\text{MoS}_2$ ) and  $c = 12.00 \text{ \AA}$ , containing 111 and 129 atoms, respectively, for the purpose of compatibility with the hexagonal  $\text{MoS}_2$  cell. The initial atomic configurations were randomized at 5000 K for 10 ps and successively evolved at 3000 K for 10 ps. They were then quenched to 300 K and evolved for another 10 ps, then finally quenched to 0 K with the quenching rate of  $900 \text{ Kps}^{-1}$ [20]. This method resulted in well-converged amorphous structures showing the characteristic SRO. The final structures were fully relaxed at 0 K, until the atomic forces were less than  $0.01 \text{ eV\AA}^{-1}$ . The densities correspond to the experimental values of  $2.2 \text{ gcm}^{-3}$  for  $\alpha\text{-SiO}_2$ [21] and  $9.0 \text{ gcm}^{-3}$  for  $\alpha\text{-HfO}_2$ [22], respectively. The final amorphous oxide structure is combined with a monolayer  $\text{MoS}_2$  to form an interface structure where the  $\text{MoS}_2$  is surrounded by the oxide layer with the initial spacing of  $1.52 \text{ \AA}$  (about half of the interlayer gap in bulk  $\text{MoS}_2$ ) and relaxed. This sandwich interface structure makes the analysis of the interface energy and electronic structure simple and efficient due to the absence of the artificial surface states induced by vacuum region. The interface structures were annealed at 300, 1000, or 2000 K, and subsequently quenched and relaxed in a similar fashion. All calculations were performed by the Vienna Ab initio Simulation Package (VASP)[23] with the generalized gradient approximation parameterized by Perdew et al.[24] using the vdW corrections D3[25]. The AIMD was carried out with a cutoff energy of 300 eV and  $\Gamma$ -centered k-mesh. A higher cutoff

energy of 500 eV was adopted for both the structure relaxation and electronic structure calculation at 0 K. For the former calculation, the  $\Gamma$ -centered k-mesh was used, while the  $3\times 3\times 3$  k-mesh was used for the latter calculation.

### 3.3 Results and Discussion

#### 3.3.1 Short-range order of oxides

First, a significant difference in the intrinsic SRO between  $a$ -SiO<sub>2</sub> and  $a$ -HfO<sub>2</sub> was noted in their bulk forms. Figure 3.1(a) shows a bulk  $a$ -SiO<sub>2</sub> composed of the well-known corner-sharing SiO<sub>4</sub> tetrahedral network[21,20]. The calculated Si-O bond length is  $1.64 \pm 0.05$  Å (mean  $\pm$  standard deviation), and the coordination number of Si shows nearly zero variation with  $N_{\text{Si}} = 4.0 \pm 0.0$ . By contrast, the  $a$ -HfO<sub>2</sub> exhibits large variations in both Hf-O bond length of  $2.16 \pm 0.14$  Å and coordination number of  $N_{\text{Hf}} = 6.5 \pm 0.8$  with various connectivities of corner-, edge- and face- sharing of the oxygen polyhedron, as shown in Figure 1b, which is also consistent with the previous studies[22,26–28]. Such a difference in SRO will induce a significant difference in the interfacial structure and accompanying properties, which have yet to be addressed in detail. Figure 3.1(c) and (d) show the MoS<sub>2</sub>/ $a$ -SiO<sub>2</sub> and MoS<sub>2</sub>/ $a$ -HfO<sub>2</sub> interface structures, respectively, obtained by annealing at 1000 K for 50 ps. It is notable that the Si-S bonds and dangling O atoms are formed for the former, as indicated by arrows in Figure 3.1(c),

but the latter does not show these features.

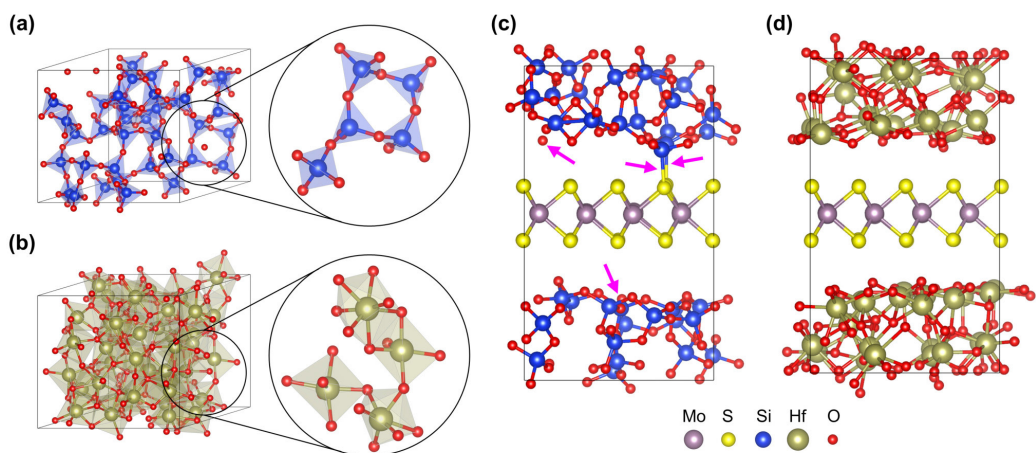


Figure 3.1 Atomic structures of bulk amorphous oxide and interface structure with  $\text{MoS}_2$ . Short-range order of (a)  $a\text{-SiO}_2$  showing the distinct  $\text{SiO}_4$  tetrahedral network and (b)  $a\text{-HfO}_2$  showing various coordination numbers and polyhedral connectivities. Interface structures of (c)  $\text{MoS}_2/a\text{-SiO}_2$  and  $\text{MoS}_2/a\text{-HfO}_2$  obtained by annealing at 1000 K for 50 ps. The Si-S bonds and dangling O atoms are indicated by arrows in (c).

Figure 3.2(a), (b) show the evolution in the coordination numbers of Si, Hf, and S atoms ( $N_{\text{Si}}$ ,  $N_{\text{Hf}}$ , and  $N_{\text{S}}$ ) and interface energies ( $\gamma$ ) of  $\text{MoS}_2/a\text{-SiO}_2$  and  $\text{MoS}_2/a\text{-HfO}_2$ , respectively, after annealing at 300, 1000, and 2000 K. Although 1000 and 2000 K are much higher than the experimental temperature range for device fabrication (400–700 K)[10], taking these temperatures was necessary for examining the evolution of structural features within reasonable computational steps. The interface energy is defined as  $\gamma = (E_{\text{interface}} - E_{\text{MoS}_2} - E_{\text{oxide}}) / 2A$ , where  $E_{\text{interface}}$ ,  $E_{\text{MoS}_2}$ , and  $E_{\text{oxide}}$  are the total energies of the interface structure, free-standing  $\text{MoS}_2$ , and bulk amorphous oxide, respectively, and  $A$  is the interface area. The  $\gamma$  measures the degree of stability of the interface associated with the reconstruction of the interface atomic structure such as formation, breaking, or distortion of chemical bonds. For all of the interface structures, the bond length of Mo-S ( $2.40 \pm 0.05 \text{ \AA}$ ) is almost the same as that of free-standing  $\text{MoS}_2$  ( $2.41 \pm 0.00 \text{ \AA}$ ), indicating the absence of stress on the  $\text{MoS}_2$ . This could be attributed to the absence of strain between the two contacting materials due to the amorphous nature of the oxide layers, which can rather easily accommodate the structural mismatch by the local distortion of the interfacial bonds.

For all of the annealing conditions, the coordination number of Si was maintained almost constantly at 4, as shown for  $\text{MoS}_2/a\text{-SiO}_2$  structures in Figure 3.2(a). By contrast, the  $N_{\text{S}}$  is initially significantly higher than 3, which is the value of the free-standing  $\text{MoS}_2$ , and gradually decreases to 3 by

annealing, especially at high temperature. At 300 K, such structural relaxation can hardly be observed due to the extremely slow kinetic process. The Si atoms at the  $\alpha$ -SiO<sub>2</sub> surface maintain the tetrahedral coordination. Even some Si atoms, which are presumed to be 3-fold Si ( $\equiv\text{Si}\cdot$ ) atoms generated by breaking the periodic boundary condition of the bulk  $\alpha$ -SiO<sub>2</sub>, recover the tetrahedral coordination by forming Si-S bonds ( $\equiv\text{Si-S}-(\text{MoS}_2)$ ) at the interface, as shown in Figure 1c. Further annealing removes the interface Si-S bonds and promotes the formation of siloxane group by  $\equiv\text{Si}\cdot + \cdot\text{O-Si}\equiv \rightarrow \equiv\text{Si-O-Si}\equiv$ . This results in decreased interface energy, as shown in the lower panel of Figure 3.2(a). However, interfacial defects, such as Si-S bond and 1-fold dangling O atom ( $\equiv\text{Si-O}\cdot$ ) (which may also appear due to the broken periodic boundary condition of the bulk  $\alpha$ -SiO<sub>2</sub>), were not entirely removed from all of the interface structures in this simulation set. The Si-S bonds lengths are 2.24 and 2.35 Å, which are slightly longer than the value of 2.13 Å found in SiS<sub>2</sub>[29].

By contrast, for the MoS<sub>2</sub>/ $\alpha$ -HfO<sub>2</sub>, the coordination number of Hf is significantly lower than the corresponding bulk value for all temperatures and annealing times (the mean and standard deviation for the bulk  $\alpha$ -HfO<sub>2</sub> are shown as the dashed line and shade, respectively), as shown in the upper panel of Figure 3.2(b). This is caused by the bond breaking at the surface and consistent with the finding that the  $N_s$  remains near 3 at all annealing temperatures and times, indicating the absence of the strong covalent

interaction between MoS<sub>2</sub> and *a*-HfO<sub>2</sub>. These findings indicate that the interaction between MoS<sub>2</sub> and *a*-HfO<sub>2</sub> is weak, presumably due to the flexible SRO of *a*-HfO<sub>2</sub>. This is accompanied by generally lower interface energies than those of MoS<sub>2</sub>/*a*-SiO<sub>2</sub>, as shown in the lower panel of Figure 3.2(b). The interface energy of MoS<sub>2</sub>/*a*-HfO<sub>2</sub> decreases by annealing at 1000 K and 2000 K presumably due to the relaxation of the atomic structure within the HfO<sub>2</sub> layer, which involves slight reductions in both the mean value of the coordination number of Hf atoms and its standard deviation. This type of relaxation is not observed at 300 K due to the slow kinetics.

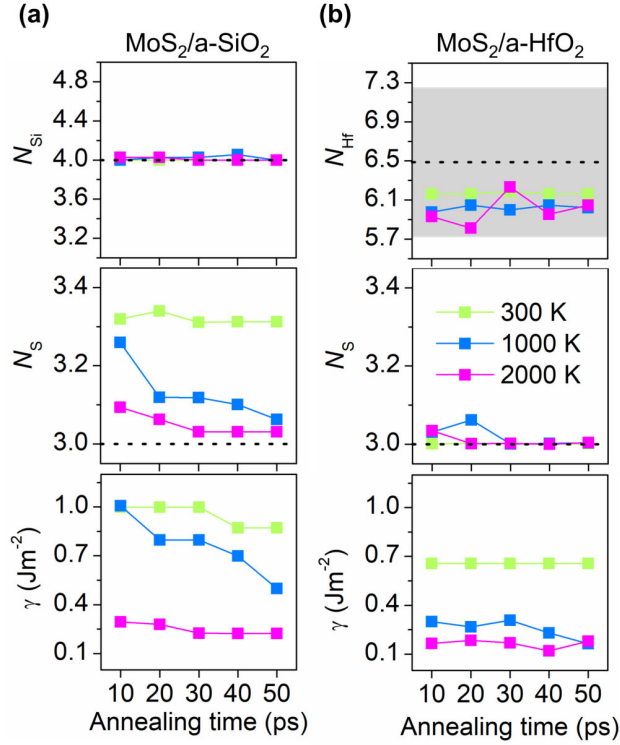


Figure 3.2 Evolution of interface atomic structure and interface energy for MoS<sub>2</sub>/a-SiO<sub>2</sub> and (b) MoS<sub>2</sub>/a-HfO<sub>2</sub> along the annealing time at different annealing temperatures.  $N_{Si}$ ,  $N_{Hf}$ , and  $N_S$  are the coordination numbers of Si, Hf, and S atoms, respectively. The dashed lines are the corresponding values for bulk a-SiO<sub>2</sub>, bulk a-HfO<sub>2</sub>, and free-standing MoS<sub>2</sub>. The shaded region in (b) indicates the standard deviation of  $N_{Hf}$  in Bulk a-HfO<sub>2</sub>.

### 3.3.2 Effect of interface on band dispersion

The electronic structures of the two interface structures are also examined based on the Brillouin zone of MoS<sub>2</sub>, as shown in Figure 3.3(a), since the band structure of MoS<sub>2</sub> in 4×4 supercell is folded into the smaller Brillouin zone (orange). The conduction band minimum (CBM) and valence band maximum (VBM) of the free-standing MoS<sub>2</sub> appear at *K* point, as shown in Figure 3.3(b). Figure 3.3(c) shows the local charge distribution of the free-standing MoS<sub>2</sub> layer, where the wavefunction of CBM mainly consists of Mo  $4d_{z^2}$  states. The electron effective mass  $m_e^*$ , as estimated by the parabolic fitting at *K* point, is  $m_e^* = 0.46$ .

In MoS<sub>2</sub>/*a*-SiO<sub>2</sub>, the CB dispersion is significantly flattened, resulting in the increased effective mass of  $m_e^* = 0.63$  shown in Figure 3.3(d). The interface Si-S bond, as indicated by an arrow in Figure 3.3(e), severely distorts the wavefunction of MoS<sub>2</sub> and is attributed to the increased effective mass of MoS<sub>2</sub>. In addition, MoS<sub>2</sub>/*a*-SiO<sub>2</sub> shows several occupied O  $2p$  states originating from the O dangling bonds below approximately 0.1 eV and 1.0 eV from the Fermi level  $E_F$ , shown in Figure 3d. By contrast, the dispersion of the CB of MoS<sub>2</sub>/*a*-HfO<sub>2</sub> shown in Figure 3.3(f) is remarkably similar to that of the free-standing MoS<sub>2</sub>, resulting in the  $m_e^* = 0.47$ . Correspondingly, the wavefunction of the CBM in MoS<sub>2</sub>/*a*-HfO<sub>2</sub> in Figure 3.3(g) is almost identical to that of free-standing MoS<sub>2</sub>, and there is no involvement of the gap

states.

It is noted that the position of the VBM changes to the  $\Gamma$  point in the MoS<sub>2</sub>/*a*-SiO<sub>2</sub> and MoS<sub>2</sub>/*a*-HfO<sub>2</sub> structures. This is because the valence band states of MoS<sub>2</sub> near the  $\Gamma$  point has a contribution from the out-of-plane S  $3p_z$  orbitals, which are susceptible to the electron cloud from the neighboring oxide layers[30]. Thus, the change in the VBM position can be attributed to the non-covalent interaction, which was also observed in the multilayer MoS<sub>2</sub> bonded by the vdW interaction[30].

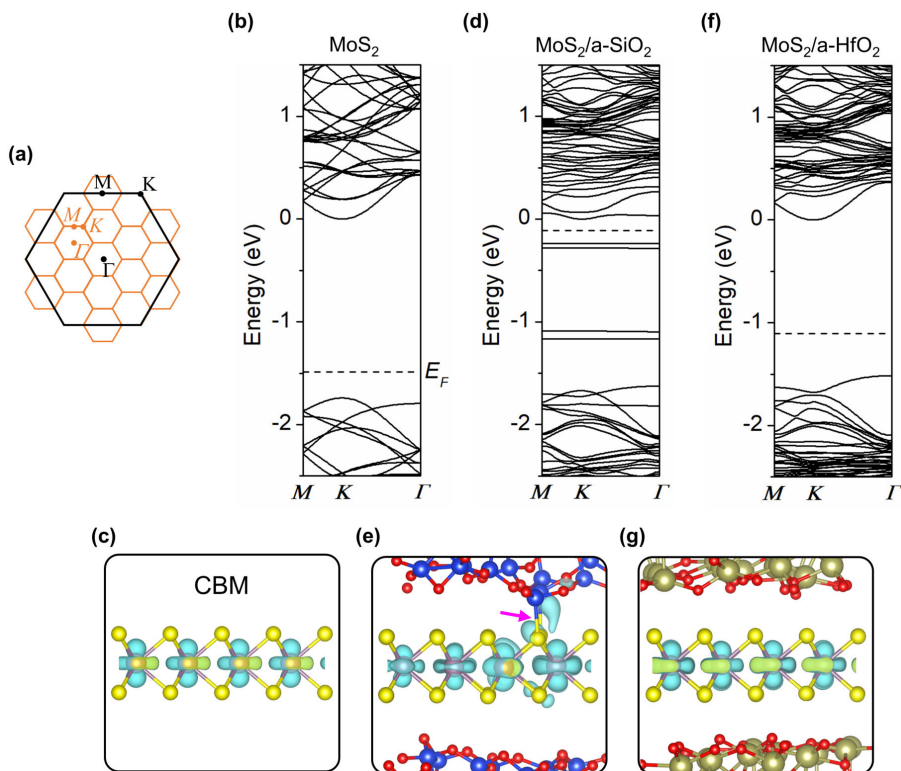


Figure 3.3 Comparison of the electronic properties of the interface structures with free-standing MoS<sub>2</sub>. The interface structures correspond to the structures shown in Figure 3.1(c) and (d). (a) High-symmetry points in the folded Brillouin zone (orange) of MoS<sub>2</sub> in 4x4 supercell. Band structure and wavefunction of the conduction band minimum for (b, c) free-standing MoS<sub>2</sub>, (d, e) MoS<sub>2</sub>/a-SiO<sub>2</sub> and (f, g) MoS<sub>2</sub>/a-HfO<sub>2</sub> structures. The Si-S bonds in MoS<sub>2</sub>/a-SiO<sub>2</sub> are denoted by the arrow in (e).

The obvious contrast in the characteristics of the SRO between the two bulk amorphous oxides is suggested to induce the different responses to the bond breaking and the interface structure with MoS<sub>2</sub>. The strict SRO in *a*-SiO<sub>2</sub> implies a strong driving force to retain the tetrahedral coordination of Si atoms. When the surface of *a*-SiO<sub>2</sub> is reconstructed by itself, which corresponds to the formation of siloxane group, the interaction with MoS<sub>2</sub> will be weak. Such self-reconstruction of *a*-SiO<sub>2</sub> surface may result in lowered interface energy, as shown in Figure 3.2(a). However, in a certain intermediate case, some surface Si atoms readily bond to the S atoms to have the tetrahedral coordination by the reaction,  $\equiv\text{Si}\cdot + \text{S}-(\text{MoS}_2) \rightarrow \equiv\text{Si}-\text{S}-(\text{MoS}_2)$ , leaving an O atom with a dangling bond (which may not covalently bond to S anions). The Si-S bonds significantly affect the electronic effective mass and the dangling O atoms introduce the gap states in the band gap of MoS<sub>2</sub>. Under the typical MoS<sub>2</sub> device fabrication conditions[10], the surface of SiO<sub>2</sub> is not fully covered with siloxane group but with coexisting hydroxyl group[31] or hydrogenated bonds[32]. Such a surface may induce broken bonds at the surface during the fabrication process, as in the initial interface structures shown in this work. Therefore, *a*-SiO<sub>2</sub> is prone to deteriorate MoS<sub>2</sub> channel.

By contrast, the flexible SRO in *a*-HfO<sub>2</sub> means that ions in this material can accommodate the change in the local chemical environment. It is, therefore, less probable that defects will be formed at the surface or interface.

Furthermore, it may marginally disturb MoS<sub>2</sub> even when the interface forms. The similar result was obtained for the interface between MoS<sub>2</sub> and the high-*k* Al<sub>2</sub>O<sub>3</sub> exhibiting flexible SRO (see Appendix 3.5.1). A previous density functional theory (DFT) study also showed weak interaction between *a*-HfO<sub>2</sub> and MoS<sub>2</sub>, but did not analyze the band structure and effective mass[33]. A similar DFT study using artificially strained crystalline HfO<sub>2</sub> substrate showed a considerable increase in effective mass of MoS<sub>2</sub>[34], which is inconsistent with the experimentally observed high mobility using HfO<sub>2</sub>[7–10]. It is possible that the actual interface may contain thin amorphous-like or at least distorted structure from the assumed strained crystalline one.

### 3.4 Conclusion

In summary, the interfaces between MoS<sub>2</sub> and two amorphous oxides (SiO<sub>2</sub> and HfO<sub>2</sub>) with contrasting characteristics of the intrinsic short-range order (SRO) are examined using ab-initio molecular dynamics calculations. The amorphous SiO<sub>2</sub> with the strict SRO shows strong interaction with MoS<sub>2</sub>, resulting in the interfacial bonds of Si-S and dangling oxygen atoms accompanying a significant increase in the effective mass of MoS<sub>2</sub>. On the other hand, the amorphous HfO<sub>2</sub> showing the flexible SRO weakly interacts with MoS<sub>2</sub> and preserves the band dispersion and effective mass of MoS<sub>2</sub> as its free-standing state. These results reveal possible reasons for the higher

carrier mobility of MoS<sub>2</sub> when it is in contact with HfO<sub>2</sub> gate dielectric over SiO<sub>2</sub> from the viewpoint of the interfacial atomic structure.

## 3.5 Appendix

### 3.5.1 MoS<sub>2</sub>/a-Al<sub>2</sub>O<sub>3</sub> interface

The MoS<sub>2</sub> transistors using the high- $k$  Al<sub>2</sub>O<sub>3</sub> as the gate oxide has shown superior mobility which, like the HfO<sub>2</sub> case, has been attributed to the suppression of the Coulombic impurity scattering [9,10]. We investigated the atomic and electronic structures of the interface between the MoS<sub>2</sub> and the amorphous Al<sub>2</sub>O<sub>3</sub> (a-Al<sub>2</sub>O<sub>3</sub>) in a similar fashion. We adopted the density of the bulk a-Al<sub>2</sub>O<sub>3</sub> structure as 3.0 gcm<sup>-3</sup> which is in the range of reported values[35–37]. First, the bulk a-Al<sub>2</sub>O<sub>3</sub> structure shows large variations in Al-O bond length of  $1.85 \pm 0.09$  Å and coordination number  $N_{\text{Al}} = 4.5 \pm 0.53$  (Figure 3.4(a)), which is consistent with the previous reports[35–37]. The connectivity between Al-O polyhedra is dominated by the corner- and edge-sharing networks. The results indicate the SRO of Al<sub>2</sub>O<sub>3</sub> is rather flexible like a-HfO<sub>2</sub>. The MoS<sub>2</sub>/a-Al<sub>2</sub>O<sub>3</sub> interface structures exhibit no interface chemical bonds (Figure 3.4(b)) and, consequently, the unperturbed conduction band dispersion (Figure 3.4(c)) and wavefunction (Figure 3.4(d)).

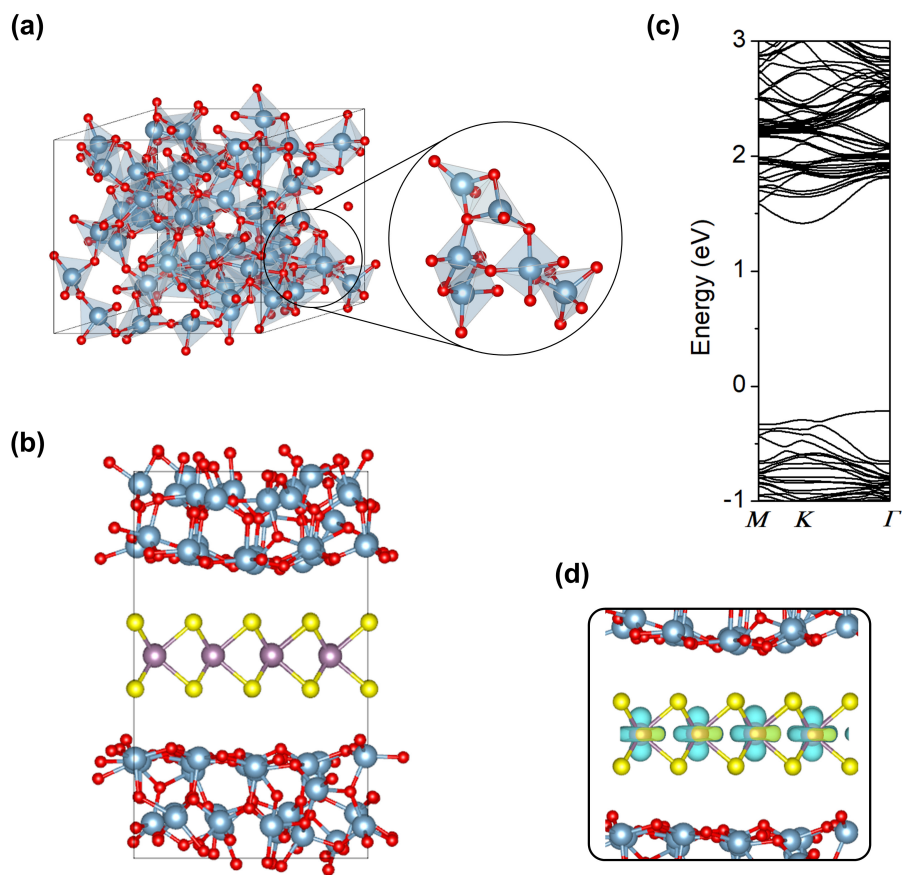


Figure 3.4 (a) Short-range order of bulk  $\alpha\text{-Al}_2\text{O}_3$  structure. (b) Snapshot of  $\text{MoS}_2/\alpha\text{-Al}_2\text{O}_3$  interface structure annealed at 1000 K for 50 ps. (c) Electronic band structure of the interface structure. Zero-energy corresponds to the Fermi level (d) Plot of wavefunction corresponding to the CBM.

### 3.6 References

- [1] G. Fiori, F. Bonaccorso, G. Iannaccone, T. Palacios, D. Neumaier, A. Seabaugh, S. K. Banerjee, L. Colombo, *Nat. Nanotechnol.* 2014, 9, 768.
- [2] Y. Kang, S. Han, *Nanoscale* 2017, 9, 4265.
- [3] K. Kaasbjerg, K. S. Thygesen, K. W. Jacobsen, *Phys. Rev. B* 2012, 85, 115317.
- [4] X. Li, J. T. Mullen, Z. Jin, K. M. Borysenko, M. Buongiorno Nardelli, K. W. Kim, *Phys. Rev. B* 2013, 87, 115418.
- [5] G. D. Wilk, R. M. Wallace, J. M. Anthony, *J. Appl. Phys.* 2001, 89, 5243.
- [6] R. Chau, J. Brask, S. Datta, G. Dewey, M. Doczy, B. Doyle, J. Kavalieros, B. Jin, M. Metz, A. Majumdar, M. Radosavljevic, *Microelectron. Eng.* 2005, 80,1.
- [7] B. Radisavljevic, A. Radenovic, J. Brivio, V. Giacometti, A. Kis, *Nat. Nanotechnol.* 2011, 6, 147.
- [8] Z. Yu, Y. Pan, Y. Shen, Z. Wang, Z.-Y. Ong, T. Xu, R. Xin, L. Pan, B. Wang, L. Sun, J. Wang, G. Zhang, Y. W. Zhang, Y. Shi, X. Wang, *Nat. Commun.* 2014, 5, 5290.
- [9] Z. Yu, Z.-Y. Ong, Y. Pan, Y. Cui, R. Xin, Y. Shi, B. Wang, Y. Wu, T. Chen, Y.-W. Zhang, G. Zhang, X. Wang, *Adv. Mater.* 2016, 28, 547.
- [10] S.-L. Li, K. Tsukagoshi, E. Orgiu, P. Samorì, *Chem. Soc. Rev.* 2016, 45, 118.

- [11] N. Ma, D. Jena, *Phys. Rev. X* 2014, 4, 011043.
- [12] V. Georgakilas, M. Otyepka, A. B. Bourlinos, V. Chandra, N. Kim, K. C. Kemp, P. Hobza, R. Zboril, K. S. Kim, *Chem. Rev.* 2012, 112, 6156.
- [13] M. Chhowalla, H. S. Shin, G. Eda, L.-J. Li, K. P. Loh, H. Zhang, *Nat. Chem.* 2013, 5, 263.
- [14] K. Nagashio, T. Yamashita, T. Nishimura, K. Kita, A. Toriumi, *J. Appl. Phys.* 2011, 110, 024513.
- [15] S. Das, D. Lahiri, A. Agarwal, W. Choi, *Nanotechnology* 2014, 25, 045707.
- [16] C. R. Dean, A. F. Young, I. Meric, C. Lee, L. Wang, S. Sorgenfrei, K. Watanabe, T. Taniguchi, P. Kim, K. L. Shepard, J. Hone, *Nat. Nanotechnol.* 2010, 5, 722.
- [17] X. Cui, G.-H. Lee, Y. D. Kim, G. Arefe, P. Y. Huang, C.- H. Lee, D. A. Chenet, X. Zhang, L. Wang, F. Ye, F. Pizzocchero, B. S. Jessen, K. Watanabe, T. Taniguchi, D. A. Muller, T. Low, P. Kim, J. Hone, *Nat. Nanotechnol.* 2015, 10, 534.
- [18] S. McDonnell, B. Brennan, A. Azcatl, N. Lu, H. Dong, C. Buie, J. Kim, C. L. Hinkle, M. J. Kim, R. M. Wallace, *ACS Nano* 2013, 7, 10354.
- [19] J. Lee, D.-Y. Cho, J. Jung, U. K. Kim, S. H. Rha, C. S. Hwang, J.- H. Choi, *Appl. Phys. Lett.* 2013, 102, 242111.
- [20] J. Sarnthein, A. Pasquarello, R. Car, *Phys. Rev. B* 1995, 52, 12690.
- [21] A. Pasquarello, R. Car, *Phys. Rev. Lett.* 1997, 79, 1766.
- [22] P. Broqvist, A. Alkauskas, J. Godet, A. Pasquarello, *J. Appl. Phys.* 2009,

105, 061603.

- [23] G. Kresse, J. Furthmüller, *Phys. Rev. B* 1996, 54, 11169.
- [24] J. P. Perdew, K. Burke, M. Ernzerhof, *Phys. Rev. Lett.* 1996, 77, 3865.
- [25] S.Grimme, J.Antony,S.Ehrlich,H.Krieg, *J. Chem. Phys.* 2010, 132, 154104.
- [26] W. L. Scopel, A. J. R. da Silva, A. Fazzio, *Phys. Rev. B* 2008, 77, 172101.
- [27] T.-J. Chen, C.-L. Kuo, *J. Appl. Phys.* 2011, 110, 064105.
- [28] G. Broglia, G. Ori, L. Larcher, M. Montorsi, *Model. Simul. Mater. Sci. Eng.* 2014, 22, 065006.
- [29] J. Peters, B. Krebs, *Acta Crystallogr. Sect. B, Struct. Crystallogr. Cryst. Chem.* 1982, 38, 1270.
- [30] G.-b. Liu, D. Xiao, Y. Yao, X. Xu, W. Yao, *Chem. Soc. Rev.* 2015, 44, 2643.
- [31] L. Zhuravlev, *Colloids Surfaces A, Physicochem. Eng. Asp.* 2000, 173,1.
- [32] A. G. Revesz, *J. Electrochem. Soc.* 1979, 126, 122.
- [33] W. L. Scopel, R. H. Miwa, T. M. Schmidt, P. Venezuela, *J. Appl. Phys.* 2015, 117, 194303.
- [34] M. Yang, J. W. Chai, M. Callsen, J. Zhou, T. Yang, T. T. Song, J. S. Pan, D. Z. Chi, Y. P. Feng, S. J. Wang, *J. Phys. Chem. C* 2016, 120, 9804.
- [35] Shi C, Alderman O L G, Berman D, Du J, Neufeind J, Tamalonis A, Weber J K R, You J and Benmore C J 2019 *Front. Mater.* **6** 1–15
- [36] Davis S and Gutiérrez G 2011 *J. Phys. Condens. Matter* **23** 495401
- [37] Gutiérrez G and Johansson B 2002 *Phys. Rev. B* **65** 104202

# CHAPTER 4

## EFFECT OF SYMMETRY ON VALLEYTRONICS OF MULTILAYER STRUCTURE<sup>2</sup>

---

### 4.1 Introduction

Two-dimensional (2D) materials serve as the primary testbeds where attempts to utilize the quantum degrees of freedom (DoFs) beyond the electronic charge are currently very active. Provided that the proper framework of manipulating the DoFs is given, it can be harnessed as information carriers to construct new types of the logic device[1, 2]. In 2D transition metal

---

<sup>2</sup>This chapter is reprinted/adapted from the published work; J. Park et al., “Optical control of the layer degree of freedom through Wannier–Stark states in polar 3R MoS<sub>2</sub>”, *Journal of Physics: Condensed Matter* 31 (2019) 315502. IOP Publishing. Reproduced with permission. All rights reserved.

dichalcogenide (TMDC), the crystal momentum of Bloch electrons associated with the corners of the hexagonal Brillouin zone comprises the binary information carriers called valley-index  $\tau = \{K, -K\}$ [3]. In non-centrosymmetric crystals, opposite valley-indexes are associated with the opposite crystal angular momentum (CAM). The optical operation on the valley-index exploits the valley-contrasting circular dichroism by which one can selectively populate each valley with carriers (valley-polarization)[4].

In the multilayer structure, electrons gain an additional DoF associated with the discrete position among the layers. It can be defined as the layer-index  $n = \{1, 2, \dots, N\}$ , where  $N$  layers are stacked along the  $z$ -axis as shown in Figure 4.1(a), and is coupled with electric polarization[1, 5, 6]. In this case, controlling the layer-index corresponds to inducing an upward ( $\Delta n = +1$ ) or downward ( $\Delta n = -1$ ) motion of the electrons along the  $z$ -axis in a selective and precise manner. Recently, the interlayer charge transfer after the optical pumping in the bilayer heterostructures has attracted much attention[7–17]. However, the interlayer motion of charges therein was one-way (say,  $\Delta n = -1$  only) according to the energy relaxation under the type II band alignment, hence it is irreversible. It means that the most natural DoF (layer-index,  $n$ ) in layered structure has not been treated as fully controllable one.

The controllability of the layer-index, like the valley-index, is expected to be closely intertwined with the symmetry of the structure. In this work, we study the role of crystallographic symmetry on the characteristics of the layer-index

and its control in TMDC using density functional theory (DFT) and group theory calculations. The presence of the spontaneous electric polarization was found in 3R MoS<sub>2</sub> having polar symmetry which has not been reported yet to the authors' knowledge. The uniform built-in field from the electric polarization leads the Wannier-Stark (WS) type localization of Bloch wavefunctions at the *K* valleys in 3R as shown in Figure 4.1(b). It is pointed out that the double group symmetry strengthens the confinement via interplay between spin-orbit coupling (SOC) and the built-in field. Thus, the localization mechanism differs from the previous understanding based on single group analysis[18, 19]. Next, we show an unique interband selection rule for the interlayer motion which appears exclusively in 3R homostructure induced from its crystallographic symmetry. In particular, infrared frequency irradiation induces the optical interlayer charge transfer of both electrons and holes against the built-in field ( $\Delta n = +1$ ). This excitation channel enables the reversible interlayer motion in conjunction with the interlayer transition ( $\Delta n = -1$ ) at the visible regime. The results propose a simple and efficient route for the optical controlling of layer-index ( $\Delta n = \pm 1$ ) using a dual-frequency (visible and infrared regimes) light source.

## 4.2 Method; DFT calculation

The atomic and electronic structures of the 3R and 2H MoS<sub>2</sub> were calculated

based on the DFT, using the Vienna Ab-initio Simulation Package (VASP)[20, 21]. Both the local density approximation (LDA) parameterized by Ceperley *et al.*[22], and the generalized gradient approximation parameterized by Perdew *et al.*[23] with the van der Waals (vdW) corrections (PBE-D2[24] and PBE-D3[25]) were used. The projector-augmented wave (PAW) method[26] and the cut-off energy of 500 eV were used with the valence electron configurations of Mo ( $4s^2 4p^6 5s^2 4d^4$ ) and S ( $3s^2 3p^4$ ), respectively. For the bulk 3R and 2H structures, the  $\Gamma$ -centered  $24 \times 24 \times 5$  and  $24 \times 24 \times 6$  k-meshes were used, respectively. For the slab structures consisting of finite layers (two to five layers) and at least 20-Å-thick vacuum, the  $24 \times 24 \times 1$  k-mesh was chosen. All the structures were fully relaxed until the Hellmann- Feynman forces on the atoms were less than  $0.001 \text{ eV}\text{\AA}^{-1}$ . The spontaneous polarization was calculated by the Berry phase method[27]. The dielectric tensors and Born effective charge tensors were calculated via the density functional perturbation theory including the local field effect[28, 29]. All the calculated values, such as the structural parameters, band structures, spontaneous polarizations, potential profiles, and dielectric tensors, were crosschecked using the Quantum-Espresso (QE) package[30, 31], and a good agreement was confirmed. Accordingly, the expectation value of the spin operator  $\langle S_z \rangle$  of the SOC band structure was calculated using the QE package. The external electric field on the slab structure was simulated adding artificial dipole sheet in the vacuum region[32].

## 4.3 Results and Discussion

### 4.3.1 Spontaneous polarization of 3R MoS<sub>2</sub>

The symmetry of the layered crystal is determined by the configuration of the constituent layers. The configuration of a layer (e.g., **A**, **B**, and **C**) can be defined by the sequential positions of Mo and S atoms projected onto the close-packed positions in the hexagonal primitive cell shown in Figure 4.1(a) (i. e., **A**, **B**, and **C** correspond to *cAc*, *aBa*, and *bCb* stackings, respectively, where the lower case represents the position of S atoms and the upper case represents that of Mo atoms). Likewise, the configurations of a layer  $\bar{\mathbf{A}}$ ,  $\bar{\mathbf{B}}$ , and  $\bar{\mathbf{C}}$  correspond to *bAb*, *cBc*, and *aCa* stackings, respectively. In this notation, the 3R structure is specified as **BCA**... and the 2H structure is specified as  $\bar{\mathbf{B}}\bar{\mathbf{C}}$ .... The polar symmetry of material permits the spontaneous electric polarization. The 3R structure has the polar symmetry (*R3m* for bulk and *P3m1* for finite layers[35]) with the polar axis along the z-axis. The Berry phase calculation verifies the finite spontaneous polarization  $P_s$  in accordance with the polar symmetry as shown in the upper panel in Figure 4.1(c) (See section 4.5.1 for calculation details). The direction of the spontaneous polarization is downward ([001]) in the **BCA**... stacking and upward ([001]) in the **BAC**... stacking. The magnitude of  $P_s$  increases with the number of layers and saturates to 0.59-1.15  $\mu\text{Ccm}^{-2}$  at the bulk structure (dashed line). The values are comparable to those of the wurtzite-structure III-V compounds

(e.g.,  $1.8 \mu\text{Ccm}^{-2}$  in GaN and  $1.1 \mu\text{Ccm}^{-2}$  in InN, respectively[36]). The functional dependency is attributed to the difference in the interlayer distance  $d$  which is susceptible to the strength of vdW interaction described by the exchange-correlation functional.

The spontaneous polarization provokes the macroscopic built-in potential in opposite direction (e.g., [001] in **BCA**... stacking). For finite layers, the potential across the top and bottom layers  $V_{built-in}$  linearly increases with the number of layers as shown in the lower panel in Figure 4.1(c). The increment corresponds to the interlayer potential  $\varphi \sim 55\text{-}84$  meV between neighboring layers. The corresponding electric field was estimated to be  $E_{built-in} \approx \varphi / d \sim 0.88\text{-}1.40$  MVcm<sup>-1</sup>, assuming  $d \sim 6.00\text{-}6.20$  Å. The bulk structure simulated by the periodic boundary condition does not directly show the electric field due to the absence of the surface bound charge. Nonetheless, the electric field associated with the uniform polarization can be estimated to be  $E_{built-in} = -P_s / \varepsilon_{\parallel} \varepsilon_0$ , where  $\varepsilon_{\parallel}$  and  $\varepsilon_0$  are the bulk static dielectric tensor component parallel to the z-axis and the vacuum permittivity, respectively[37]. Table 4.1 shows relevant parameters for the bulk structure. The calculated  $E_{built-in}$  is  $1.02\text{-}1.59$  MVcm<sup>-1</sup> depending on the functionals adopted for calculation, which are in a reasonable agreement with the value calculated for the finite layers. It is also noted that the reduction of the dielectric screening with decreasing thickness of 2D materials bound by weak vdW interaction[38, 39] may explain the fact that the finite layers of 3R

structure, despite its reduced  $P_s$ , develops the built-in field whose magnitude is almost similar to the that of bulk. These results corroborate the persistent existence of spontaneous polarization in the 3R structure irrespective of the number of stacking layers.

To date, the presence of the  $P_s$  in several TMDC materials has been neglected based on the horizontal mirror symmetry of the  $\text{MoS}_6$  trigonal prism in the individual layer[40, 41]. This is the case for the 2H structure which has a non-polar symmetry ( $P6_3mmc$  for bulk,  $P\bar{6}m2$  for finite odd layers, and  $P\bar{3}m1$  for finite even layers[35]) as can be confirmed from the calculation results shown in Table 4.1. The presence of mirror symmetry in the 2H structure is corroborated by the fact that the lower and upper S atoms,  $S_1$  and  $S_2$ , in a constituent layer show identical Born effective charge of  $Z_{zz}^*(S_1)$  and  $Z_{zz}^*(S_2)$ , respectively. However, in the 3R structure, the horizontal mirror symmetry of the constituent layer is broken by the asymmetric vdW interaction between neighboring layers. Thus, the Born effective charges of upper and lower S atoms are asymmetric in Table 4.1, which is in accordance with the polar symmetry of the 3R structure.

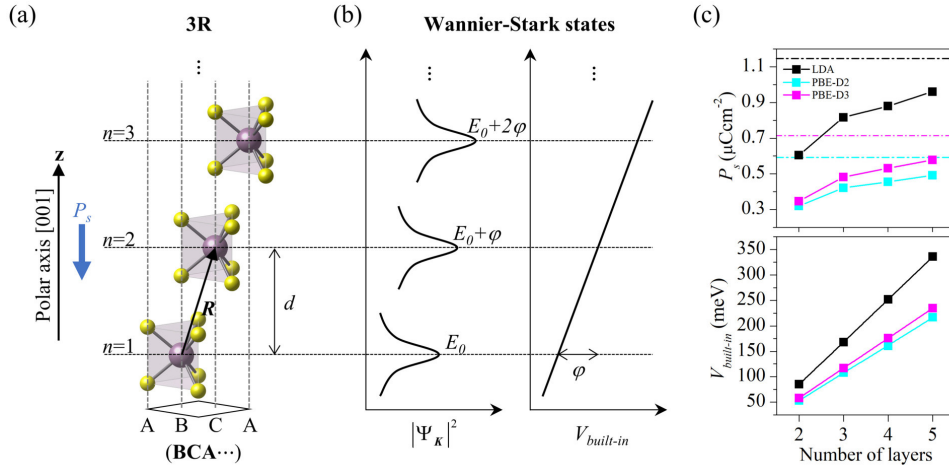


Figure 4.1 Layer-index of polar 3R MoS<sub>2</sub>. (a) The layer-index  $n$  is defined over layers stacked with the interlayer spacing  $d$  along the polar axis [001]. The direction of the spontaneous electric polarization  $P_s$  is downward ([001]) in BCA... stacking. All the layers are crystallographically equivalent by the rhombohedral translational symmetry  $R$  in the periodic bulk structure. (b) The Wannier-Stark states confined in each layer under the uniform built-in potential  $V_{built-in}$  with the energy splitting corresponding to the interlayer potential  $\phi$ . (c) The magnitude of  $P_s$  and  $V_{built-in}$  calculated by DFT as a function of the number of layers. The  $P_s$  asymptotically reaches the bulk value (dashed line) with the number of layers. The potential between the top and bottom layers increases linearly by the interlayer potential  $\phi$ .

Table 4.1 Calculated structural and electronic properties of the bulk 3R and 2H MoS<sub>2</sub> in comparison with experimental data.

Stacking	Method	$a$	$c$	$d$	$\epsilon_{\parallel}$	$\epsilon_{\perp}$	$P_s$	$E_{built-in}$	$Z_{zz}^*(Mo)$	$Z_{zz}^*(S_1)$	$Z_{zz}^*(S_2)$
Bulk 3R	LDA	3.13	17.81	5.94	8.2	15.9	1.15	1.59	0.97	-0.57	-0.41
	PBE-D2	3.19	18.39	6.13	6.6	15.6	0.59	1.02	0.68	-0.39	-0.30
	PBE-D3	3.16	18.24	6.08	7.0	15.6	0.71	1.15	0.72	-0.41	-0.31
	Exp.	3.16 <sup>[33]</sup>	18.37 <sup>[33]</sup>	6.12 <sup>[33]</sup>	-	-	-	-	-	-	-
Bulk 2H	LDA	3.12	11.98	5.99	7.7	15.6	0	0	0.87	-0.44	-0.44
	PBE-D2	3.19	12.31	6.16	6.4	15.4	0	0	0.64	-0.32	-0.32
	PBE-D3	3.16	12.23	6.11	6.7	15.4	0	0	0.67	-0.34	-0.34
	Exp.	3.16 <sup>[33]</sup>	12.30 <sup>[33]</sup>	6.15 <sup>[33]</sup>	7.0 <sup>[34]</sup>	-	-	-	-	-	-

Lattice constants  $a$  and  $c$  and interlayer distance  $d$  are given in unit of Å.  $\epsilon_{\parallel}$  and  $\epsilon_{\perp}$  are the static dielectric tensor components parallel and perpendicular to the [001] axis, respectively. For the spontaneous polarization  $P_s$  ( $\mu\text{Ccm}^{-2}$ ) and internal field  $E_{built-in}$  ( $\text{MVcm}^{-1}$ ), only the magnitudes are given and their directions depending on the stacking sequence are described in the main text. The Born effective charge tensor components  $Z_{zz}^*$  are given for the Mo, and lower ( $S_1$ ) and upper ( $S_2$ ) S atoms comprising the MoS<sub>6</sub> trigonal prism.

### 4.3.2 Localization mechanism of $K$ valley states

In order to precisely encode the layer information, it is necessary to confine carriers within the individual layer (layer thickness of  $\sim 3 \text{ \AA}$ ) as schematically shown in Figure 4.1(b). This requires the localization strength much stronger than that of the typical WS states in the artificial quantum-well composed of bulk semiconductors showing nanometer-scale localization ( $\gg 1 \text{ nm}$ )[42]. The atomic-scale confinement can be achieved in 3R structure through additional localization mechanism driven by the crystallographic symmetry besides the WS mechanism. In followings, we analyze the irreducible representation (IR) of double group to elucidate the localization mechanism from the symmetry argument under the presence of the SOC.

The wavefunctions at  $K$  valley of commensurately stacked  $N$  layers,  $\Psi_K$ , can be described by the linear combination

$$\Psi_K = \sum_{n=1}^N \sum_{i=\pm} c_{n,i} |n, l\rangle \otimes \chi_i, \quad (1)$$

where  $|n, l\rangle$  and  $\chi_i$  are the Bloch wavefunction localized in the  $n$ -th layer (one drawn in Figure 4.1(b)) and the spin state ( $S_z \chi_{\pm} = \pm \hbar / 2 \chi_{\pm}$ ), respectively.

The spatial and spin parts can be chosen as eigenstates of the  $C_3^+$  symmetry which persists in the group of wave vector (GWV) of  $K$  in any commensurate structure:

$$C_3^+ |n, l\rangle = e^{-i\frac{2\pi}{3}l} |n, l\rangle, \quad C_3^+ \chi_{\pm} = e^{\mp i\frac{\pi}{3}} \chi_{\pm}. \quad (2)$$

The eigenvalue of the spatial part is defined with respect to a  $C_3^+$  axis through the A site at origin among three inequivalent axes through A, B and C sites in Figure 4.1(a). This definition is mandatory because the IR of a point group (isomorphic to the GWV) requires the action of symmetries passing through the single point. Thus, there is a subtle difference from the previous definition using three inequivalent axes[18, 19, 43]. The eigenvalue in this work is associated with the IR and hence the CAM with conserved quantum number  $l$  having one of the three values:  $-1$ ,  $0$ , or  $+1$ . The major components of Bloch wavefunctions for the valence band (VB) and the conduction band (CB) states are Mo  $4d_{x^2-y^2} \pm i4d_{xy}$  and  $4d_{z^2}$  orbitals, respectively[3]. Table 4.2 shows CAM for both bands depending on the configuration of layer (See Supplementary Note II for the calculation details). On the other hand, the eigenvalue of the spin parts is given by the transformation property of the spinor under special unitary group  $SU(2)$ [44]. Considering the contributions of the CAM and the spinor, the (reducible) representation  $\Gamma$  of double group is constructed on the space spanned by the VB or the CB basis states in any stacking. Then, the  $K$  valley states in the symmetry-adapted form and corresponding IR are determined by the decomposition of  $\Gamma$ .

Table 4.2 Stacking-dependent crystal angular momentum (CAM) of the Bloch wavefunctions  $|n, l\rangle$  at the  $K$  valley.

Configuration of the layer	<b>A</b>	<b>B</b>	<b>C</b>	$\bar{\mathbf{A}}$	$\bar{\mathbf{B}}$	$\bar{\mathbf{C}}$
CB	0	-1	1	0	-1	1
VB	-1	1	0	1	0	-1

At  $-K$  valley, the sign of CAM is reversed by the time-reversal symmetry.

We compare the bilayer structure of the 3R (**BC** stacking) with the 2H ( **$\bar{B}C$**  stacking) to illustrate the essence of the localization mechanism. This analysis can be extended to arbitrary stacking. Table 4.3 shows the symmetry-adapted form of  $K$  valley states and associated IR label (See Supplementary Note III for the calculation details). A simple rule governing the confinement is that the states spanning the different IRs cannot be superposed whereas the states spanning the same IR can be superposed. In the 3R structure, every IR of the Abelian  $C_3^\dagger$  (double group of  $C_3$ ) is one-dimensional, excluding the degeneracy. It is noted that the states of the parallel spins always span the different IRs indicating the prohibited superposition between them. Thus, these states are confined solely by symmetry. This aspect for parallel spin is in line with the previous single group formalism neglecting spin[18, 19] (i.e., all the  $K$  valley states would span the different IRs of  $C_3$  solely by the CAM contribution). By contrast, the particular pairs of states with the opposite spins, e.g.,  $v1$  ( $\Gamma_4$ ) and  $v4$  ( $\Gamma_4$ ), and  $c2$  ( $\Gamma_6$ ) and  $c3$  ( $\Gamma_6$ ), span the same IR allowing the simultaneous delocalization and spin-depolarization. In this case, symmetry does not guarantee the confinement and there must be a source of energy splitting between the adjacent spins to inhibit the superposition. We note that the spontaneous electric polarization in 3R provides the sizable interlayer potential between them, which provide the necessary energy splitting. Thus, WS states showing the atomic-scale confinement with definite spin will manifest itself.

Table 4.3 Symmetry-adapted form of the  $K$  valley states and corresponding irreducible representation (IR) of the double group for the bilayer 3R and 2H structure.

Band		3R ( $D_3^\dagger$ )		2H ( $D_3^\dagger$ )	
		Symmetry-adapted form	IR	Symmetry-adapted form	IR
CB	$c4$	$ 2,1\rangle \otimes \chi_-$	$\Gamma_4$	$ 1,-1\rangle \otimes \chi_- -  2,1\rangle \otimes \chi_+$	$\Gamma'_5$
	$c3$	$ 2,1\rangle \otimes \chi_+$	$\Gamma_6$	$ 1,-1\rangle \otimes \chi_- +  2,1\rangle \otimes \chi_+$	$\Gamma'_6$
	$c2$	$ 1,-1\rangle \otimes \chi_-$	$\Gamma_6$	$\{ 1,-1\rangle \otimes \chi_+,$ $- 2,1\rangle \otimes \chi_-\}$	$\Gamma'_4$
	$c1$	$ 1,-1\rangle \otimes \chi_+$	$\Gamma_5$		
VB	$v4$	$ 2,0\rangle \otimes \chi_+$	$\Gamma_4$	$\{(\cos \alpha  1,0\rangle - \sin \alpha  2,0\rangle) \otimes \chi_+,$ $(\sin \alpha  1,0\rangle - \cos \alpha  2,0\rangle) \otimes \chi_-\}$	$\Gamma'_4$
	$v3$	$ 1,1\rangle \otimes \chi_+$	$\Gamma_6$		
	$v2$	$ 2,0\rangle \otimes \chi_-$	$\Gamma_5$	$\{(\sin \alpha  1,0\rangle + \cos \alpha  2,0\rangle) \otimes \chi_+,$ $(\cos \alpha  1,0\rangle + \sin \alpha  2,0\rangle) \otimes \chi_-\}$	$\Gamma'_4$
	$v1$	$ 1,1\rangle \otimes \chi_-$	$\Gamma_4$		

The stacking sequences are **BC** (3R) and  $\bar{\mathbf{B}}\mathbf{C}$  (2H). The band index corresponds to Figure 4.2. We adopt the notation of IR from the literature[44] and add the prime ( $\Gamma'$ ) for  $D_3^\dagger$ . The valley states at  $-K$  is obtained by time-reversal symmetry.

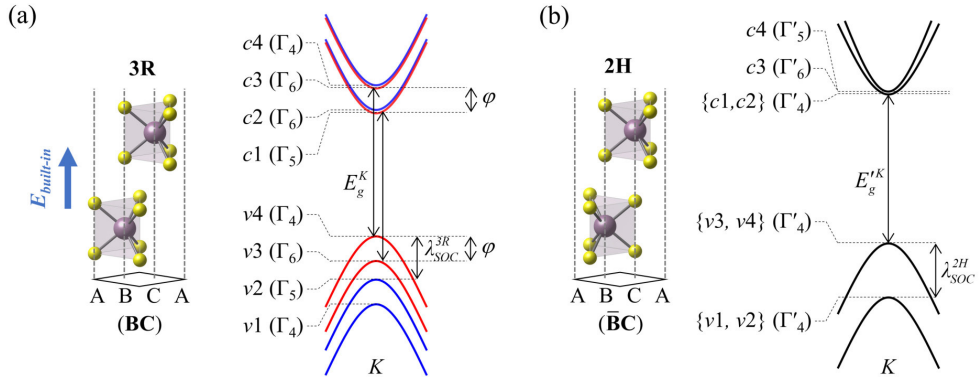


Figure 4.2 Schematic band structures with the double group representation  $\Gamma$  of bilayer structure. The red and blue lines indicate spin up and down, respectively. (a) In 3R, all the states are nondegenerate from  $C_3^\dagger$  symmetry and show WS type localization under  $E_{built-in}$  with splitting energy  $\varphi$ . Except for certain pair of opposite spins,  $\Gamma$  differ between adjacent states indicating prohibited superposition from symmetry. (b) In 2H, degeneracy arises from  $D_3^\dagger$  symmetry whose IR labels are marked with the prime ( $\Gamma'$ ). See Table 4.3 for the detailed wavefunction forms.

In 2H structure, on the contrary, the  $K$  valley states are spread over the two layers reflecting the non-polar symmetry  $D_3^\dagger$ . The details of the distribution depend on the dimensionalities of the IR (IR label of  $D_3^\dagger$  is expressed with the prime such as  $\Gamma'$ ). While the non-degenerate states ( $\Gamma_5, \Gamma_6$ ) are symmetrically delocalized over the two layers with zero spin polarization, the two degenerate states ( $\Gamma_4$ ) have a definite spin and are distributed over the two layers depending on their spin states. In particular, the degenerate VB states show the spin-dependent asymmetric localization, where the  $\alpha$  of trigonometric factors determines the localization strength. We note that those states correspond to the spin-polarized gauge[45] and reproduce the spin-layer locking effect[6, 46].

Figure 4.2 shows the schematics of  $K$  valley of the 3R and 2H structures considering the interlayer potential and the SOC splitting. In Figure 4.2(a), the band energy of a given spin state increases with the layer-index by the  $\varphi$  under the built-in field. Each of the electrons confined in the individual layer stacked along the polar axis is hence distinguished by the potential energy. The 3R stacks with more than two layers show the same characteristic (Figure 4.1(b)). This is an importantly distinct characteristic of the polar 3R structure compared to the non-polar 2H structure shown in Figure 4.2(b) where the layer-index is independent of the energy. The predicted band structures are in good agreement with those calculated by DFT (which will be shown in detail for 3R in Figure 4.4(a) and for 2H in Figure 4.5(a), respectively).

Double group analysis indicates that the confinement of carriers in 3R structure can be canceled out by modulating the interlayer potential. The compatibility relations in Figure 4.3(a) and (b) show the evolution of  $K$  valley states under the external electric field along the  $z$ -axis for 3R and 2H structures, respectively. The symmetry of the 3R is preserved  $C_3^\dagger$  as while that of the 2H is reduced from  $D_3^\dagger$  to  $C_3^\dagger$  under the field. In the 3R ( $E_{built-in}$  is upward in **BC** stacking), the energies of the  $v1$  and  $v4$  ( $\Gamma_4$ ), and  $c2$  and  $c3$  ( $\Gamma_6$ ) become closer under the field along the  $-z$  direction as shown in Figure 4.3(a). At some critical point, those states spanning the same IR are strongly mixed through anti-crossing, which results in the delocalization and spin-depolarization. Note that the anti-crossing does not take place under the field along the  $+z$  direction which is parallel with the built-in field. In the 2H structure, in contrast, the degenerate VB and CB states are split,  $\Gamma'_4 \rightarrow \Gamma_4$  (spin up) +  $\Gamma_5$  (spin down) for VB, by the symmetry breaking, which may result in the localization. The split VB states of the same spin, however, span the same IR of  $C_3^\dagger$  as shown in Figure 4.3(b). Those states can be delocalized by the mixing through the anti-crossing at the critical point.

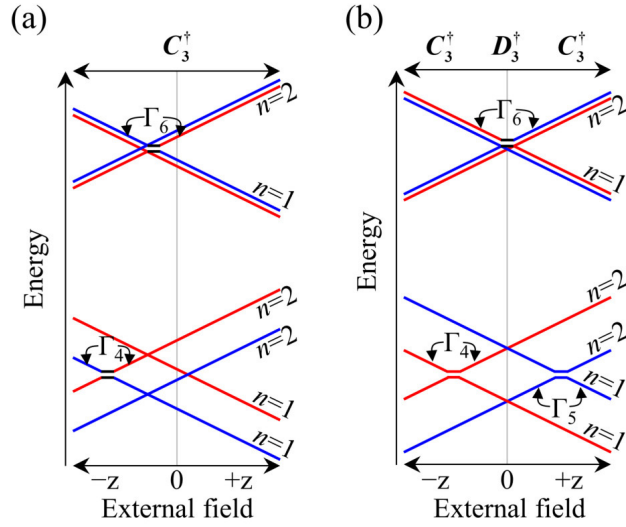


Figure 4.3 Compatibility relation for the  $K$  valley states under the electric field along the  $z$ -axis. The red and blue lines indicate spin up and down, respectively. (a) 3R structure undergoes the anti-crossing accompanied by the delocalization and spin-depolarization at the critical field. The critical field is always opposite to the built-in electric field ( $-z$  direction in the **BC** stacking). (b) In 2H structure, the anti-crossing between split VB states with the up (down) spin appears at the critical field along  $-$  ( $+$ ) $z$  direction entailing the delocalization but no spin-depolarization.

The band structures obtained by the DFT calculations verify the behaviors depicted by the double group analysis. Figure 4.4(a) shows the pristine band structure and  $K$  valley states of 3R structure from LDA calculation. The energy splittings between the parallel spins for both the VB ( $v1$  and  $v2$ , and  $v3$  and  $v4$ ; 94 meV) and the CB ( $c1$  and  $c3$ ,  $c2$  and  $c4$ ; 77 meV) are consistent with the interlayer potential  $\varphi$  in the bilayer structure (85 meV). The small deviation from the  $\varphi$  is attributed to the slight difference in the intralayer band gap  $E_g^K$  of the two layers, such as 1.778 eV for the upper layer ( $v4 \leftrightarrow c3$ ) and 1.795 eV for the lower layer ( $v3 \leftrightarrow c1$ ). The strong SOC splitting at the VB ( $\lambda_{SOC}^{3R} = 145$  meV) and the negligible SOC splitting at the CB (2 meV) are similar to those of free-standing monolayer. The band structures under the electric field  $E_{ext}$  show the significant anti-crossing for the CB states at the critical field strength of  $\sim 10$  MVcm $^{-1}$  (Figure 4.4(b)) while those of the VB states at  $\sim 30$  MVcm $^{-1}$  (Figure 4.4(c)). The high critical field for the VB states can be understood by its large Zeeman splitting  $\lambda_{SOC}^{3R}$  which is negligible at the CB states. A similar calculation using PBE-D3 results in the lower critical field (e.g.,  $\sim 5$  MVcm $^{-1}$  for the CB and  $\sim 22$  MVcm $^{-1}$  for the VB states), which is understood from its lower interlayer potential ( $\varphi \sim 59$ meV).

The 2H structure has a similar direct gap ( $E_g^K = 1.791$  eV) and a larger SOC splitting at the VB ( $\lambda_{SOC}^{2H} = 185$  meV) compared to the 3R structure. This larger

splitting was experimentally observed[47] and is attributed to the anti-bonding characteristics of the  $\{v3, v4\}$  states and bonding characteristics of the  $\{v1, v2\}$  state, respectively. Interestingly, the LDA calculations show that the spin up VB states become more delocalized under the field along the  $-z$  direction up to the field strength  $\sim 15 \text{ MVcm}^{-1}$  where the distribution is almost symmetric over two layers (Figure 4.5). Likewise, the spin down VB states undergo delocalization under the field along the  $z$  direction. Therefore, the 2H stacking cannot induce the atomically confined valley states like 3R stacking, although it acquires the same polar symmetry under external bias. The results highlight the crucial role of both crystallographic symmetry and (internal and external) electric field in the localization mechanism.

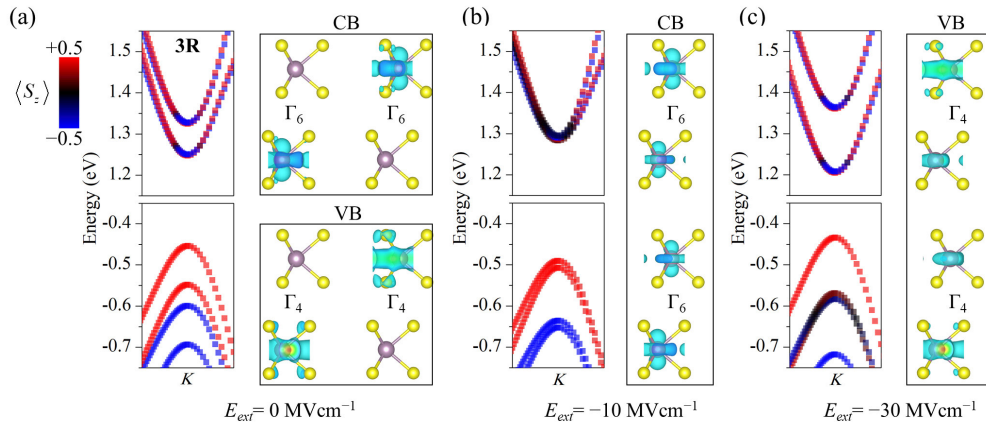


Figure 4.4 LDA band structures of pristine (a) and biased (b, c) 3R MoS<sub>2</sub>. (a) All the bands are spin polarized and confined, including the states spanning the same IR. (b) Under the field strength of 10 MVcm<sup>-1</sup>, the anti-crossing induces mixing of two CB states having identical representation  $\Gamma_6$ , which results in the significant delocalization and depolarization of spin. (c) The anti-crossing between VB states of  $\Gamma_4$  takes place at higher field of 30 MVcm<sup>-1</sup>. The direction of external field is downward.

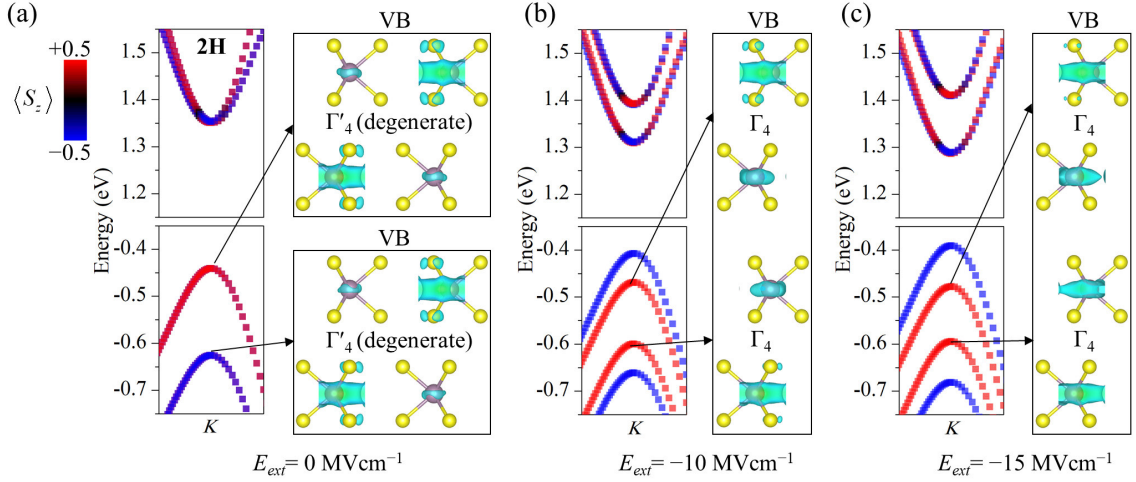


Figure 4.5 LDA band structures of pristine (a) and biased (b, c) 2H MoS<sub>2</sub> ( $\overline{\text{BC}}$  stacking). The IR labels of  $D_3^\dagger$  are marked with the prime ( $\Gamma'$ ) in (a), on the contrary, those of  $C_3^\dagger$  are marked without the prime ( $\Gamma$ ) in (b, c) by breaking the  $D_3^\dagger$  symmetry. (a) In the absence of field, all the bands are spin-depolarized although pair of degenerate states have definite spin. The VB states are slightly delocalized. (b, c) Under the field along with the  $-z$  direction, delocalization of up spin bands becomes significant by the anti-crossing between spin up states ( $\Gamma_4$ ). By increasing the field strength from (b) 10 MVcm<sup>-1</sup> to (c) 15 MVcm<sup>-1</sup>, the probability distribution over two layers becomes almost symmetric.

### 4.3.3 Optical selection rule for interlayer dynamics

Selection rule governing carrier dynamics in the layered structure is the primary mean to control the layer-index of carriers. Direct product of IRs for spin-conserving selection rule is reduced to the conservation of CAM,  $\Delta l = l^{final} - l^{initial} \equiv l_{photon}$  modulo 3 the  $C_3^+$  symmetry. The polarization states of the light are indicated as  $\sigma^\pm$  ( $=1/\sqrt{2}(\hat{\mathbf{x}} \pm \hat{\mathbf{y}})$ ;  $l_{photon} = \pm 1$ ) for an out-of-plane incidence and  $\pi$  ( $=\hat{\mathbf{z}}$ ;  $l_{photon} = 0$ ) for an in-plane incidence, respectively. Figure 4.6(a) shows frequency and polarization selection rule at  $K$  valley of the bilayer 3R structure with **BC** stacking. We classify the transitions as  $\Sigma$  (across the band gap in the visible range) and  $\Phi$  (interlayer charge transfer in the infrared range) types with the superscript corresponding to the change of layer-index  $\Delta n$ . Previous symmetry analyses addressed the stacking-dependent selection rule especially for the  $\Sigma$  transitions in heterostructures[48, 49], but whether the  $\Phi$  transition is subject to the definite polarization selection rule was ambiguous.

An essential feature of the 3R structure is that the  $\Phi$  transitions of both holes and electrons are subject to identical frequency ( $\hbar\omega_2 = \varphi$ ) and polarization ( $\sigma^-$ ) selection rule. This is because the band-offset is originated from the interlayer potential  $\varphi$  between the two layers connected by the rhombohedral translational symmetry  $R$  inherited from the periodic bulk 3R homostructure (Figure 4.1(a)). In all the other commensurate stackings of homo and

heterostructures,  $\Phi$  transitions of holes and electrons require a different light source (Figure 4.7). For instance, in the 2H heterostructure, the  $\Phi$  transition of the hole requires irradiation of the  $\pi$  polarization which is different from the  $\sigma^-$  needed by the electron. Therefore, the  $\Phi$  transition in the 2H heterostructure requires the more complicated optical inputs compared to the 3R homostructure. We note that the polarization selection rule of the 3R structure was misinterpreted as the same with that of 2H structure in previous study using time-dependent DFT coupled with molecular dynamics (TDDFT-MD)[50, 51].

The observations provide a simple route to the optical control of the layer-index with the dual-frequency light source in the 3R structure as shown in Figure 4.6(b). The key suggestion is to utilize the  $\Phi$  transition as an active excitation channel, which has been considered merely as a non-radiative energy relaxation channel after the optical pumping[7–17]. The 3R structure enables the binary operations with the frequencies of  $\hbar\omega_1 = E_g^K - \varphi$  (visible regime, indicated by orange) and  $\hbar\omega_2 = \varphi$  (infrared regime, indicated by red) utilizing either the  $\Sigma^-$  transition for  $\Delta n = -1$ , or the successive  $\Sigma^-$  and  $\Phi^+$  transitions for  $\Delta n = +1$  as illustrated in Figure 4.6(b). The motion of carriers during the  $\Delta n = +1$  operation is that the electron (hole) at the lower (upper) layer created by the  $\Sigma^-$  transition moves upward (downward) by the  $\Phi^+$  transition which is an excited-state absorption[52]. Note that the light helicities for the  $\hbar\omega_1$  and the  $\hbar\omega_2$  should be always the same as  $\sigma^\mp$  for the

$\Delta n = +1$  operation on the  $\pm K$  valley. For instance, illumination of  $\hbar\omega_2$  with  $\sigma^-$  polarization after  $\hbar\omega_1$  with  $\sigma^+$  polarization shall not induce  $\Phi^+$  transition since there are no electrons (holes) at the CB (VB) at the  $K$  valley (Pauli blocking). The valley-polarization is selective because, for instance, the  $\sigma^-$  polarized  $\hbar\omega_1$  light for the  $\Sigma^-$  transition at the  $K$  valley cannot induce the  $\Sigma^0$  transition at the  $-K$  valley, coupled with the same  $\sigma^-$  polarization, in resonance with the  $\hbar(\omega_1 + \omega_2)$ . Combined with the valley-index which is controlled by the light polarization,  $2 \otimes 2$  states can be prepared as  $\{00, 01, 10, 11\}$  where the first and second bit represents a distinct electric- and valley-polarization states, respectively. The information of the layer- and valley-polarization may be read out capacitively[53] and by the valley Hall effect[54], respectively. Although challenging, it will be interesting to detect the electron/hole current at each layer by suitable electrode geometry.

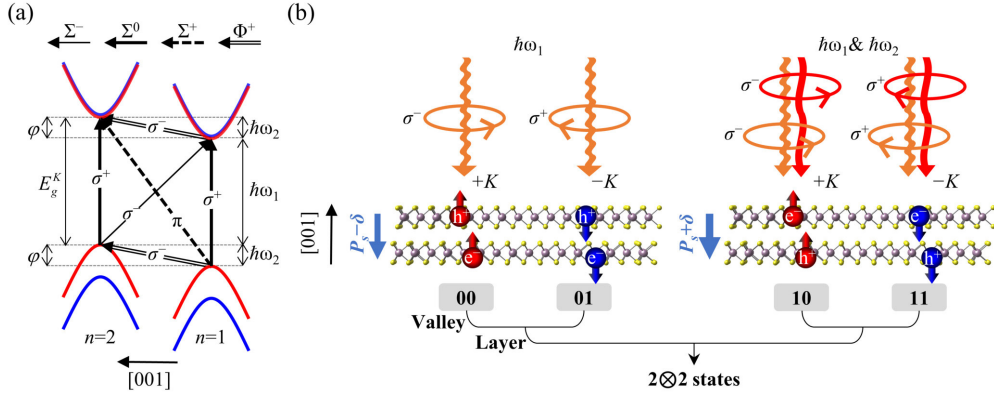


Figure 4.6 (a) Frequency and polarization of the optical selection rule at K valley of bilayer 3R structure. In the 3R homostructure, the  $\Phi^+$  transition of electrons and holes can be induced simultaneously by a single light source. At  $-K$  valley, the light polarization is reversed. (b) The  $\Delta n = -1$  operation by the illumination of photon of energy  $\hbar\omega_1 = E_g^K - \varphi$  (orange) coupled with the  $\Sigma^-$  transition. Simultaneous incidence with the  $\hbar\omega_2 = \varphi$  (red) triggers the  $\Phi^+$  transition by virtue of the excited-state absorption, corresponding to the  $\Delta n = +1$  operation. The magnitude of  $P_s$  is modulated in accord with the configuration of electron-hole carriers. The valley-index can be independently controlled by the helicity for each frequency and constitutes the  $2\otimes 2$  quantum states in total with the layer-index.

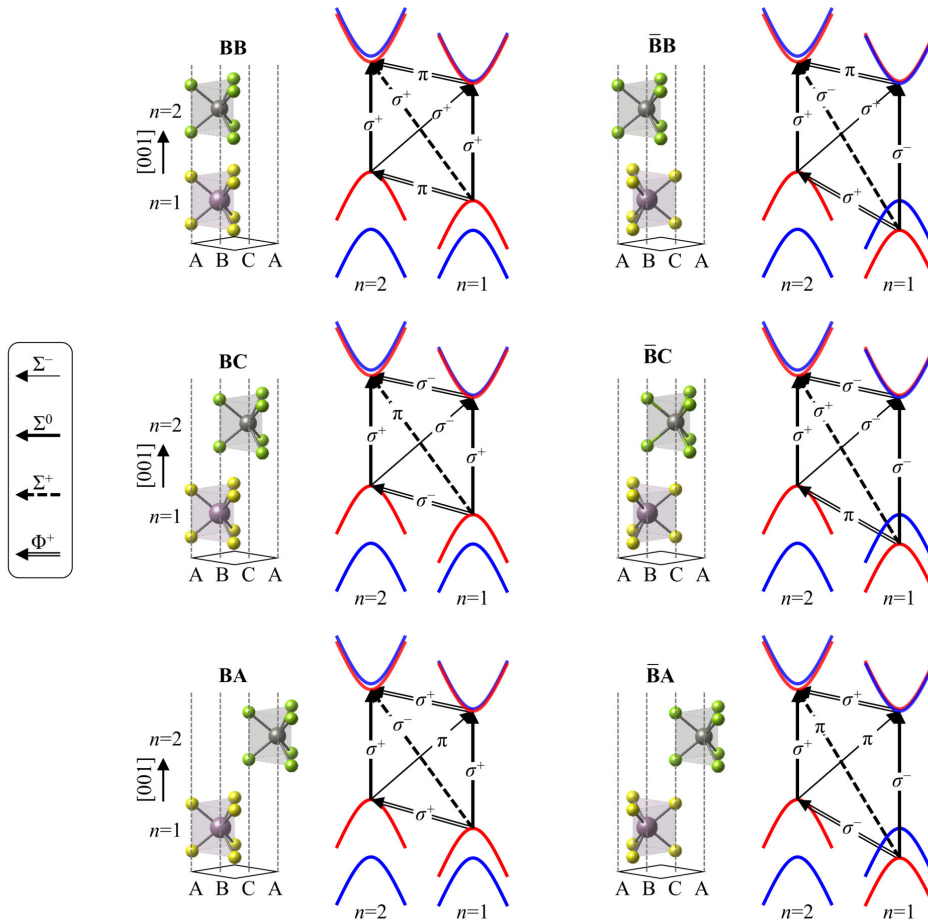


Figure 4.7 Optical selection rule of various commensurate heterostructures. Bilayer heterostructures  $\text{MX}_2/\text{M}'\text{X}'_2$  and the schematics of the  $K$  valleys drawn in the real space along the  $[001]$  axis. Optical transitions are classified into  $\Sigma$  (across the band gap in the visible range) and  $\Phi$  (interlayer charge transfer in the infrared range) types with the superscript corresponding to the change of layer-index  $\Delta n$ . Frequency selection rule can be varied with the details of the energy spectra such as band offsets and Zeeman spin splitting depending on the chemistry; e.g.,  $\text{M} = \{\text{Mo}, \text{W}\}$  and  $\text{X} = \{\text{S}, \text{Se}, \text{Te}\}$ . The polarization selection rule is independent of the chemistry. At the  $-K$  valley, the light helicity is reversed

In principle, one can also consider the  $\Sigma^+$  transition for the  $\Delta n = +1$  operation. This route, however, has considerable disadvantages. First, it requires an in-plane incidence of light ( $\pi$  polarization), making the device geometry more complex, and the valley-index is not controllable because the  $K$  and the  $-K$  valleys absorb the light simultaneously. In addition, an unintentional absorption at the off- $K$  valleys will be included due to its high photon energy. The structures other than 3R homostructure have similar problem.

The lifetime of the interlayer excitons may determine the retention of information encoded in the layer-index. The non-adiabatic  $\Phi$  transition will be the dominant energy relaxation channel since the radiative recombination lifetime of the interlayer exciton (from 2 ns[8] to 100 ns[14]) is quite long. In particular, only the 10 and 11 states are subject to the relaxation because the electron-hole configurations in the 00 and 01 states are stable under the built-in potential. Therefore, exploiting optical  $\Phi^+$  transition has an indispensable benefit, compared to the  $\Sigma^+$  transition, that the 10 and 11 states can be retained (re-written) by illuminating the infrared pulse of the  $\hbar\omega_2$  overwhelming the relaxation. To authors' knowledge, data for the rate of non-adiabatic  $\Phi$  transition in 3R homostructure has yet been reported. For heterostructure, the relaxation rate measured from the transient spectroscopy experiment is very fast (within  $\sim 50$  fs) regardless of stacking geometry[7, 11]. The feasibility of such a stacking-independent ultrafast relaxation against large momentum mismatch in the incommensurate structure is under debate[55]. Meanwhile,

TDDFT-MD simulations showed that the rate in the 3R structure ( $\sim 1500$  fs[51]) is one order of magnitude slower than that in the 2H ( $\sim 100$  fs[50]-150 fs[51]) MoS<sub>2</sub>/WS<sub>2</sub> heterostructure. Further study on interlayer dynamics considering stacking effect is required to accurately estimate the retention time.

#### 4.4 Conclusion

We investigated the fundamental consequences of the symmetry of layered two-dimensional (2D) polar crystal concerning the controllability of the positional degree of freedom called layer-index. The polar 3R homostructure hosts the Wannier-Stark (WS) states with extreme confinement at the  $K$  valleys from the novel spontaneous electric polarization and the double group symmetry. In this way, each carrier encodes the layer information precisely and is distinguished by the potential energy along the polar axis. Optical processing of the layer-index is hence based on the conservation of energy, which has an interesting analogy with the control of the valley-index through the conservation of the crystal angular momentum (CAM) in the non-centrosymmetric crystal. The key feature is to utilize optical interlayer charge transfer in the infrared regime as an additional excitation channel which makes the interlayer motion reversible. The selection rule in the 3R homostructure enabling the binary operation through the minimal optical

input is much simpler than those in other types of homo and heterostructures. The explicit instruction on the  $2 \times 2$  states/cell device operated by a dual-frequency polarized light source in the polar 3R MoS<sub>2</sub> may constitute the first attempt to harness the layer-index as an information carrier based on the 2D homostructure. The integration of the layer-index into the valleytronics doubles information density, and further possibilities remain to be explored.

## 4.5 Appendix

### 4.5.1 Berry phase Calculation

In modern theory of polarization[56], the electric polarization of given state parametrized by  $\lambda$  is given as the difference respect to the reference state  $\Delta P = P^\lambda - P^0$ . In the periodic gauge for crystalline structure, the electronic term in  $P^\lambda$  is given[27]

$$P_\alpha^{\lambda(el)} = \frac{-2ie}{(2\pi)^3} \sum_{n=1}^{occ} \int_{\text{BZ}} d\mathbf{k} \left\langle u_{n\mathbf{k}}^\lambda \left| \frac{\partial}{\partial k_\alpha} \right| u_{n\mathbf{k}}^\lambda \right\rangle, \quad (\text{S1})$$

where  $\alpha$  is the Cartesian direction,  $u_{n\mathbf{k}}^\lambda$  is the cell-periodic part of the Bloch wavefunction, and Brillouin zone (BZ) integral is related to the Berry phase of  $n$ -th band. In popular plane wave based DFT codes, the finite-difference version of the Equation (S1) is implemented[56]. Note that the z-component

of the polarization  $P_z^{\lambda(el)}$  is associated with the differential phase of Bloch wavefunctions varying with the wavevector  $\mathbf{k}$  along the z-axis in BZ. The finite layers of MoS<sub>2</sub>, however, are strictly two-dimensional (2D) crystal which lacks translational symmetry along the z-axis and wavevector  $\mathbf{k}$  along the z-axis is not defined correspondingly. Even when simulated with supercell consisting of the MoS<sub>2</sub> slab and the vacuum layers, the  $\mathbf{k}$  points out of the 2D BZ carries no physical meaning (and hence, the differential phase  $\partial u_{n\mathbf{k}}^\lambda / \partial k_z$ ). Since the 2D crystal does not provide closed-path along the z-axis in parameter space of BZ on which the Berry (Zak) phase[27] is defined, it might be meaningless to use Equation (S1) for the calculation of z-component of  $P_s$  of finitely stacked 2D MoS<sub>2</sub>. In fact, the  $P_s$  calculated with the slab-vacuum structure is negligibly small, even it obviously shows the built-in potential implying the existence of the spontaneous polarization (Figure 4.8).

Accordingly, we rather construct the supercell consisting of the finite layers of 3R MoS<sub>2</sub> intercalated between non-polar stacking as shown in Figure 4.9 in order to properly estimate the  $P_s$ . In the bulk sandwich structure, the translational symmetry along the z-axis is recovered where the Equation (S1) is applicable. The calculated  $P_s$  is the sum of the contribution from the polar and non-polar sections based on the fact that the Equation (S1) is equivalent to the Wannier function-based formalism where the total polarization is the sum of the contribution from the individual Wannier functions localized in each atom in real space[27,56]. It is assumed that the contribution from the

non-polar section is zero. Indeed, the finite layers of 3R MoS<sub>2</sub> in the supercell structure shows the finite  $P_s$ , which increases with the thickness and saturates to the bulk value (Figure 4.1(c)).

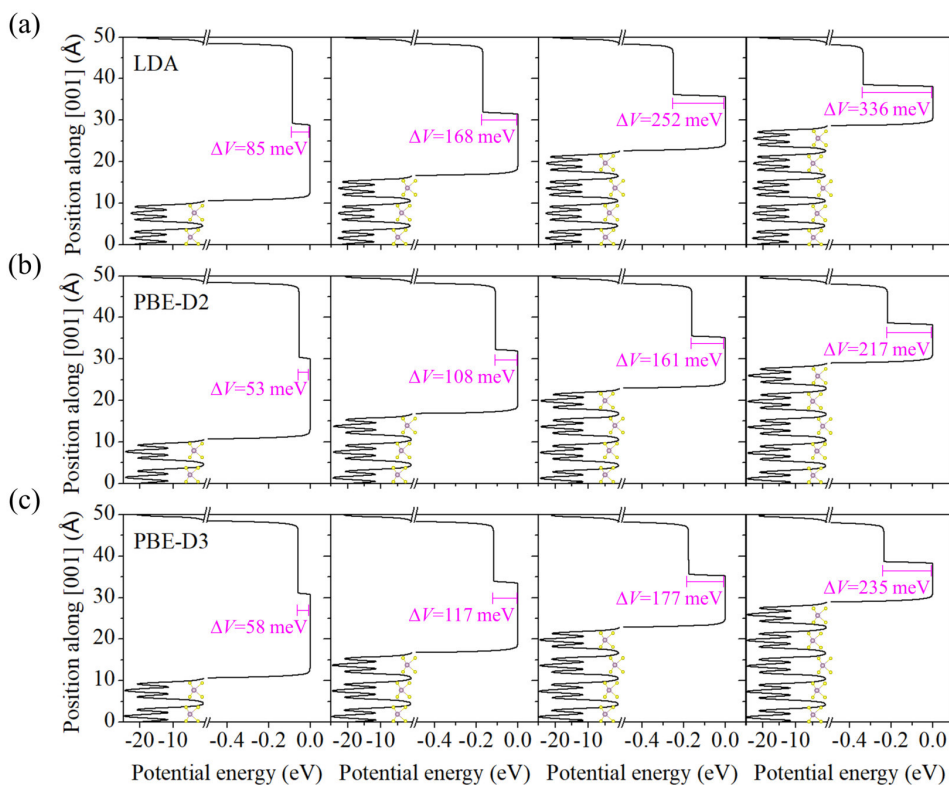


Figure 4.8 Built-in potential developed by the spontaneous polarization of the finite layers of 3R MoS<sub>2</sub>. Plane-averaged electrostatic potential profiles along the [001] axis of 2-5 layers of 3R MoS<sub>2</sub> (**BCA**··· stacking) calculated using vacuum-slab structures with (a) LDA, (b) PBE-D2 and (c) PBE-D3 functionals.  $\Delta V$  is the potential difference between the top and bottom layers.

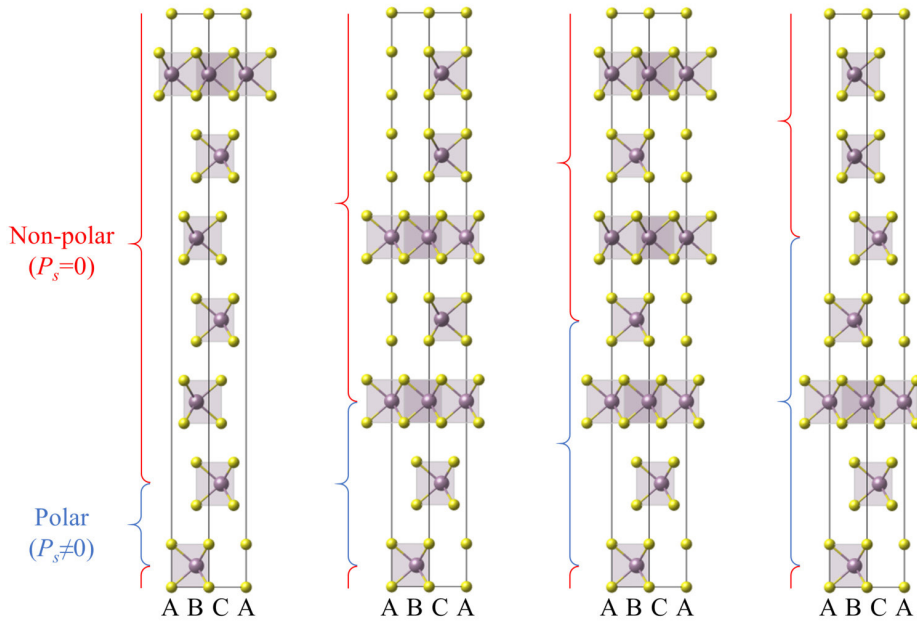


Figure 4.9 Finite layers of 3R stacking sandwiched in supercell structure. Finite layers (2-5 layers) of MoS<sub>2</sub> with polar 3R stacking are intercalated between non-polar stacking (including 2H). In-plane lattice parameters, layer thickness and interlayer distances in the supercell structures are the same with those of bulk 3R MoS<sub>2</sub>.

#### 4.5.2 Calculation of crystal angular momentum

The crystal angular momentum (CAM) is a quantum number conserved under discrete rotational symmetry. This is based on the fact that the CAM designates irreducible representation (IR) of the point group. The point group representation corresponds to the action of symmetries passing through the origin. Therefore, the eigenvalues of 3-fold symmetry axis passing through the origin, among three axes, correspond to the CAM (Figure 4.10). The  $K$  valley states localized at the layer of configuration  $\mathbf{A}$  can be written as

$$\psi_{\mathbf{K}}^{\mathbf{A}}(\mathbf{x}) = \sum_j e^{i\mathbf{K} \cdot \mathbf{R}_j} \phi(\mathbf{x} - \mathbf{R}_j), \quad (\text{S2})$$

where  $\phi(\mathbf{x})$  is Mo 4d orbital centered at  $\mathbf{t}_A$  (figure S3), and  $\mathbf{K} = 1/3(\mathbf{b}_1 + \mathbf{b}_2)$  with reciprocal lattice vectors  $\mathbf{b}_1$  and  $\mathbf{b}_2$  defined by lattice  $\mathbf{R}_j$ . The  $\phi(\mathbf{x})$  having the angular part  $Y_2^{m_l}$  ( $Y_2^2$  and  $Y_2^0$  for VB and CB, respectively[3]) transforms under the 3-fold symmetry  $\{C_3^+|0\}$  (Seitz notation) as  $\overline{\{C_3^+|0\}}\phi(\mathbf{x}) = e^{-i2\pi m_l/3}\phi(\mathbf{x})$  in the active convention.

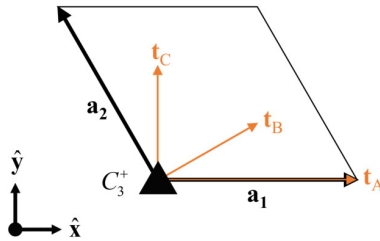


Figure 4.10 In the commensurate structure, position of the Mo and S atoms projected onto the 2D hexagonal primitive cell corresponds to the partial translation vectors  $\mathbf{t}_A = \mathbf{a}_1$ ,  $\mathbf{t}_B = 2/3\mathbf{a}_1 + 1/3\mathbf{a}_2$  and  $\mathbf{t}_C = 1/3\mathbf{a}_1 + 2/3\mathbf{a}_2$ , respectively. The  $C_3^+$  symmetry axes at  $\mathbf{t}_A$ ,  $\mathbf{t}_B$  and  $\mathbf{t}_C$  are all preserved in any commensurate stacking. The CAM is the eigenvalue of the  $C_3^+$  symmetry axis at  $\mathbf{t}_A$ .

The CAM of the  $\psi_K^A(\mathbf{x})$  is given

$$\overline{\{C_3^+|0\}}\psi_K^A(\mathbf{x}) = \sum_j e^{i\mathbf{K}\cdot\mathbf{R}_j} \overline{\{C_3^+|0\}}\phi(\mathbf{x}-\mathbf{R}_j). \quad (\text{S3})$$

Considering the commutation relation of the space-group operators acting on functions,

$$\begin{aligned} \overline{\{C_3^+|0\}}\phi(\mathbf{x}-\mathbf{R}_j) &= \overline{\{C_3^+|0\}}\overline{\{E|\mathbf{R}_j\}}\phi(\mathbf{x}), \\ &= \overline{\{E|C_3^+\mathbf{R}_j\}}\overline{\{C_3^+|0\}}\phi(\mathbf{x}), \end{aligned} \quad (\text{S4})$$

equation (S3) is reduced to

$$\begin{aligned} \sum_j e^{i\mathbf{K}\cdot\mathbf{R}_j} \overline{\{E|C_3^+\mathbf{R}_j\}}\overline{\{C_3^+|0\}}\phi(\mathbf{x}) &= e^{-i2\pi m_l/3} \sum_j e^{i\mathbf{K}\cdot\mathbf{R}_j} \phi(\mathbf{x}-C_3^+\mathbf{R}_j), \\ &= e^{-i2\pi m_l/3} \sum_j e^{i(C_3^+\mathbf{K})\cdot(C_3^+\mathbf{R}_j)} \phi(\mathbf{x}-C_3^+\mathbf{R}_j), \\ &= e^{-i2\pi m_l/3} \psi_K^A(\mathbf{x}), \end{aligned} \quad (\text{S5})$$

where the CAM of  $\psi_K^A(\mathbf{x})$  is the same as the  $m_l$  modulo 3.

The  $K$  valley states at the layers of configurations **B** and **C** are simply translation of  $\psi_K^A(\mathbf{x})$  by  $\mathbf{t}_B$  and  $\mathbf{t}_C$ , respectively. We define the  $\psi_K^m(\mathbf{x})$  for  $m = \mathbf{B}$  and **C** as

$$\psi_K^m(\mathbf{x}) = \overline{\{E|\mathbf{t}_m\}}\psi_K^A(\mathbf{x}). \quad (\text{S6})$$

The CAM of  $\psi_K^m(\mathbf{x})$  is given, considering the commutation relation in Equation (S4),

$$\begin{aligned} \overline{\{C_3^+|0\}}\psi_K^m(\mathbf{x}) &= \overline{\{C_3^+|0\}}\overline{\{E|\mathbf{t}_m\}}\psi_K^A(\mathbf{x}), \\ &= \overline{\{E|C_3^+\mathbf{t}_m\}}\overline{\{C_3^+|0\}}\psi_K^A(\mathbf{x}), \\ &= e^{-i2\pi m/3}\overline{\{E|C_3^+\mathbf{t}_m\}}\psi_K^A(\mathbf{x}). \end{aligned} \quad (\text{S7})$$

It is noted that  $C_3^+\mathbf{t}_m = \mathbf{t}_m - \mathbf{R}_j$  where

$$\begin{aligned} C_3^+\mathbf{t}_B &= \mathbf{t}_B - \mathbf{a}_1, \\ C_3^+\mathbf{t}_C &= \mathbf{t}_C - (\mathbf{a}_1 + \mathbf{a}_2). \end{aligned} \quad (\text{S8})$$

By the Bloch theorem,  $\overline{\{E|C_3^+\mathbf{t}_B\}}\psi_K^A(\mathbf{x}) = e^{i\mathbf{K}\cdot\mathbf{a}_1}\psi_K^B(\mathbf{x})$ ,  $\overline{\{E|C_3^+\mathbf{t}_C\}}\psi_K^A(\mathbf{x}) = e^{i\mathbf{K}\cdot(\mathbf{a}_1+\mathbf{a}_2)}\psi_K^C(\mathbf{x})$ , Equation (S7) is reduced to

$$\begin{aligned} \overline{\{C_3^+|0\}}\psi_K^B(\mathbf{x}) &= e^{-i2\pi(m-1)/3}\psi_K^B(\mathbf{x}), \\ \overline{\{C_3^+|0\}}\psi_K^C(\mathbf{x}) &= e^{-i2\pi(m-2)/3}\psi_K^C(\mathbf{x}). \end{aligned} \quad (\text{S9})$$

Therefore, the CAM decreases by 1 when the configuration of the layers changes from **A** to **B**, and from **B** to **C**.

The  $K$  valley states at the layers of configurations  $\bar{\mathbf{A}}$ ,  $\bar{\mathbf{B}}$  and  $\bar{\mathbf{C}}$  can be obtained by  $180^\circ$  rotation along the z-axis as,

$$\begin{aligned}
\overline{\{C_2^+|0\}}\psi_K^m(\mathbf{x}) &= \sum_j e^{i\mathbf{K}\cdot\mathbf{R}_j} \overline{\{C_2^+|0\}} \overline{\{E|\mathbf{R}_j + \mathbf{t}_m\}} \phi(\mathbf{x}), \\
&= \sum_j e^{i\mathbf{K}\cdot\mathbf{R}_j} \overline{\{E|C_2^+\mathbf{R}_j + C_2^+\mathbf{t}_m\}} \overline{\{C_2^+|0\}} \phi(\mathbf{x}) \\
&= \sum_j e^{i\mathbf{K}\cdot\mathbf{R}_j} \phi(\mathbf{x} - C_2^+\mathbf{R}_j - C_2^+\mathbf{t}_m), \\
&= \sum_j e^{i(C_2^+\mathbf{K})(C_2^+\mathbf{R}_j)} \phi(\mathbf{x} - C_2^+\mathbf{R}_j - C_2^+\mathbf{t}_m), \\
&= \sum_j e^{i(-\mathbf{K})(C_2^+\mathbf{R}_j)} \phi(\mathbf{x} - C_2^+\mathbf{R}_j - C_2^+\mathbf{t}_m), \\
&= \psi_{-\mathbf{K}}^{\bar{m}}(\mathbf{x}).
\end{aligned} \tag{S10}$$

We have used the invariance of 4d orbitals  $\overline{\{C_2^+|0\}}\phi(\mathbf{x}) = \phi(\mathbf{x})$ . Note that the center of the Mo 4d orbital is translated by  $C_2^+\mathbf{t}_m = \mathbf{t}_{m'}$  corresponding to  $C_2^+\mathbf{t}_A \equiv \mathbf{t}_A$ ,  $C_2^+\mathbf{t}_B \equiv \mathbf{t}_C$ , and  $C_2^+\mathbf{t}_C \equiv \mathbf{t}_B$  modulo  $\mathbf{R}_j$ . The  $\psi_K^{\bar{m}}(\mathbf{x})$ , the time-reversal of  $\psi_{-\mathbf{K}}^{\bar{m}}(\mathbf{x})$ , consists of the complex conjugate of  $\phi(\mathbf{x})$  as

$$\psi_K^{\bar{m}}(\mathbf{x}) = \sum_j e^{i\mathbf{K}\cdot\mathbf{R}_j} \phi^*(\mathbf{x} - \mathbf{R}_j - \mathbf{t}_{m'}). \tag{S11}$$

The corresponding CAM's are obtained as

$$\begin{aligned}
\overline{\{C_3^+|0\}}\psi_{\mathbf{K}}^{\bar{\mathbf{A}}}(\mathbf{x}) &= e^{i2\pi m_l/3}\psi_{\mathbf{K}}^{\bar{\mathbf{A}}}(\mathbf{x}), \\
\overline{\{C_3^+|0\}}\psi_{\mathbf{K}}^{\bar{\mathbf{B}}}(\mathbf{x}) &= e^{-i2\pi(-m_l-1)/3}\psi_{\mathbf{K}}^{\bar{\mathbf{B}}}(\mathbf{x}), \\
\overline{\{C_3^+|0\}}\psi_{\mathbf{K}}^{\bar{\mathbf{C}}}(\mathbf{x}) &= e^{-i2\pi(-m_l-2)/3}\psi_{\mathbf{K}}^{\bar{\mathbf{C}}}(\mathbf{x}).
\end{aligned} \tag{S12}$$

#### 4.5.3 Calculation of double group representation

For point group  $\mathbf{G} = \{R\}$ , the single- and double-valued representations of the  $\mathbf{G}$  on the spatial and spin function spaces are obtained respectively as,

$$R_{space}\psi_p = \sum_q \psi_q D(R)_{qp}, \tag{S13}$$

$$R_{spin}\chi_r = \sum_{s=\pm} \chi_s \mathcal{D}^{1/2}(R)_{sr}. \tag{S14}$$

Given stacking structure, the basis of spatial function space  $\{\psi_p\}$  corresponds to the ordered set of  $K$  valley states localized at each layer (i.e. the  $\psi_{\mathbf{K}}^m$  or  $\psi_{\mathbf{K}}^{\bar{m}}$  at  $n$ -th layer). The spin function space  $\{\chi_r\}$  transforms under the point group symmetries corresponding to the two-dimensional spinor space spanned by  $\chi_+ = [1 \ 0]$  and  $\chi_- = [0 \ 1]$  under the  $2 \times 2$  unitary matrices  $\mathcal{D}^{1/2}(R) \in \text{SU}(2)$ . The representation  $\Gamma$  of  $\mathbf{G}^\dagger$  (double group of  $\mathbf{G}$ ) on the space spanned by basis  $\eta = \{\Psi_i\} = \{\psi_p \otimes \chi_r\}$  is then, constructed by the Kronecker product of matrices  $\Gamma(R) = D(R) \otimes \mathcal{D}^{1/2}(R)$ .

Finding the IRs and symmetry-adapted forms of the  $K$  valley states is straightforward by the block-diagonalization of  $\Gamma$  by the similarity transformation  $\tilde{\Gamma} = U^{-1}\Gamma U$  (See the text[44] for the details).

In the bilayer 3R, the bases of the space of the VB and CB states (**BC** stacking, refer to the Table 4.2 for CAMs) can be written in row vector forms as

$$\eta^{VB} = \left[ |1,1\rangle \otimes \chi_+ \quad |1,1\rangle \otimes \chi_- \quad |2,0\rangle \otimes \chi_+ \quad |2,0\rangle \otimes \chi_- \right] \quad (\text{S15})$$

$$\eta^{CB} = \left[ |1,-1\rangle \otimes \chi_+ \quad |1,-1\rangle \otimes \chi_- \quad |2,1\rangle \otimes \chi_+ \quad |2,1\rangle \otimes \chi_- \right] \quad (\text{S16})$$

The double group of the group of wave vector (GWV) of  $K$  of the 3R is  $C_3^\dagger = \{E, C_3^+, C_3^-, \bar{E}, \bar{C}_3^+, \bar{C}_3^-\}$ . The generator of the cyclic group is  $C_3^+$ , and its representations with the bases are given as

$$\Gamma^{VB}(C_3^+) = \begin{bmatrix} -1 & 0 & 0 & 0 \\ 0 & -\omega & 0 & 0 \\ 0 & 0 & -\omega & 0 \\ 0 & 0 & 0 & -\omega^* \end{bmatrix}_{\eta^{VB}}, \quad (\text{S17})$$

$$\Gamma^{CB}(C_3^+) = \begin{bmatrix} -\omega^* & 0 & 0 & 0 \\ 0 & -1 & 0 & 0 \\ 0 & 0 & -1 & 0 \\ 0 & 0 & 0 & -\omega \end{bmatrix}_{\eta^{CB}}, \quad (\text{S18})$$

where  $\omega = e^{2\pi i/3}$ . The representations of the remaining elements of  $C_3^+$  can be generated according to the multiplication table, and are already in the diagonal form with respect to the present bases since the product of diagonal matrices is diagonal. By referring to the character table (Table 4.4), the representations are decomposed into

$$\Gamma^{VB} = 2\Gamma_4 + \Gamma_5 + \Gamma_6, \quad (\text{S19})$$

$$\Gamma^{CB} = \Gamma_4 + \Gamma_5 + 2\Gamma_6. \quad (\text{S20})$$

Note that the each  $\Gamma^{VB}$  and  $\Gamma^{CB}$  contains the (isotypic) two-dimensional reducible representation which is the direct sum of two equivalent one-dimensional IR of  $\Gamma_4$  and  $\Gamma_6$ , respectively. It is because each pair of states localized at opposite layers with opposite spins,  $|1,1\rangle \otimes \chi_-$  and  $|2,0\rangle \otimes \chi_+$  (Equation (S15)), and  $|1,-1\rangle \otimes \chi_-$  and  $|2,1\rangle \otimes \chi_+$  (Equation (S16)), has the same phase under  $C_3^+$  (Equations (S17) and (S18)). Accordingly, the diagonal forms of  $\Gamma^{VB}$  and  $\Gamma^{CB}$  are retained under the arbitrary unitary transforms which result in the delocalization and depolarization of spin. The degree of the superposition is determined by actual form of the Hamiltonian of the system. However, sizable built-in interlayer potential in 3R (and Zeeman splitting at VB as well) will hinder the superposition although degree of the superposition is tunable by external electric field. It should be noted that the definite spin-polarizations at K valley are guaranteed only at

monolayer having GWV of Abelian  $C_{3h}^+$  where all the available IRs enforce simultaneous eigenstate of  $C_3^+$  and  $\sigma_h$ , and there is no neighboring layers for the superposition. It may explain spin-polarization at CB states despite the negligible Zeeman splitting.

Table 4.4 Character table of double group  $C_3^\dagger$  [44].

Mulliken	Koster <i>et. al.</i>	E	$C_3^+$	$C_3^-$	$\bar{E}$	$\bar{C}_3^+$	$\bar{C}_3^-$
A	$\Gamma_1$	1	1	1	1	1	1
${}^2E$	$\Gamma_2$	1	$\omega$	$\omega^*$	1	$\omega$	$\omega^*$
${}^1E$	$\Gamma_3$	1	$\omega^*$	$\omega$	1	$\omega^*$	$\omega$
${}^1\bar{E}$	$\Gamma_4$	1	$-\omega$	$-\omega^*$	-1	$\omega$	$\omega^*$
${}^2\bar{E}$	$\Gamma_5$	1	$-\omega^*$	$-\omega$	-1	$\omega^*$	$\omega$
$\bar{A}$	$\Gamma_6$	1	-1	-1	-1	1	1

$$\omega = e^{2\pi i/3}$$

On the other hand, the bases for the VB and CB states of bilayer 2H ( $\overline{\text{BC}}$  stacking, refer to the Table 4.2 for CAMs) are given

$$\eta^{VB} = [ |1,0\rangle \otimes \chi_+ \quad |1,0\rangle \otimes \chi_- \quad |2,0\rangle \otimes \chi_+ \quad |2,0\rangle \otimes \chi_- ], \quad (\text{S21})$$

$$\eta^{CB} = [ |1,-1\rangle \otimes \chi_+ \quad |1,-1\rangle \otimes \chi_- \quad |2,1\rangle \otimes \chi_+ \quad |2,1\rangle \otimes \chi_- ]. \quad (\text{S22})$$

The double group of the GWV of  $K$  is  $D_3^\dagger = \{E, C_3^+, C_3^-, C'_{21}, C'_{22}, C'_{23}, \overline{E}, \overline{C}_3^+, \overline{C}_3^-, \overline{C}'_{21}, \overline{C}'_{22}, \overline{C}'_{23}\}$ , and the representations of group generators are

$$\Gamma^{VB}(C_3^+) = \begin{bmatrix} -\omega & 0 & 0 & 0 \\ 0 & -\omega^* & 0 & 0 \\ 0 & 0 & -\omega & 0 \\ 0 & 0 & 0 & -\omega^* \end{bmatrix}_{\eta^{VB}}, \quad \Gamma^{VB}(C'_{21}) = \begin{bmatrix} 0 & 0 & 0 & -i \\ 0 & 0 & -i & 0 \\ 0 & -i & 0 & 0 \\ -i & 0 & 0 & 0 \end{bmatrix}_{\eta^{VB}}, \quad (\text{S23})$$

$$\Gamma^{CB}(C_3^+) = \begin{bmatrix} -\omega^* & 0 & 0 & 0 \\ 0 & -1 & 0 & 0 \\ 0 & 0 & -1 & 0 \\ 0 & 0 & 0 & -\omega \end{bmatrix}_{\eta^{CB}}, \quad \Gamma^{CB}(C'_{21}) = \begin{bmatrix} 0 & 0 & 0 & -i \\ 0 & 0 & -i & 0 \\ 0 & -i & 0 & 0 \\ -i & 0 & 0 & 0 \end{bmatrix}_{\eta^{CB}}. \quad (\text{S24})$$

By orthogonality relationships for characters (Table 4.5), the representations are decomposed into the IRs including the degenerate  $\Gamma_4$  as

$$\Gamma^{VB} = 2\Gamma_4, \quad (\text{S25})$$

$$\Gamma^{CB} = \Gamma_4 + \Gamma_5 + \Gamma_6. \quad (\text{S26})$$

Table 4.5 Character table of double group  $D_3^\dagger$  [44].

Mulliken	Koster <i>et. al.</i>	$E$	$\bar{E}$	$C_3^+, C_3^-$	$\bar{C}_3^+, \bar{C}_3^-$	$C'_{21}, C'_{22}, C'_{23}$	$\bar{C}'_{21}, \bar{C}'_{22}, \bar{C}'_{23}$
$A$	$\Gamma_1$	1	1	1	1	1	1
$A_2$	$\Gamma_2$	1	1	1	1	-1	-1
$E$	$\Gamma_3$	2	2	-1	-1	0	0
$\bar{E}_1$	$\Gamma_4$	2	2	1	-1	0	0
${}^1\bar{E}$	$\Gamma_5$	1	-1	-1	1	$i$	$-i$
${}^2\bar{E}$	$\Gamma_6$	1	-1	-1	1	$-i$	$i$

For the block-diagonalization of  $\Gamma^{VB}(C'_{21})$ , we can choose  $U$  which preserves the diagonal form of the  $\Gamma^{VB}(C'_3)$ . It has the form as

$$U = \begin{bmatrix} \cos \alpha & 0 & \sin \alpha & 0 \\ 0 & \cos \beta & 0 & \sin \beta \\ -\sin \alpha & 0 & \cos \alpha & 0 \\ 0 & -\sin \beta & 0 & \cos \beta \end{bmatrix}, \quad (\text{S27})$$

and arbitrarily mixes the  $|1,0\rangle \otimes \chi_+$  and  $|2,0\rangle \otimes \chi_+$ , and the  $|1,0\rangle \otimes \chi_-$  and  $|2,0\rangle \otimes \chi_-$ , respectively. The similarity transform of the  $\Gamma^{VB}(C'_{21})$  is given

$$\begin{aligned} \Gamma^{VB'}(C'_{21}) &= U^{-1} \Gamma^{VB}(C'_{21}) U \\ &= \begin{bmatrix} 0 & i \sin(\alpha + \beta) & 0 & -i \cos(\alpha + \beta) \\ i \sin(\alpha + \beta) & 0 & -i \cos(\alpha + \beta) & 0 \\ 0 & -i \cos(\alpha + \beta) & 0 & -i \sin(\alpha + \beta) \\ -i \cos(\alpha + \beta) & 0 & -i \sin(\alpha + \beta) & 0 \end{bmatrix}_{VB'} \end{aligned}, \quad (\text{S28})$$

and the  $\eta^{VB}$  transforms correspondingly into

$$\eta^{VB} U = \begin{bmatrix} (\cos \alpha |1,0\rangle - \sin \alpha |2,0\rangle) \otimes \chi_+ \\ (\cos \beta |1,0\rangle - \sin \beta |2,0\rangle) \otimes \chi_- \\ (\sin \alpha |1,0\rangle + \cos \alpha |2,0\rangle) \otimes \chi_+ \\ (\sin \beta |1,0\rangle + \cos \beta |2,0\rangle) \otimes \chi_- \end{bmatrix}^T. \quad (\text{S29})$$

The  $\Gamma^{VB}$  becomes the block-diagonal form corresponding to the Equation (S25) if  $\alpha + \beta = \pi(m+1/2)$ , where  $m$  is an integer. The substitution with  $\beta = -\alpha + \pi/2$  into Equation (S29) yields the symmetry-adapted form of  $K$  valley states for VB states as

$$\eta^{VB} \mathbf{U} = \begin{bmatrix} (\cos \alpha |1,0\rangle - \sin \alpha |2,0\rangle) \otimes \chi_+ \\ (\sin \alpha |1,0\rangle - \cos \alpha |2,0\rangle) \otimes \chi_- \\ (\sin \alpha |1,0\rangle + \cos \alpha |2,0\rangle) \otimes \chi_+ \\ (\cos \alpha |1,0\rangle + \sin \alpha |2,0\rangle) \otimes \chi_- \end{bmatrix}^T. \quad (\text{S30})$$

The resultant states spanning the two-dimensional  $\Gamma_4$  are spin-polarized and localized at opposite layer. The degree of the localization depends on the parameter  $\alpha$ . In addition, the anti-bonding and bonding characteristics of the VB states from the relative phases are also clearly determined.

The representation on CB space is decomposed in a similar way. We choose  $\mathbf{U}$  preserving the diagonal form of  $\Gamma^{CB}(C_3^+)$  as

$$\mathbf{U} = \begin{bmatrix} 1 & 0 & 0 & 0 \\ 0 & \cos \alpha & \sin \alpha & 0 \\ 0 & -\sin \alpha & \cos \alpha & 0 \\ 0 & 0 & 0 & 1 \end{bmatrix}. \quad (\text{S31})$$

The similarity transformation of  $\Gamma^{CB}(C'_{21})$  is given

$$\begin{aligned} \Gamma^{CB'}(C'_{21}) &= U^{-1}\Gamma^{CB}(C'_{21})U \\ &= \begin{bmatrix} 0 & 0 & 0 & -i \\ 0 & i \sin 2\alpha & -i \cos 2\alpha & 0 \\ 0 & -i \cos 2\alpha & -i \sin 2\alpha & 0 \\ -i & 0 & 0 & 0 \end{bmatrix}_{CB'} \end{aligned} \quad (\text{S32})$$

and the  $\eta^{CB}$  changes correspondingly as

$$\eta^{CB}U = \begin{bmatrix} |1,-1\rangle \otimes \chi_+ \\ \cos \alpha |1,-1\rangle \otimes \chi_- - \sin \alpha |2,1\rangle \otimes \chi_+ \\ \sin \alpha |1,-1\rangle \otimes \chi_- + \cos \alpha |2,1\rangle \otimes \chi_+ \\ |2,1\rangle \otimes \chi_- \end{bmatrix}^T. \quad (\text{S33})$$

The  $\Gamma^{CB}$  becomes the block-diagonal corresponding to the Equation (S26) when  $2\alpha = \pi(m+1/2)$  where  $m$  is an integer, and is simply permuted (e.g.  $(\cos \alpha |1,-1\rangle \otimes \chi_- - \sin \alpha |2,1\rangle \otimes \chi_+)$  and  $|2,1\rangle \otimes \chi_-$ ). The substitution with  $\alpha = \pi/4$  into Equation (S33) yields the symmetry-adapted form of the  $K$  valley states for the CB states as

$$\eta^{CB}U = \begin{bmatrix} |1,-1\rangle \otimes \chi_+ \\ 1/\sqrt{2}(|1,-1\rangle \otimes \chi_- - |2,1\rangle \otimes \chi_+) \\ 1/\sqrt{2}(|1,-1\rangle \otimes \chi_- + |2,1\rangle \otimes \chi_+) \\ |2,1\rangle \otimes \chi_- \end{bmatrix}^T. \quad (\text{S34})$$

Note that the anti-bonding and bonding like delocalized states spanning the

one-dimensional  $\Gamma_5$  and  $\Gamma_6$  have an unpolarized spin in contrast to the degenerate states. The one-dimensional IRs of  $D_3^\dagger$  should have a definite phase under the in-plane 2-fold symmetries, classes of  $\{C'_{21}, C'_{22}, C'_{23}\}$  and  $\{\bar{C}'_{21}, \bar{C}'_{22}, \bar{C}'_{23}\}$ , which interchange the upper and lower layers, and up and down spins. It enforces the non-degenerate states in the 2H to have symmetric delocalization over layers with unpolarized spin.

Under the vertical electric field of magnitude  $\varepsilon$ , the present symmetry-adapted form of K valley states should be altered to comply with new symmetry. In 3R, we can stick to the present form of states (with possible mixing between the same IRs) since the  $C_3^\dagger$  symmetry is preserved under the vertical field. In contrast, symmetry of 2H is lowered to  $C_3^\dagger$  accompanied by abrupt splitting of states. Nonetheless, the present bases in the Equation (S30) and (S34) are the ones making the matrices  $\Gamma^{VB}(C_3^+)$  and  $\Gamma^{CB}(C_3^+)$  diagonal, and hence, are already symmetry-adapted form under the  $C_3^\dagger$  symmetry. In this case, the pair of wavefunctions consisting of degenerate subspace are splitted preserving the spin-polarization according to the energy splitting by the interlayer potential  $\sim \varepsilon d$  where  $d$  is the interlayer distance. If we suppose that the adiabatic change of wavefunctions is continuous at the instant of the symmetry breaking (infinitesimal field  $\varepsilon \rightarrow 0$ ), the present choice of spin-polarized bases for VB states is the only option although the choice of basis

in the degenerate space is arbitrary. For non-degenerate states, the  $\Gamma_5$  and  $\Gamma_6$  of  $D_3^\dagger$  are merged into the same  $\Gamma_6$  of  $C_3^\dagger$  which may promote delocalization by anti-crossing, at the small electric field regim, against the opposite localization effect driven by electric field.

#### 4.6 References

- [1] Xu X, Yao W, Xiao D and Heinz T F 2014 *Nat. Phys.* 10 343–50
- [2] Xia F, Wang H, Xiao D, Dubey M and Ramasubramaniam A 2014 *Nat. Photon.* 8 899–907
- [3] Xiao D, Liu G B, Feng W, Xu X and Yao W 2012 *Phys. Rev. Lett.* 108 196802
- [4] Yao W, Xiao D and Niu Q 2008 *Phys. Rev. B* 77 235406
- [5] Manchon A, Koo H C, Nitta J, Frolov S M and Duine R A 2015 *Nat. Mater.* 14 871–82
- [6] Gong Z, Liu G B, Yu H, Xiao D, Cui X, Xu X and Yao W 2013 *Nat. Commun.* 4 1–6
- [7] Hong X, Kim J, Shi S F, Zhang Y, Jin C, Sun Y, Tongay S, Wu J, Zhang Y and Wang F 2014 *Nat. Nanotechnol.* 9 682–6
- [8] Rivera P et al 2015 *Nat. Commun.* 6 6242
- [9] Rivera P, Seyler K L, Yu H, Schaibley J R, Yan J, Mandrus D G, Yao W and Xu X 2016 *Science* 351 688–91

- [10] Yu Y et al 2015 *Nano Lett.* 15 486–91
- [11] Chen H et al 2016 *Nat. Commun.* 7 12512
- [12] Kozawa D, Carvalho A, Verzhbitskiy I, Giustiniano F, Miyauchi Y, Mouri S, Castro Neto A H, Matsuda K and Eda G 2016 *Nano Lett.* 16 4087–93
- [13] Ceballos F, Bellus M Z, Chiu H Y and Zhao H 2014 *ACS Nano* 8 12717–24
- [14] Miller B, Steinhoff A, Pano B, Klein J, Jahnke F, Holleitner A and Wurstbauer U 2017 *Nano Lett.* 17 5229–37
- [15] Baranowski M et al 2017 *Nano Lett.* 17 6360–5
- [16] Hsu W T et al 2018 *Nat. Commun.* 9 1356
- [17] Kim J et al 2017 *Sci. Adv.* 3 e1700518
- [18] Akashi R, Ochi M, Bordács S, Suzuki R, Tokura Y, Iwasa Y and Arita R 2015 *Phys. Rev. Appl.* 4 014002
- [19] Akashi R, Iida Y, Yamamoto K and Yoshizawa K 2017 *Phys. Rev. B* 95 245401
- [20] Kresse G and Furthmüller J 1996 *Phys. Rev. B* 54 11169–86
- [21] Kresse G and Furthmüller J 1996 *Comput. Mater. Sci.* 6 15–50
- [22] Ceperley D M and Alder B J 1980 *Phys. Rev. Lett.* 45 566–9
- [23] Perdew J P, Burke K and Ernzerhof M 1996 *Phys. Rev. Lett.* 77 3865–8
- [24] Grimme S 2006 *J. Comput. Chem.* 27 1787–99
- [25] Grimme S, Antony J, Ehrlich S and Krieg H 2010 *J. Chem. Phys.* 132 154104

- [26] Blöchl P E 1994 *Phys. Rev. B* 50 17953–79
- [27] King-Smith R D and Vanderbilt D 1993 *Phys. Rev. B* 47 1651–4
- [28] Baroni S and Resta R 1986 *Phys. Rev. B* 33 7017–21
- [29] Gajdoš M, Hummer K, Kresse G, Furthmüller J and Bechstedt F 2006 *Phys. Rev. B* 73 045112
- [30] Giannozzi P et al 2009 *J. Phys.: Condens. Matter* 21 395502
- [31] Giannozzi P et al 2017 *J. Phys.: Condens. Matter* 29 465901
- [32] Bengtsson L 1999 *Phys. Rev. B* 59 12301–4
- [33] Schönfeld B, Huang J J and Moss S C 1983 *Acta Crystallogr. B* 39 404–7
- [34] Frindt R F and Yoffe A D 1963 *Proc. R. Soc. A* 273 69–83
- [35] Ribeiro-Soares J, Almeida R M, Barros E B, Araujo P T, Dresselhaus M S, Cançado L G and Jorio A 2014 *Phys. Rev. B* 90 115438
- [36] Belabbes A, Furthmüller J and Bechstedt F 2013 *Phys. Rev. B* 87 035305
- [37] Bauer B, Hubmann J, Lohr M, Reiger E, Bougeard D and Zweck J 2014 *Appl. Phys. Lett.* 104 211902
- [38] Andersen K, Latini S and Thygesen K S 2015 *Nano Lett.* 15 4616–21
- [39] Cheiwchanchamnangij T and Lambrecht W R L 2012 *Phys. Rev. B* 85 205302
- [40] Fan X, Zheng W T, Kuo J L, Singh D J, Sun C and Zhu W 2016 *Sci. Rep.* 6 24140
- [41] Ding W, Zhu J, Wang Z, Gao Y, Xiao D, Gu Y, Zhang Z and Zhu W 2017 *Nat. Commun.* 8 14956

- [42] Kuo Y H, Lee Y K, Ge Y, Ren S, Roth J E, Kamins T I, Miller D A B and Harris J S 2005 *Nature* 437 1334–6
- [43] Liu G B, Xiao D, Yao Y, Xu X and Yao W 2015 *Chem. Soc. Rev.* 44 2643–63
- [44] Bradley C and Cracknell A 2010 *The Mathematical Theory of Symmetry in Solids: Representation Theory for Point Groups and Space Groups* (Oxford: Oxford University Press)
- [45] Pientka F, Gradhand M, Fedorov D V, Mertig I and Györffy B L 2012 *Phys. Rev. B* 86 054413
- [46] Jones A M, Yu H, Ross J S, Klement P, Ghimire N J, Yan J, Mandrus D G, Yao W and Xu X 2014 *Nat. Phys.* 10 130–4
- [47] Suzuki R et al 2014 *Nat. Nanotechnol.* 9 611–7
- [48] Yu H, Wang Y, Tong Q, Xu X and Yao W 2015 *Phys. Rev. Lett.* 115 187002
- [49] Wu F, Lovorn T and MacDonald A H 2018 *Phys. Rev. B* 97 035306
- [50] Wang H, Bang J, Sun Y, Liang L, West D, Meunier V and Zhang S 2016 *Nat. Commun.* 7 11504
- [51] Zhang J, Hong H, Lian C, Ma W, Xu X, Zhou X, Fu H, Liu K and Meng S 2017 *Adv. Sci.* 4 1700086
- [52] Berera R, van Grondelle R and Kennis J T M 2009 *Photosynth. Res.* 101 105–18
- [53] Hunt B M et al 2017 *Nat. Commun.* 8 948 [54] Mak K F, McGill K L, Park J and McEuen P L 2014 *Science* 344 1489–92

- [55] Zhu X, Monahan N R, Gong Z, Zhu H, Williams K W and Nelson C A  
2015 *J. Am. Chem. Soc.* 137 8313–20
- [56] Resta R 2010 *J. Phys. Condens. Matter* 22 123201

## CHAPTER 5

# FERROELECTRICITY OF LAYERED STRUCTURE WITH POLAR SYMMETRY

---

### 5.1 Introduction

Ferroelectric two-dimensional (2D) materials have great importance in realizing non-volatile devices with extreme feature size[1,2], and possibly with unforeseen functionalities from the unique properties of 2D materials[3,4]. However, the studies on the 2D ferroelectrics is yet an emerging field. Only a few materials such as SnTe[5],  $\alpha$ -In<sub>2</sub>Se<sub>3</sub>[6] were experimentally shown to work in agreement with theories[7–9]. Transition metal dichalcogenide (TMDC) is another major 2D materials class showing versatile electronic phases ranging from semiconducting or metallic phase to that with topological characteristics[10–12]. Nonetheless, the ferroelectricity of the TMDC is very scarce because the underlying symmetry of single layer

in stable phase is either non-polar or centrosymmetric, precluding the electric polarization; i.e. 2H ( $P\bar{6}m2$ ), 1T ( $P\bar{3}m1$ ) and distorted 1T ( $P2/m$ ) phases[11]. While theory showed ferroelectric instability of single layer 1T MoS<sub>2</sub>[13], its realization in the experiment is challenging because MoS<sub>2</sub> is stable in semiconducting 2H phase rather than metallic 1T structure[14].

The ferroelectricity likely appears in stacked TMDC rather than a single layer form. It was recently shown that the horizontal mirror symmetries of individual layers are broken by the stacking in 3R structure ( $P3m1$  for finite layers and  $R3m$  for bulk), hence the vertical electric polarization manifests itself according to the global polar symmetry[15]. The direction of polarization depends on the stacking sequence, hence is reversed by the interlayer translation between the AB and AC stackings[15,16] as shown in Figure 5.1(a). The possibility of ferroelectric switching in the 3R structure via the interlayer translation has not been explored to date. On the other hand, the multilayer distorted 1T WTe<sub>2</sub> showed switching of the polarization[17,18] and the topological phase[12] in the experiments, probably via the interlayer translation. The stability of the 3R structure MoS<sub>2</sub> is comparable to that of the 2H structure and can be selectively synthesized among competing polytypes[19]. It is hence a viable candidate for 2D ferroelectrics in which the fascinating phenomena such as high electron mobility[16] and valleytronics[15,19] can be explored altogether.

The interlayer translation universally manifests as Raman active low-frequency lattice vibrations in layered 2D crystals, due to the weak van der Waals bonds (vdW) between layers[20–22]. Therefore, the ferroelectric switching using an optical field based on ionic Raman scattering is considerably appealing[23–25]. A particular mechanism, called nonlinear phononics, relies on the anharmonic phonon coupling between infrared active and targeted secondary vibrational modes, which displaces the crystal toward the reversal of polarization upon the irradiation of intense terahertz pulse[26,27]. The use of pulse with the mid-infrared frequency within short duration allows exploring an extremely intense light field (peak electric field reaching  $\sim 600 \text{ MVcm}^{-1}$ ) without the material damage[28–30]. The optical ferroelectric switching is a rapidly growing topic, which will enable the ultrafast and nondestructive way to achieve coherent switching[26,27,31–33].

In this work, we theoretically show the possibility of the ferroelectric switching of the bilayer 3R MoS<sub>2</sub> using the intense light pulse through the anharmonic phonon coupling. Density functional theory (DFT) calculations show that a large amplitude vibration of infrared mode can effectively lower the ferroelectric switching barrier, and induce a unidirectional anharmonic force on the interlayer shear mode along the switching direction. This effect depends on the polarization angle of the incident light pulse with respect to the crystallographic axis of MoS<sub>2</sub> in accordance with the selection rule.

Lattice dynamics simulations indicate the possibility of dynamical ferroelectric switching through the coherent amplification of the interlayer shear mode and the lowering of the energy barrier under the repetitive pulses within a few picoseconds.

## 5.2 Methods

The density functional theory calculations were performed using the Vienna Ab-initio Simulation Package (VASP)[34,35]. The projector-augmented wave (PAW) method[36] and the cut-off energy of 500 eV were used with the valence electron configurations of Mo[4s<sup>2</sup>4p<sup>6</sup>5s<sup>2</sup>4d<sup>4</sup>] and S[3s<sup>2</sup>3p<sup>4</sup>], respectively. The generalized gradient approximation[37] with Grimme's D3 scheme[38] was used to describe the van der Waals interaction. The bilayer structure is simulated by the supercell containing ~40 Å of vacuum layer to avoid the artificial interaction between periodic images. The structures were fully relaxed until the residual forces on the atoms were less than 0.001 eVÅ<sup>-1</sup> using 24×24×1 k-mesh. The spontaneous polarization was calculated using Berry phase method[39]. The phonon calculation was performed using PHONOPY code[40] using 3×3×1 supercell and 8×8×1 k-mesh.

## 5.3 Results and Discussion

### 5.3.1 Electric polarization and switching in bilayer 3R MoS<sub>2</sub>

The bilayer 3R MoS<sub>2</sub> has the polar point group symmetry of  $C_{3v}$  with the polar axis along the z-axis. The 3R structure can be constructed by either AB or AC stacking sequence, which develops the spontaneous electric polarization in the opposite direction each other as shown in Figure 5.1(a). The magnitude of electric polarization of the bilayer structure was calculated to be  $P = 0.24 \mu\text{Ccm}^{-2}$  from the Berry phase method, in agreement with previous reports[15,16]. Figure 5.1(b) shows the total energy of the bilayer structure (primitive cell consisting of 6 atoms) depending on the stacking sequence calculated by using the nudged elastic band (NEB) method. Both the AB and AC stackings are stable and energetically degenerate structures. The AC stacking is obtained from the AB stacking by sliding the upper B layer along the +y direction by 1.82 Å. The interlayer translation over the weak vdW interaction results in the modest energy barrier  $\Phi_{\text{NEB}} = 15.0 \text{ meV}$ .

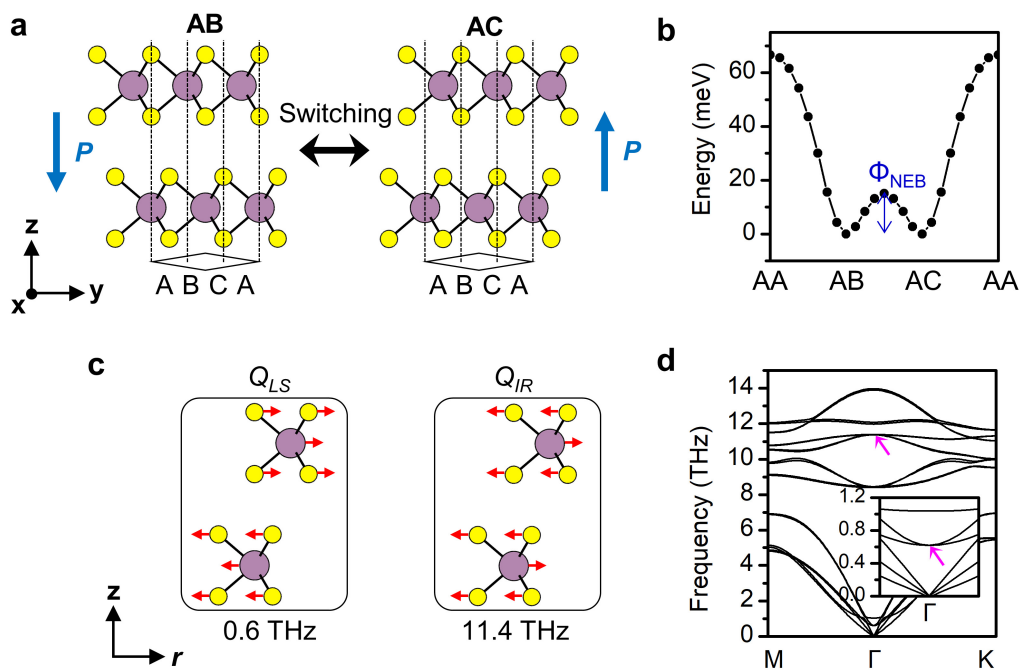


Figure 5.1 (a) Stacking-dependent spontaneous polarization of bilayer 3R MoS<sub>2</sub>. (b) Energy of the bilayer structure depending on the stacking sequence.  $\Phi_{NEB}$  is the ferroelectric switching barrier calculated by the NEB method. (c) Displacement patterns of the interlayer shear mode ( $Q_{LS}$ ) and the infrared mode ( $Q_{IR}$ ) mode along the in-plane polarization direction  $r$ . (d) Phonon dispersion of the bilayer 3R MoS<sub>2</sub>. The zone-center  $Q_{LS}$  mode at 0.6 THz and  $Q_{IR}$  mode at 11.4 THz are denoted by arrows.

We investigate the optical switching mechanism based on the nonlinear phononics[23,24]. The bilayer 3R MoS<sub>2</sub> has 18 zone-center phonon modes which are decomposed into  $\Gamma = 6A_1+6E$  representations. The singly degenerate A<sub>1</sub> mode involves out-of-plane motion of atoms, while the doubly degenerate E mode involves in-plane motion of atoms. Figure 5.1(c) shows two kinds of E modes relevant to the nonlinear phononics mechanism. The low-frequency mode ( $\Omega_{LS} = 0.6$  THz in phonon dispersion in Figure 5.1(d)) referred to as the interlayer shear mode (denoted by  $Q_{LS}$ ) involves the relative motion between adjacent layers along the in-plane polarization axis  $r$ . Therefore, the  $Q_{LS}$  mode is related to the AB $\leftrightarrow$ AC stacking change. The infrared activity of the  $\nu$ -th mode is proportional to the square of mode effective charge  $Z_{\nu}^*$ [41]. Due to the almost rigid relative ionic motion, the  $Q_{LS}$  mode does not produce net dipole moment as the calculated effective charge  $Z_{LS}^* = 0.00 e\mu^{-1/2}$  (where  $e$  is the electronic charge and  $\mu$  is the atomic mass unit). The vanishing infrared activity indicates that it is almost impossible to directly excite the  $Q_{LS}$  mode with large amplitude for the stacking change. Nonetheless, the anharmonic coupling of  $Q_{LS}$  mode with other infrared active modes can provide an alternative route to control this mode, and the ferroelectric switching. Among the other in-plane modes, only the high-frequency mode (denoted by  $Q_{IR}$ ) at  $\Omega_{IR} = 11.4$  THz shows finite effective charge  $Z_{IR}^* = 0.23 e\mu^{-1/2}$ , and is the solely infrared active mode under the vertical incidence of light.

The normal-mode coordinate  $Q_\nu$  of  $\nu$ -th mode is related to the atomic displacement vector  $U_i^\nu = \frac{Q_\nu}{\sqrt{m_i}} e_i^\nu$  where  $m_i$  is the atomic mass of  $i$ -th atom and  $e_i^\nu$  is the normalized eigenvector of the dynamical matrix. We chose the orthogonal basis set to represent the degenerate  $Q_{LS}$  and  $Q_{IR}$  modes as  $\{Q_{LSx}, Q_{LSy}\}$  and  $\{Q_{IRx}, Q_{IRy}\}$ . They correspond to the linear polarization along the zigzag (x-axis) and armchair (y-axis) axes shown in the top view of the AB stacking of the 3R MoS<sub>2</sub> in Figure 5.2(a). The AB stacking deformed by the positive amplitude of  $Q_{LSy} = +16.29 \text{ \AA}\sqrt{\mu}$  (atomic displacement of the each of the adjacent layers in the opposite direction by 0.91 \text{ \AA}) corresponds to the AC stacking. Meanwhile, the deformation by the negative amplitude of the  $Q_{LSy} = -16.29 \text{ \AA}\sqrt{\mu}$  changes the AB stacking into the unstable AA stacking. The positive amplitude of  $Q_{LS}$  along the three crystallographically equivalent directions,  $r_1$  (+y direction),  $r_2$  and  $r_3$  directions ( $-120^\circ$  and  $+120^\circ$  from the +y direction), equally change the AB stacking into AC stacking as shown in Figure 5.2(a).

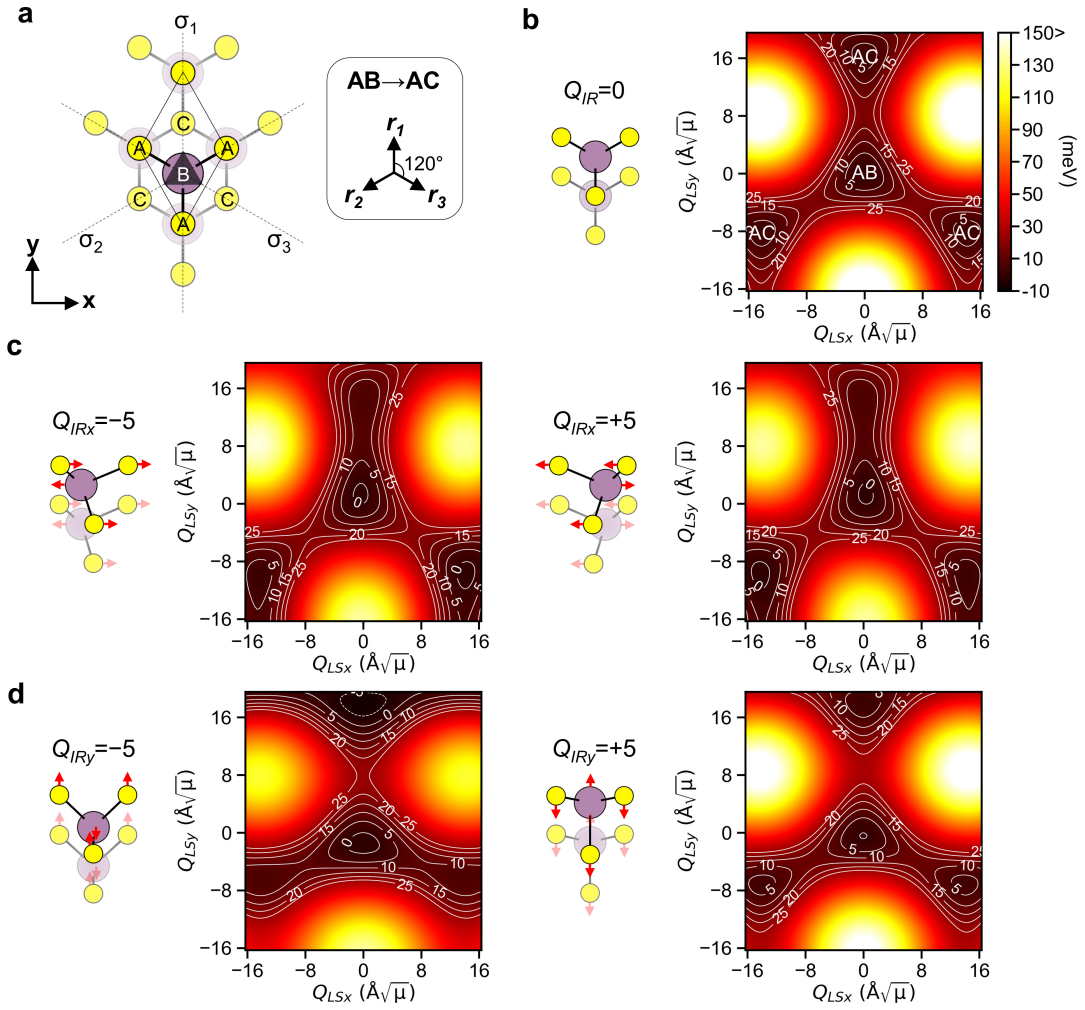


Figure 5.2 (a) Top view of the AB stacked 3R MoS<sub>2</sub> showing the C<sub>3v</sub> symmetry. In the AB stacking, the S atoms in the upper layer are on the top of the Mo atoms in the lower layer (bottom layer is depicted as dimmed). The x- and y- axis corresponds to the zigzag and armchair axis of MoS<sub>2</sub>, respectively. The AB stacking changes to the AC stacking under the deformation induced by the positive amplitude of Q<sub>LS</sub> along the three equivalent directions r<sub>1</sub>, r<sub>2</sub> and r<sub>3</sub>. (b) Potential energy surface V(Q<sub>IR</sub>, Q<sub>LSx</sub>, Q<sub>LSy</sub>) on the (Q<sub>LSx</sub>, Q<sub>LSy</sub>) coordinates for Q<sub>IR</sub> = 0 Å√μ (μ is atomic mass unit). The AB stacking corresponds to the origin (0, 0). (c, d) Polarization-dependent modulation of the potential energy landscape at (c) Q<sub>IRx</sub> = ±5 Å√μ and at (d) Q<sub>IRy</sub> = ±5 Å√μ via anharmonic coupling.

The possibility of the ferroelectric switching based on the nonlinear phononics hinges on how much the  $Q_{LS}$  mode can be amplified along the desired direction for the  $AB \leftrightarrow AC$  stacking change by the coupling with  $Q_{IR}$ . Here, the anharmonic coupling property was investigated from the potential energy surfaces as a function of normal-mode coordinates. The potential energy surfaces  $V(Q_{IR}, Q_{LSx}, Q_{LSy})$  for each  $Q_{IRx}$  and  $Q_{IRy}$  were calculated using DFT on  $21 \times 21 \times 23$  points with steps of  $0.82 \text{ \AA}\sqrt{\mu}$  for  $Q_{IR}$  and  $1.63 \text{ \AA}\sqrt{\mu}$  for  $Q_{LS}$  modes. Then, the energy surface was fitted to the polynomial function as

$$V(Q_{IR}, Q_{LSx}, Q_{LSy}) = \sum_{\{l,m,n\}} c_{lmn} Q_{IR}^l Q_{LSx}^m Q_{LSy}^n \quad \text{Eq. 1}$$

where  $Q_{IR}$  is either  $Q_{IRx}$  or  $Q_{IRy}$ , and  $c_{lmn}$  is the anharmonic coefficient, and  $Q_{IR}^l$ ,  $Q_{LSx}^m$  and  $Q_{LSy}^n$  denote the  $l$ ,  $m$  and  $n$  powers of the normal-mode coordinates, respectively. By this expression, we analyze the effect of the irradiating light pulse with the linear polarization along the x- or y-axis, thus exciting  $Q_{IRx}$  or  $Q_{IRy}$  mode, respectively. Note that the normal-modes in the cartesian basis are classified into the odd parity modes ( $Q_{LSx}$  and  $Q_{IRx}$ ) and even parity modes ( $Q_{LSy}$  and  $Q_{IRy}$ ) under the mirror symmetry  $\sigma_1$  shown in Figure 2a. The mirror parity imposes the polarization-dependent selection rule on  $Q_{IRx}^l Q_{LSx}^m Q_{LSy}^n$  ( $Q_{IRy}^l Q_{LSx}^m Q_{LSy}^n$ ) coupling such that  $c_{lmn}$  is nonzero only for  $l+m = \text{even}$  ( $m = \text{even}$ ). We included the terms up to 15<sup>th</sup> power terms ( $l+m+n = 15$ ) in the polynomial function, which fits the DFT potential energy

surface accurately. The representative coupling terms are displayed in Table 5.1.

Figure 5.2(b) shows the potential energy surface  $V(Q_{IR}, Q_{LSx}, Q_{LSy})$  represented on  $(Q_{LSx}, Q_{LSy})$  coordinates when the amplitude of  $Q_{IR}$  is zero. The energy contour shows the directional dependence inherited from the  $C_{3v}$  symmetry. The energy barriers for the AB $\rightarrow$ AC change along the equivalent  $r_1$ ,  $r_2$  and  $r_3$  directions in this potential energy surface are the same as  $\Phi_0 = 17.3$  meV. The difference between  $\Phi_0$  and  $\Phi_{NEB}$  for the AB $\rightarrow$ AC stacking change comes from the fact that the deformation by the in-plane  $Q_{LS}$  mode does not include any out-of-plane relaxations, while the NEB path includes the relaxation from the small increase ( $\sim 1.6\%$ ) of the interlayer distance, reducing the barrier. It is worth to note that the  $\Phi_0$  rather than the  $\Phi_{NEB}$  is relevant to the ultrafast switching in the picosecond time scale, while the latter is relevant to the conventional switching in a longer time scale.

The anharmonic coupling effect can be seen from the modulation of the potential energy landscape under the large  $Q_{IR}$  amplitude. Figure 5.2(c) and (d) show the potential energy landscapes when the amplitude of  $Q_{IR}$  is set to  $\pm 5.00 \text{ \AA} \sqrt{\mu}$  along the x- and y-axis, respectively. This amplitude corresponds to the displacement of Mo atoms by  $\sim 0.23 \text{ \AA}$  and of S atoms by  $\sim 0.34 \text{ \AA}$  in opposite direction along the polarization axis. Due to the deformation, the  $C_{3v}$  symmetry of the potential surface on the  $(Q_{LSx}, Q_{LSy})$  coordinates is broken,

and the energy barriers along the three equivalent directions become different. Under the negative amplitude of  $Q_{IRx} = -5.00 \text{ \AA}\sqrt{\mu}$ , the energy barrier along the  $r_1$  direction significantly decreases to 8.6 meV, but that along the other directions increases to 19.4 meV ( $r_2$  direction) and 21.3 meV ( $r_3$  direction), respectively. The energy landscape for the positive amplitude  $Q_{IRx} = +5.00 \text{ \AA}\sqrt{\mu}$  is essentially the same with that for negative amplitude, except for the fact that the energy contour is flipped with respect to the mirror  $\sigma_1$ . For both signs of  $Q_{IRx}$ , the coordinate of the potential energy minimum is slightly shifted along the  $r_1$  direction from the origin ( $Q_{LSx} = Q_{LSy} = 0 \text{ \AA}\sqrt{\mu}$ ).

By contrast, the amplitude of  $Q_{IRy}$  largely increases the energy barrier along the  $r_1$  direction (31.7 meV at  $Q_{IRy} = -5.00 \text{ \AA}\sqrt{\mu}$ , and 23.8 meV at  $Q_{IRy} = +5.00 \text{ \AA}\sqrt{\mu}$ ). This is accompanied by the slight shift of the potential minimum along the  $-r_1$  ( $-y$ ) direction. The energy landscape is symmetric with respect to the mirror plane  $\sigma_1$ , and the energy barrier along the  $r_2$  and  $r_3$  directions are reduced (13.4 meV at  $Q_{IRy} = -5.00 \text{ \AA}\sqrt{\mu}$ , and 10.1 meV at  $Q_{IRy} = +5.00 \text{ \AA}\sqrt{\mu}$ ). The change of energy barriers and the shift of the potential minimum indicate that the coupling of  $Q_{LS}$  and  $Q_{IR}$  modes exerts an anharmonic force on the  $Q_{LS}$  mode. This will be explained later in more detail.

Table 5.1 The anharmonic coefficient  $c_{lmn}$  for  $Q_{IR}^l Q_{LSx}^m Q_{LSy}^n$  coupling terms for each  $Q_{IRx}$  and  $Q_{IRy}$  mode. The values are shown up to 5th power coupling terms in unit of  $\text{meV}\text{\AA}^{-(l+m+n)}\mu^{-(l+m+n)/2}$ .

$l$	$m$	$n$	$Q_{IRx}$	$Q_{IRy}$	$l$	$m$	$n$	$Q_{IRx}$	$Q_{IRy}$
0	0	3	$-5.64 \times 10^{-2}$	$-5.71 \times 10^{-2}$	1	3	0	$1.07 \times 10^{-3}$	
0	0	4	$-2.48 \times 10^{-3}$	$-2.29 \times 10^{-3}$	1	3	1	$1.15 \times 10^{-4}$	
0	0	5	$1.22 \times 10^{-4}$	$1.22 \times 10^{-4}$	1	4	0		$-1.01 \times 10^{-3}$
0	2	0	$7.93 \times 10^{-1}$	$7.90 \times 10^{-1}$	2	0	0	$2.66 \times 10^{-2}$	$2.62 \times 10^{-2}$
0	2	1	$1.70 \times 10^{-1}$	$1.71 \times 10^{-1}$	2	0	1	$-6.64 \times 10^{-2}$	$1.03 \times 10^{-1}$
0	2	2	$-4.92 \times 10^{-3}$	$-4.79 \times 10^{-3}$	2	0	2	$-3.28 \times 10^{-3}$	$-6.17 \times 10^{-4}$
0	2	3	$-2.85 \times 10^{-4}$	$-2.88 \times 10^{-4}$	2	0	3	$5.91 \times 10^{-4}$	$-5.58 \times 10^{-5}$
0	4	0	$-2.38 \times 10^{-3}$	$-2.30 \times 10^{-3}$	2	2	0	$3.98 \times 10^{-4}$	$-6.14 \times 10^{-3}$
0	4	1	$-3.76 \times 10^{-4}$	$-4.00 \times 10^{-4}$	2	2	1	$1.30 \times 10^{-4}$	$-1.13 \times 10^{-3}$
1	0	1		$1.81 \times 10^{-2}$	3	0	0		$-5.66$
1	0	2		$5.43 \times 10^{-2}$	3	0	1		$-1.5710^{-2}$
1	0	3		$2.36 \times 10^{-3}$	3	0	2		$-5.75 \times 10^{-3}$
1	0	4		$-5.05 \times 10^{-4}$	3	1	0	$8.91 \times 10^{-3}$	
1	1	0	$-1.05 \times 10^{-2}$		3	1	1	$1.66 \times 10^{-4}$	
1	1	1	$-1.69 \times 10^{-2}$		3	2	0		$-8.40 \times 10^{-3}$
1	1	2	$1.32 \times 10^{-3}$		4	0	0	$-1.81$	$-3.01 \times 10^{-1}$
1	1	3	$1.47 \times 10^{-4}$		4	0	1	$-2.41 \times 10^{-3}$	$-1.31 \times 10^{-2}$
1	2	0		$6.29 \times 10^{-2}$	5	0	0		$3.18 \times 10^{-1}$
1	2	1		$6.97 \times 10^{-4}$					
1	2	2		$-5.94 \times 10^{-4}$					

### 5.3.2 Dynamics of coupled normal-modes under light pulse

Next, we investigate the dynamical behavior of the normal-modes under light pulse with a specific polarization direction. Since the motion of the  $Q_{IR}$  mode is much faster than the  $Q_{LS}$ , the  $Q_{LS}$  modes experience the effective potential asserted by the rapidly oscillating  $Q_{IR}$  mode; i.e., time-averaged potential energy surface depending on  $Q_{IR}(t)$ . The dynamics of the nonlinearly coupled modes are simulated by the following coupled equations of motion,

$$\begin{aligned}
 \ddot{Q}_{IR} &= -\frac{\partial V(Q_{IR}, Q_{LSx}, Q_{LSy})}{\partial Q_{IR}} - \gamma_{IR} \dot{Q}_{IR} + F(t), \text{ where } Q_{IR} = \{Q_{IRx}, Q_{IRy}\}, \\
 \ddot{Q}_{LSx} &= -\frac{\partial V(Q_{IR}, Q_{LSx}, Q_{LSy})}{\partial Q_{LSx}} - \gamma_{LS} \dot{Q}_{LSx}, \\
 \ddot{Q}_{LSy} &= -\frac{\partial V(Q_{IR}, Q_{LSx}, Q_{LSy})}{\partial Q_{LSy}} - \gamma_{LS} \dot{Q}_{LSy},
 \end{aligned} \tag{Eq. 2}$$

where  $\gamma_{IR}$  and  $\gamma_{LS}$  are the damping coefficients for each mode, and  $F(t)$  is the optical driving force on the  $Q_{IR}$  mode. We used Gaussian pulse  $F(t) = Z_{IR}^* E_0 \sin(\Omega t) e^{-t^2/2\sigma^2} / \sigma \sqrt{2\pi}$ , where  $E_0$  is the amplitude of the electric field,  $\sigma$  is the duration of the pulse and  $\Omega$  is the frequency, respectively.

Figure 5.3 shows the evolution of potential energy curve on the  $Q_{LS}$  coordinate along the  $AB \rightarrow AC$  switching directions when the  $Q_{IR}$  mode is resonantly pumped by a pulse with  $\Omega = \Omega_{IR}$ ,  $E_0 = 34 \text{ MVcm}^{-1}$  and  $\sigma = 100$

fs. Such high intensity of the pulse is required to achieve the large amplitude of  $Q_{IR}$  ( $\sim 5 \text{ \AA}\sqrt{\mu}$ ) in MoS<sub>2</sub> in order to explore the strong anharmonic coupling effect. We note that the pulse intensity used here is comparable to the that used in the experiment on the high harmonic generation of the single layer MoS<sub>2</sub>[30]. The energy curve (black line) corresponds to the static case ( $Q_{IRx} = 0 \text{ \AA}\sqrt{\mu}$ ), where the energy of the AC stacking is not identical but slightly higher than that of the AB stacking because the layer-shearing by the  $Q_{LS}$  mode is not perfectly rigid.

The pulse polarized along the x-axis induces the oscillation of the  $Q_{IRx}$  mode with the amplitude between  $\pm 5.35 \text{ \AA}\sqrt{\mu}$  by which the potential curve changes (grey line). The time-averaged potential energy (orange line) results in the effective barrier  $\langle \Phi \rangle = 11.5 \text{ meV}$  along the  $r_1$  direction (Figure 5.3(a)), which is a significant reduction from the 17.3 meV for the static case. The coordinate of the potential minimum is shifted by  $0.72 \text{ \AA}\sqrt{\mu}$  along the  $r_1$  direction, and the energy of the AC stacking slightly increases compared to the static case. Meanwhile, a slight increase of the barrier to 19.2 meV along the  $r_2$  and  $r_3$  directions is observed (Figure 5.3(b)). In contrast, the  $Q_{IRy}$  mode under the y-polarized pulse shows asymmetric vibration between  $-4.69 \text{ \AA}\sqrt{\mu}$  and  $+5.43 \text{ \AA}\sqrt{\mu}$  in the anharmonic potential due to the lack of the mirror plane perpendicular to the y-axis. This results in an increase of the effective barrier along the  $r_1$  direction to 22.5 meV, and the shift of the potential minimum by

0.36  $\text{\AA}\sqrt{\mu}$  along the  $-r_1$  direction (Figure 5.3(c)). On the other hand, the effective energy barrier along the  $r_2$  and  $r_3$  directions diminishes to 14.4 meV (Figure 5.3(d)).

The polarization-dependent modulation of the effective potential energy can be explained by the characteristics of the anharmonic coupling terms. Overall trend is captured by the coupling terms in the form of  $Q_{IR}^l Q_{LSy}$  with even  $l$ , which impart an unidirectional anharmonic force on  $Q_{LSy}$  by

$$F_{anh} = -\sum_l^{even} c_{10l} \langle Q_{IR}^l \rangle.$$

It is noted that the sign of the coefficient of quadratic-linear term  $c_{201} Q_{IR}^2 Q_{LSy}$  determines the sign of  $F_{anh}$ . The calculated  $F_{anh}$  by the  $Q_{IRx}$  has the positive value of  $0.92 \text{ meV}\text{\AA}^{-1}\mu^{-1/2}$ , hence unidirectionally drives the  $Q_{LSy}$  along the  $+y$  ( $r_1$ ) direction (as indicated by the orange arrow in Figure 3a). The  $F_{anh}$  decreases the effective energy barrier along the  $r_1$  direction by 33 %, while it increases the energy barrier by 9 % along the  $r_2$  and  $r_3$  directions (according to the factor  $\cos(2\pi/3)F_{anh} = -(1/2)F_{anh}$ ). Compared to  $Q_{IRx}$ , the  $F_{anh}$  from  $Q_{IRy}$  is in the opposite direction with a slightly smaller magnitude ( $-0.87 \text{ meV}\text{\AA}^{-1}\mu^{-1/2}$ ). This explains the increase of the energy barrier along the  $r_1$  direction by 30 % and the decreases along the  $r_2$  and  $r_3$  directions by 16 %.

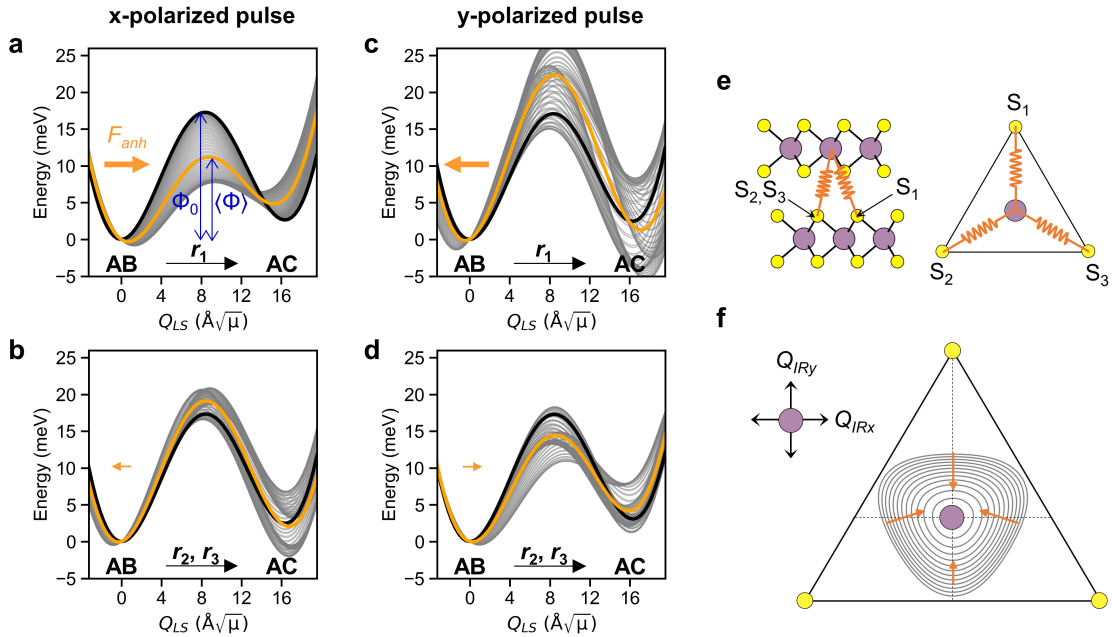


Figure 5.3 Evolution of potential energy curve on the  $Q_{LS}$  coordinate along the ferroelectric switching directions under (a, b) x-polarized and (c, d) y-polarized pulse. Rapidly oscillating  $Q_{IRx}$  under pulse modulates the potential energy curve (grey lines) with respect to the static case at  $Q_{IR} = 0 \text{ \AA}\sqrt{\mu}$  (black line). The effective potential energy experienced by the  $Q_{LS}$  is the time-average of the potential energy curves (orange line).  $\langle \Phi \rangle$  is the effective energy barrier under the pulse while  $\Phi_0$  is pristine energy barrier. Direction and relative magnitude of the effective anharmonic force  $F_{anh}$  on  $Q_{LS}$  are depicted by the orange arrow. (e) Effective interlayer interaction between the Mo and S sublattices induced by  $Q_{IR}$ . (f) Contour plot of the interaction energy indicates the direction and relative magnitude of the anharmonic force depending on the polarization direction of  $Q_{IR}$  (see main text for the details).

The polarization-dependent direction of  $F_{anh}$  has a geometrical origin related to the Mo and S sublattices, which are oppositely displaced by the  $Q_{IR}$  (Figure 5.1(c)). The motion of  $Q_{IR}$  modulates the interlayer interaction which is approximated by the springs connecting the Mo and the S atoms ( $S_1, S_2, S_3$ ) in the adjacent layers as illustrated in Figure 5.3(e). The associated interaction energy is  $k \sum_{i=1,2,3} \Delta d_i^2$ , where  $k$  is spring constant and  $\Delta d_i$  is the change in distances between the Mo and S atoms. The contour plot of the interaction energy in Figure 5.3(f) exhibits an anisotropy arising from the triangular geometry of the atomic arrangement. Notably, the gradient of contour (orange arrow) indicates the force component along the +y direction when the Mo sublattice oscillates along the x-axis with respect to the S sublattice. Meanwhile, the x-component of the force is canceled upon the rapid motion of  $Q_{IRx}$ . This simple picture explains the  $F_{anh}$  along the +y direction, and agrees with the selection rule ( $l+m = \text{even}$ ) for  $Q_{IRx}^l Q_{LSx}^m Q_{LSy}^n$  coupling. In contrast, the  $Q_{IRy}$  motion induces net forces along the -y direction due to the imbalance of the force (see the length of orange arrows).

Neither  $Q_{IRx}$  nor  $Q_{IRy}$  imparts such a unidirectional force on  $Q_{LSx}$  because the relevant coupling terms (the  $Q_{IR}^l Q_{LSy}^m$  with even  $l$ ) are absent due to the odd parity of  $Q_{LSx}$ . It prohibits the excitation of the interlayer shear along the  $r_2$  and  $r_3$  directions. Although the y-polarized light pulse lowers the energy barrier along the  $r_2$  and  $r_3$  directions, it cannot induce the ferroelectric

switching along these directions. Therefore, the most effective way to realize the ferroelectric switching is to use the x-polarized light pulse which induces both the interlayer shear motion and energy barrier lowering along the  $r_1$  direction for the ferroelectric switching to occur.

Next, we analyze the dynamics of ferroelectric switching based on the  $Q_{IRx}$ - $Q_{LSy}$  coupling under the x-polarized pulse. First, we consider the situation neglecting the damping of normal modes to show simply the essential consequences of the  $Q_{IRx}$ - $Q_{LSy}$  coupling on the dynamics of  $Q_{LSy}$  mode. Figure 5.4(a) and (b) show the motions of  $Q_{IRx}$  and  $Q_{LSy}$  modes at 0 K and 300 K, respectively, without damping under the x-polarized pulse with  $E_0 = 34$  MVcm<sup>-1</sup> and  $\sigma = 100$  fs. The initial vibration amplitudes were set as the mean-

square-displacement  $\sqrt{\langle Q_v^2 \rangle} = \sqrt{\frac{\hbar}{\Omega_v} \frac{2}{e^{(\hbar\Omega_v/k_B T)} - 1}}$  according to the Bose-

Einstein distribution at each temperature. We assumed that the initial vibration of  $Q_{LS}$  is aligned to the y-axis by setting the initial coordinate as  $Q_{LSx} = 0 \text{ \AA}\sqrt{\mu}$ . This results in the initial amplitudes of  $Q_{IRx} = 0.21 \text{ \AA}\sqrt{\mu}$  and  $Q_{LSy} = 0.91 \text{ \AA}\sqrt{\mu}$  at 0 K, while  $Q_{IRx} = 0.28 \text{ \AA}\sqrt{\mu}$  and  $Q_{LSy} = 5.70 \text{ \AA}\sqrt{\mu}$  at 300 K, respectively.

In Figure 5.4(a), the  $Q_{IRx}$  and  $Q_{LSy}$  modes oscillate with the harmonic frequency before the arrival of the pulse at 0 ps. The initial kinetic energy of  $Q_{LSy}$  mode is  $\dot{Q}_{LSy}^2 / 2 = 0.6$  meV. When the  $Q_{IRx}$  is pumped, the  $Q_{LSy}$  oscillates

with larger amplitude with respect to the shifted minimum at  $Q_{LSy} = 0.87 \text{ \AA}\sqrt{\mu}$  (in good agreement with aforementioned  $0.72 \text{ \AA}\sqrt{\mu}$  shift in the effective potential minimum). The pumping does not affect the motion of  $Q_{LSx}$  (the value remains as  $\sim 0 \text{ \AA}\sqrt{\mu}$ ), as there are no forcing terms on it. Note that the kinetic energy of  $Q_{LSy}$  mode increases to 1.6 meV by the anharmonic energy flow from the pumped  $Q_{IRx}$  mode. It is noted that the pulse and  $Q_{LSy}$  should be in-phase because the anharmonic force is unidirectional. The vibration of  $Q_{LSy}$  is restricted in a small region because the kinetic energy is still smaller than the effective barrier of  $\langle\Phi\rangle = 11.5 \text{ meV}$  under the oscillating  $Q_{IRx}$ . On the contrary, the oscillatory curve of  $Q_{LSy}$  mode at 300 K in Figure 5.4(b) shows slight modulations in shape and frequency by the onset of anharmonicity of  $Q_{LSy}$ . The kinetic energy of  $Q_{LSy}$  mode is 13.4 meV which is yet below the static energy barrier  $\Phi_0 = 17.3 \text{ meV}$ , but higher than the effective barrier  $\langle\Phi\rangle = 11.5 \text{ meV}$  under the pulse. When the  $Q_{IRx}$  mode is pumped, the  $Q_{LSy}$  mode jumps over the barrier and oscillates with colossal amplitude between  $-3.79 \text{ \AA}\sqrt{\mu}$  and  $+19.19 \text{ \AA}\sqrt{\mu}$ . The vibration corresponds to the repetitive interconversion between AB and AC stackings, due to the absence of damping.

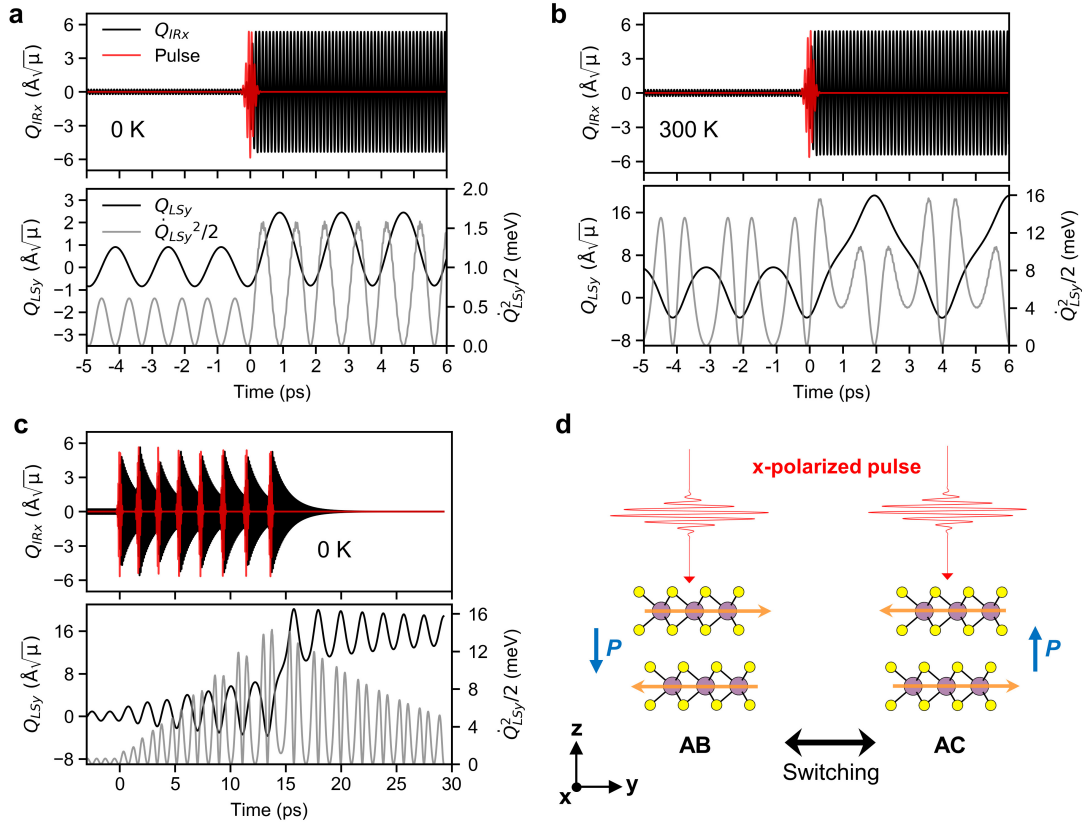


Figure 5.4 Dynamics of the normal-modes under the x-polarized pulse (a, b) without and (c) with damping. (a) Amplification of the  $Q_{LSy}$  mode through the anharmonic force by the pulse at 0 K. (b) At 300 K, the  $Q_{LSy}$  has sufficient kinetic energy to overcome the effective energy barrier ( $\langle\Phi\rangle = 11.5$  meV at  $|Q_{IRx}| = 5.35 \text{ \AA}\sqrt{\mu}$ ) after the pumping, and oscillates back and forth between the AB ( $Q_{LSy} = 0 \text{ \AA}\sqrt{\mu}$ ) and AC ( $Q_{LSy} = 16.29 \text{ \AA}\sqrt{\mu}$ ) stackings without dissipation. (c) In the presence of damping, the  $Q_{LSy}$  mode at 0 K overcomes the energy barrier after eight sequential pulses. The AB stacking changes to the AC stacking and does not return due to the dissipation of kinetic energy. (d) Schematics of ferroelectric switching through the  $Q_{IRx}$ - $Q_{LSy}$  coupling. The orange arrows indicates the directions of interlayer shear induced by the x-polarized pulse, which are opposite in the AB and AC stackings.

Second, we consider a more realistic model including the damping of the normal modes. We take the damping coefficients of  $\gamma_{IR}$  and  $\gamma_{LS}$  as 2 % of the harmonic frequencies, which are similar to the experimental values[21]. In Figure 5.4(c), the  $Q_{IRx}$  and  $Q_{IRy}$  modes initially oscillate with small amplitudes at 0 K until the arrival of the first pulse at 0 ps (damping is turned on at 0 ps). The eight pulses in the sequence are applied in order to substantially amplify the  $Q_{LSy}$  mode from the zero-point vibration at 0 K. The time interval between the subsequent pulses is gradually increased by  $\sim 4$  % from the  $1/\Omega_{LS} \sim 1.6$  ps for the phase matching between the pulse and  $Q_{LSy}$  mode, considering the increase in the period of  $Q_{LS}$  mode due to anharmonicity. Upon each cycle of pulse irradiation, the  $Q_{LSy}$  mode is coherently amplified by gaining the kinetic energy. After the eight pulses are irradiated, the  $Q_{LSy}$  mode has sufficient kinetic energy and jump over the effective barrier which is reduced by the  $Q_{IRx}$  mode. Once the initial AB stacking sequence is changed to the AC stacking, it maintains the AC stacking due to the dissipation of the kinetic energies of the vibrations. This corresponds to the AB  $\rightarrow$  AC ferroelectric switching. The opposite switching operation, AC  $\rightarrow$  AB, can be performed by the same optical input as illustrated in Figure 5.4(d). The direction of  $F_{anh}$  on  $Q_{LSy}$  mode in the AC stacking is simply reversed ( $-r_1$  direction) with respect to that ( $r_1$  direction) in the AB stacking. The optical parameters of pulses (e.g.  $E_0$  and  $\sigma$ ) used in this work might be optimized further for more efficient switching, for instance, via pulse shaping techniques[42]. Figure 5.5 shows

the result for the y-polarized pulse with a similar optical input. The anharmonic amplification occurs (Figure 5.5(a) and (b)) but the ferroelectric switching cannot be achieved due to the significantly lower energy transfer and the increase of energy barrier (Figure 5.5(c)).

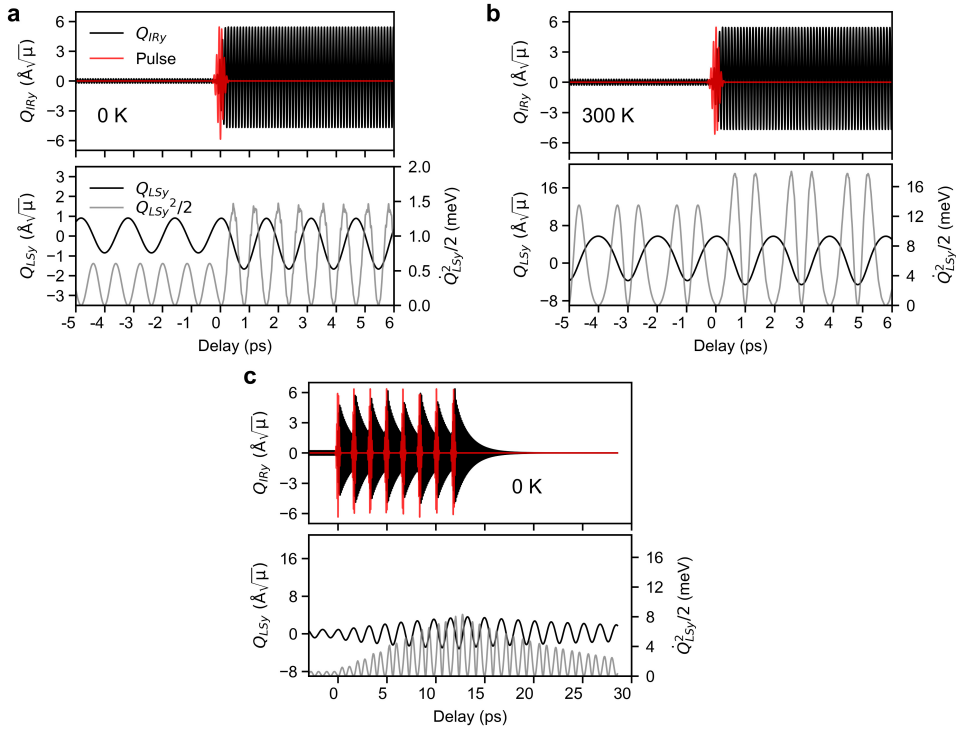


Figure 5.5 Dynamics of the normal-modes under the y-polarized pulse (a, b) without and (c) with damping. (a) Amplification of the  $Q_{LSy}$  mode through the anharmonic force by the pulse at 0 K. (b) the  $Q_{LSy}$  cannot overcome the increased effective energy barrier although its kinetic energy is increased by the pulse. (c) The gaining of kinetic energy of  $Q_{LSy}$  is smaller than x-polarized case. Even eight pulses are irradiated, switching does not take place

## 5.4 Conclusion

In summary, we investigated the polarization switching mechanism of the bilayer 3R MoS<sub>2</sub> whose direction of the polarization is reversed by the change of the stacking sequence. The ferroelectric switching is achieved by driving the interlayer shear mode through the anharmonic energy flow from the optically pumped infrared mode. Interestingly, due to the selection rule from the crystal symmetry of MoS<sub>2</sub>, the degenerate interlayer shear mode can only be driven along its armchair axis whether the infrared mode is pumped along the zigzag or armchair axis. The optical pulse, however, should be polarized along the zigzag axis for the successful switching because the direction of anharmonic force is aligned with the switching direction. The coherent light pulses can amplify the interlayer shear mode substantially and unidirectionally, displacing the stacking sequence into the opposite polarization. The scheme for optical modulation of stacking structure can be generally applied to other 2D materials exhibiting the interlayer shear mode to explore various stacking-dependent properties in a dynamical manner.

## 5.5 References

- [1] Scott J F 2007 *Science*. 315 954–9
- [2] Jeong D S, Thomas R, Katiyar R S, Scott J F, Kohlstedt H, Petraru A and

- Hwang C S 2012 *Reports Prog. Phys.* 75 076502
- [3] Wu M and Jena P 2018 *Wiley Interdiscip. Rev. Comput. Mol. Sci.* 8 e1365
- [4] Cui C, Xue F, Hu W-J and Li L-J 2018 *npj 2D Mater. Appl.* 2 18
- [5] Chang K, Liu J, Lin H, Wang N, Zhao K, Zhang A, Jin F, Zhong Y, Hu X, Duan W, Zhang Q, Fu L, Xue Q-K, Chen X and Ji S-H 2016 *Science*. 353 274–8
- [6] Cui C, Hu W-J, Yan X, Addiego C, Gao W, Wang Y, Wang Z, Li L, Cheng Y, Li P, Zhang X, Alshareef H N, Wu T, Zhu W, Pan X and Li L-J 2018 *Nano Lett.* 18 1253–8
- [7] Ding W, Zhu J, Wang Z, Gao Y, Xiao D, Gu Y, Zhang Z and Zhu W 2017 *Nat. Commun.* 8 14956
- [8] Wan W, Liu C, Xiao W and Yao Y 2017 *Appl. Phys. Lett.* 111 132904
- [9] Fei R, Kang W and Yang L 2016 *Phys. Rev. Lett.* 117 097601
- [10] Manzeli S, Ovchinnikov D, Pasquier D, Yazyev O V. and Kis A 2017 *Nat. Rev. Mater.* 2 17033
- [11] Qian X, Liu J, Fu L and Li J 2014 *Science*. 346 1344–7
- [12] Sie E J, Nyby C M, Pemmaraju C D, Park S J, Shen X, Yang J, Hoffmann M C, Ofori-Okai B K, Li R, Reid A H, Weathersby S, Mannebach E, Finney N, Rhodes D, Chenet D, Antony A, Balicas L, Hone J, Devereaux T P, Heinz T F, Wang X and Lindenberg A M 2019 *Nature* 565 61–6
- [13] Shirodkar S N and Waghmare U V. 2014 *Phys. Rev. Lett.* 112 157601
- [14] Singh A, Shirodkar S N and Waghmare U V. 2015 *2D Mater.* 2 035013
- [15] Park J, Yeu I W, Han G, Jang C, Kwak J Y, Hwang C S and Choi J-H

- 2019 *J. Phys. Condens. Matter* 31 315502
- [16] Li L and Wu M 2017 *ACS Nano* 11 6382–8
- [17] Fei Z, Zhao W, Palomaki T A, Sun B, Miller M K, Zhao Z, Yan J, Xu X and Cobden D H 2018 *Nature* 560 336–9
- [18] Yang Q, Wu M and Li J 2018 *J. Phys. Chem. Lett.* 9 7160–4
- [19] Suzuki R, Sakano M, Zhang Y J, Akashi R, Morikawa D, Harasawa A, Yaji K, Kuroda K, Miyamoto K, Okuda T, Ishizaka K, Arita R and Iwasa Y 2014 *Nat. Nanotechnol.* 9 611–7
- [20] Tan P H, Han W P, Zhao W J, Wu Z H, Chang K, Wang H, Wang Y F, Bonini N, Marzari N, Pugno N, Savini G, Lombardo A and Ferrari A C 2012 *Nat. Mater.* 11 294–300
- [21] Zhang X, Han W P, Wu J B, Milana S, Lu Y, Li Q Q, Ferrari A C and Tan P H 2013 *Phys. Rev. B* 87 115413
- [22] Zhang X, Qiao X-F, Shi W, Wu J-B, Jiang D-S and Tan P-H 2015 *Chem. Soc. Rev.* 44 2757–85
- [23] Först M, Manzoni C, Kaiser S, Tomioka Y, Tokura Y, Merlin R and Cavalleri A 2011 *Nat. Phys.* 7 854–6
- [24] Subedi A, Cavalleri A and Georges A 2014 *Phys. Rev. B* 89 220301
- [25] Juraschek D M and Maehrlein S F 2018 *Phys. Rev. B* 97 174302
- [26] Subedi A 2015 *Phys. Rev. B* 92 214303
- [27] Mankowsky R, von Hoegen A, Först M and Cavalleri A 2017 *Phys. Rev. Lett.* 118 197601
- [28] Ghimire S, DiChiara A D, Sistrunk E, Agostini P, DiMauro L F and Reis

- D A 2011 *Nat. Phys.* 7 138–41
- [29] You Y S, Yin Y, Wu Y, Chew A, Ren X, Zhuang F, Gholam-Mirzaei S, Chini M, Chang Z and Ghimire S 2017 *Nat. Commun.* 8 724
- [30] Liu H, Li Y, You Y S, Ghimire S, Heinz T F and Reis D A 2017 *Nat. Phys.* 13 262–5
- [31] Qi T, Shin Y-H, Yeh K-L, Nelson K A and Rappe A M 2009 *Phys. Rev. Lett.* 102 247603
- [32] Chen F, Zhu Y, Liu S, Qi Y, Hwang H Y, Brandt N C, Lu J, Quirin F, Enquist H, Zalden P, Hu T, Goodfellow J, Sher M-J, Hoffmann M C, Zhu D, Lemke H, Glowina J, Chollet M, Damodaran A R, Park J, Cai Z, Jung I W, Highland M J, Walko D A, Freeland J W, Evans P G, Vailionis A, Larsson J, Nelson K A, Rappe A M, Sokolowski-Tinten K, Martin L W, Wen H and Lindenberg A M 2016 *Phys. Rev. B* 94 180104
- [33] Juraschek D M, Fechner M and Spaldin N A 2017 *Phys. Rev. Lett.* 118 054101
- [34] Kresse G and Furthmüller J 1996 *Comput. Mater. Sci.* 6 15–50
- [35] Kresse G and Furthmüller J 1996 *Phys. Rev. B* 54 11169–86
- [36] Blöchl P E 1994 *Phys. Rev. B* 50 17953–79
- [37] Perdew J P, Burke K and Ernzerhof M 1996 *Phys. Rev. Lett.* 77 3865–8
- [38] Grimme S, Antony J, Ehrlich S and Krieg H 2010 *J. Chem. Phys.* 132 154104
- [39] King-Smith R D and Vanderbilt D 1993 *Phys. Rev. B* 47 1651–4
- [40] Togo A and Tanaka I 2015 *Scr. Mater.* 108 1–5

[41] Gonze X and Lee C 1997 *Phys. Rev. B* 55 10355–68

[42] Itin A P and Katsnelson M I 2018 *Phys. Rev. B* 97 184304

# CHAPTER 6

## CONCLUSION

---

In this dissertation, a range of electronic properties – electron transport, interlayer dynamics, and ferroelectricity – of MoS<sub>2</sub> are investigated with the particular focus on the roles of the interface and crystalline symmetry of the 2D materials systems for the device applications.

The single layer MoS<sub>2</sub> realizes the extremely thin semiconducting channel with enhanced electrostatic control for the switching devices. In this thesis, we studied the effect of the extrinsic interface formed with the gate oxides on the electron transport. We investigated the high-*k* HfO<sub>2</sub> and the low-*k* SiO<sub>2</sub> oxides in order to explore the atomistic origin of the superior electron transport in the high-*k* gate oxides compared to the low-*k* ones. Using the *ab initio* simulations, we revealed that the interface structures between the SiO<sub>2</sub> and MoS<sub>2</sub> showed the interface chemical bonds and dangling bonds while those between the HfO<sub>2</sub> and MoS<sub>2</sub> hardly showed such interfacial defects. The differences in the interface atomic structures directly reflected in the

degree of perturbation of the electronic band structures of MoS<sub>2</sub>. The electron effective mass of MoS<sub>2</sub> in contact with the HfO<sub>2</sub> is intact like the suspended form while that increases substantially at the interface with the SiO<sub>2</sub>. The characteristic interface chemistry between the inert surface of MoS<sub>2</sub> and the surface of amorphous oxides with the broken bonds was explained in terms of the distinct short-range order of the oxides. The results provide alternative interpretation on the role of high-*k* oxides in mobility boosting of 2D materials based MOSFET and emphasize the importance of careful treatment of the surface of gate oxide to form high-quality interface.

Multilayer structure enriches the functionalities of 2D materials from newly emerging properties. Basic design rule is set by the crystalline symmetry for the target function. In this thesis, we studied how the crystalline symmetry of multilayer MoS<sub>2</sub> affects the protocol to harness the layer degree of freedom of electrons newly as an information carrier in the valleytronic devices. Following the complementary study based on density functional theory and double group theory, we demonstrated that valley electrons in the polar 3R structure are confined exclusively within each layer with definite spin under the built-in electric field. The one-to-one correspondence between the layer degree of freedom and potential energy evoked an analogy with the valley degree of freedom coupled with the crystal angular momentum in the non-centrosymmetric system. We further showed that the binary operation on the layer degree of freedom, upward and downward interlayer motions, hence can

be performed based on the energy conservation by selectively irradiating the visible and infrared lights.

Finally, we explored the possibility of the ferroelectricity of MoS<sub>2</sub> based on the bilayer 3R structure. The ferroelectricity of the 3R structure requires the dynamic control of the stacking sequence through the interlayer shear for the polarization reversal. To this end, we investigated the optical route to substantially drive the interlayer shear vibrations which is Raman active into the switching directions based on the nonlinear phononics scheme. From the calculations of the potential energy surfaces, we showed that the interlayer shear mode can be coherently driven upon the intense terahertz laser pulse irradiation through the nonlinear coupling of the infrared active mode and the interlayer shear mode. The effect depends on the polarization angle of incident pulse and the switching can be successfully performed for the zigzag axis of MoS<sub>2</sub>. This scheme addresses the generic problem on the possibility of structure control in layered 2D materials and hence can be applied to the other systems on demands.

In conclusion, using first principles, we elucidated the fundamental consequences of atomistic structure on the electronic properties of MoS<sub>2</sub> in various aspects and the ways to realize the functions in the devices. Still, many tasks are remained to realize the working device aided by 2D materials for the industry and to provide a blueprint for the 2D-specific nanodevice. We believe that the constructed structure-property correlations in this study shall

provide some insights into the low-dimensional materials and devices.

## LIST OF PUBLICATIONS

---

### Journals (SCI)

[10] Min Hyuk Park, Han Joon Kim, Gwang Yeop Lee, Jaehong Park, Young Hwan Lee, Yu Jin Kim, Taehwan Moon, Keum Do Kim, Seung Dam Hyun, Hyun Woo Park, Hye Jung Chang, Jung-Hae Choi, Cheol Seong Hwang, “Ferroelectricity in polycrystalline nanolaminates and superlattices based on fluorite oxides”, (submitted)

[9] Jaehong Park, In Won Yeu, Gyuseung Han, Cheol Seong Hwang, and Jung-Hae Choi, “Ferroelectric switching in bilayer 3R MoS<sub>2</sub> via interlayer shear mode driven by nonlinear phononics“, (to be submitted)

[8] Jaehong Park, In Won Yeu, Gyuseung Han, Chaun Jang, Joon Young Kwak, Cheol Seong Hwang, and Jung-Hae Choi “Optical Control of the Layer Degree of Freedom through Wannier-Stark States in Polar 3R MoS<sub>2</sub>“, *J. Phys.: Condens. Matter* 31, 315502 (2019)

[7] Jaehong Park, In Won Yeu, Gyuseung Han, Cheol Seong Hwang, and Jung-Hae Choi, “Role of the Short-Range Order in Amorphous Oxide on MoS<sub>2</sub>/a-SiO<sub>2</sub> and MoS<sub>2</sub>/a-HfO<sub>2</sub> Interfaces“, *Phys. Status Solidi B* (2019) (in press)

- [6] Kai Liu, Eunjung Ko, Sangtae Kim, Jaehong Park, Cheol Seong Hwang and Jung-Hae Choi, "Orientation-dependent structural and electronic properties of Ge/a-GeO<sub>2</sub> interfaces: first-principles study", *J. Phys. D: Appl. Phys.* 52, 155101 (2019)
- [5] In Won Yeu, Gyuseung Han, Jaehong park, Ceol Seong Hwang & Jung-Hae Choi, "Equilibrium crystal shape of GaAs and InAs considering surface vibration and new (111) B reconstruction: ab-initio thermodynamics", *Sci. Rep.* 9, 1127 (2019)
- [4] In Won Yeu, Jaehong Park, Gyuseung Han, Cheol Seong Hwang & Jung-Hae Choi, "Surface reconstruction of InAs (001) depending on the pressure and temperature examined by density functional thermodynamics", *Sci. Rep.* 7, 10691 (2017)
- [3] Swastika Banerjee, Jaehong Park, Cheol Seong Hwang, Seung-Cheol Lee, Jung-Hae Choi and Swapan K. Pati, "Regulation of transport properties by polytypism: a computational study on bilayer MoS<sub>2</sub>", *Phys. Chem. Chem. Phys.*, 19, 21282 (2017)
- [2] Jaehong Park, Joohwi Lee, Cheol Seong Hwang, and Jung-Hae Choi, "Atomic and electronic structures of a-ZnSnO<sub>3</sub>/a-SiO<sub>2</sub> interface by ab initio molecular dynamics simulations", *Phys. Status Solidi B* 253, 1765 (2016)
- [1] Joohwi Lee, Jong Kwon Choi, Seon Young Moon, Jaehong Park, Jin-Sang

Kim, Cheol Seong Hwang, Seung-Hyub Baek, Jung-Hae Choi, and Hye Jung Chang, “Symmetry-dependent interfacial reconstruction to compensate polar discontinuity at perovskite oxide interfaces ( $\text{LaAlO}_3/\text{SrTiO}_3$  and  $\text{LaAlO}_3/\text{CaTiO}_3$ )“, *Appl. Phys. Lett.* 106, 071601 (2015)

## Conferences

[10] Jaehong Park, Cheol Seong Hwang, and Jung-Hae Choi, “Intrinsic electric polarization and its switching mechanism in 2D transition metal dichalcogenides having polar symmetry“, 제14회 고등과학원 전자구조계산학회 (poster), 21-22 Jun. 2018

[9] Jaehong Park, Cheol Seong Hwang, and Jung-Hae Choi, “Layer-index and valley-index of electrons in 2D transition metal dichalcogenides for optoelectronic applications:  $3\text{R MoS}_2$ “, The 25th Korean Conference on Semiconductors (oral), 5~7 Feb. 2017, Kangwon-do, Korea

[8] Jaehong Park, Cheol Seong Hwang, and Jung-Hae Choi, “Stacking-dependent electric polarization and optical transitions of K valley states in  $\text{MoS}_2$ “, 제13회 고등과학원 전자구조계산학회 (poster), 15-16 Jun. 2017

[7] Jaehong Park, Cheol Seong Hwang, and Jung-Hae Choi, “Ab initio study on the atomic and electronic structures of  $\text{MoS}_2$ /oxide interface“, The 24th

Korean Conference on Semiconductors (oral), 13~15 Feb. 2017, Kangwon-do, Korea

[6] Jaehong Park, Cheol Seong Hwang, and Jung-Hae Choi, “Optical Control of the Layer index of Electrons in Polar stacked MoS<sub>2</sub>”, 2016 Fall Meeting of the Korean Ceramic Society (oral), 23-25 Nov. 2016, Seoul, Korea

[5] Jaehong Park, Cheol Seong Hwang, and Jung-Hae Choi, “Ab-initio study on the effects of doping in mono and bilayer MoS<sub>2</sub>“, The 23rd Korean Conference on Semiconductors (oral), 22~24 Feb. 2016, Kangwon-do, Korea

[4] Jaehong Park, Cheol Seong Hwang, and Jung-Hae Choi, “Effects of the layer stacking on the electronic, phononic band structures and electron-phonon interactions in MoS<sub>2</sub>“, Psi-K Conference 2015 (poster), 6-10 Sept. 2015, Donostia/San Sebastian, Spain

[3] Jaehong Park, Cheol Seong Hwang, and Jung-Hae Choi, “Effects of the Polytypism on the Electronic, Phononic Band Structures of Ultrathin MoS<sub>2</sub>“, 제11회 고등과학원 전자구조계산학회 (poster), 18-19 Jun. 2015

[2] Jaehong Park, Cheol Seong Hwang, and Jung-Hae Choi, “Effect of Stacking Sequence on the Electronic Properties of Layered MoS<sub>2</sub>: Polytypism and Heterostructure“, The 22nd Korean Conference on Semiconductors (poster), 10~12 Feb. 2015, Incheon, Korea

[1] Jaehong Park, Joohwi Lee, Cheol Seong Hwang, and Jung-Hae Choi, “Ab-initio Study on the Interface Structure of a-ZnSnO<sub>3</sub>/a-SiO<sub>2</sub>“, 17th Asian Workshop on First-principles Electronic Structure Calculations (poster), 2~5 Nov. 2014, Seoul, Korea

### **Patents**

[1] 최정혜, 김성근, 박재홍, “발광 진동수 제어가 가능한 2차원 pn 접합구조를 갖는 발광소자 및 그 제조방법“, 10-1907549

## 국 문 초 록

---

이황화몰리브덴( $\text{MoS}_2$ )은 원자 세 개에 해당하는 두께를 가지는 결정질 시트가 반 데르 발스 힘에 의해 적층된 형태의 2차원 물질이다. 이 재료의 핵심 특징인 2차원 기하구조로부터 나타나는 물성은 소자 스케일링에 대한 획기적인 대안 내지는 완전히 새로운 유형의 소자에 대한 청사진을 제시하였기 때문에 학계와 산업계를 매료시켰다. 그러나 동시에 2차원 구조는 실제 소자에 도입하고자 할 때에 큰 어려움을 가져온다. 중요한 문제 중 하나는 소자 구성 시 필연적으로 나타나는 계면구조에 의해 전기적 물성이 크게 변화한다는 것이다. 전계효과 트랜지스터 구조에서 나타나는 게이트 산화물간의 extrinsic 계면이나 적층구조에서 발생하는 인접 층간의 intrinsic 계면이 그 예이다. 또 다른 문제는 적층구조의 결정학적 대칭성이 적층방식에 따라 변화한다는 것이다. 이러한 대칭성은 위상학적 전류 및 강유전성과 같은 다양한 특성을 결정하는데 매우 중요한 역할을 한다.

본 논문에서는  $\text{MoS}_2$ 의 전기적 물성에 대한 계면 및 대칭성의 역할을 밀도범함수이론에 기반한 제일원리계산을

이용하여 연구하였다. 이를 통해  $\text{MoS}_2$ 의 구조-물성 상관관계에 대하여 이론적으로 고찰하고, 나아가 2차원 재료 기반 논리소자의 가능성을 향상시키거나 새로운 가능성을 부여하기 위한 방법론을 제시한다.

먼저 단일 층  $\text{MoS}_2$ 로 만들어진 전계효과 트랜지스터에서 나타나는 게이트 산화물간의 계면원자구조에 대하여 연구하였다. 이 연구에서는 제일원리 분자동역학법을 이용하여  $\text{MoS}_2$ 와 산화물의 계면에서 나타나는 화학반응을 모사하였고, 계면에서의 화학적 상호작용에 따라  $\text{MoS}_2$ 의 전자 밴드구조가 크게 변화될 수 있음을 보여주었다. 이 결과는 그 동안 논쟁이 있었던 산화물 종류에 따른 전자수송 특성의 열화 현상에 대하여 원자수준의 메커니즘을 제안한다. 또한  $\text{MoS}_2$  기반 트랜지스터의 성능을 향상시키기 위해 신중한 계면처리의 중요성을 시사한다.

다음으로 특정 대칭성을 가지는 적층구조  $\text{MoS}_2$  에서 발견되는 새로운 전기적 물성을 연구하였다. 최근의 이론 및 실험 연구들은 multi-valley 밴드구조를 가지는 반도체에서 전자의 valley 자유도(valley degree of freedom)를 정보로 활용하는 valleytronics 기술의 기반을 확립하였다. 한편, 적층구조에 존재하는 전자는 층간 위치에 해당하는 layer 자유도(layer degree of freedom)를

자연적으로 갖게 되며 이는 기존 valleytronics 개념에 추가적인 정보 매개체로서 통합될 수 있다. 그러나 layer 자유도를 제어하여 정보로 이용하고자 하는 연구는 valley 자유도에 대한 연구에 비해 매우 제한적 이었다. 본 연구에서는 밀도범함수이론과 군론에 기반하여 적층구조의 대칭성이 layer 자유도의 특성에 미치는 영향을 심도 있게 연구하였다. 이를 통해 극성 대칭(polar symmetry)을 가지는 3R 구조에서 나타나는 전자의 layer 자유도 특성이 효율적인 제어에 적합하다는 것을 보여주었다. 이 결과는 layer 자유도의 제어방식과 반전 비대칭(inversion asymmetric) 구조에서 나타나는 valley 자유도의 제어방식 사이에 유사점(analogy)이 있음을 보여준다.

마지막으로 3R 구조 MoS<sub>2</sub>에서의 강유전성에 대하여 연구하였다. 지금까지 MoS<sub>2</sub>의 강유전성은 단일 층 구조에 존재하는 거울 대칭으로 인하여 간과되어왔다. 하지만 3R 구조는 층간 상호작용으로 인해 자발적 전기분극(spontaneous polarization)이 존재한다. 따라서 층간 밀립에 대한 제어를 통해 강유전 스위칭을 일으킬 수 있다. 본 연구에서는 적외선 활성 포논(infrared active phonon)과 층간 전단 포논 (interlayer shear phonon)간의 nonlinear phononics에 기반한 강유전 스위칭 메커니즘을 연구하였다. 이 결과는 강한 적외선 영역의 레이저 펄스를 이용하여 매우 빠른

속도로 강유전 스위칭을 일으킬 수 있다는 가능성을 보여준다.

이 논문은 계면과 대칭성이  $\text{MoS}_2$ 의 전기적 물성에 미치는 매우 중요한 역할을 다양한 소자 응용 관점에서 보여준다. 또한 구조-물성 상관관계 및 이에 따라 새롭게 발현되는 물성을 활용하는 전략을 제시하고 있다. 이 연구 결과는 저차원 재료 및 소자 실현에 대한 연구에 중요한 밑거름이 될 것이다.